Age-dependent meningeal macrophages protect against viral neuroinfection

Julie Rebejac, Elisa Eme-Scolan, Matei Teleman, Lionel Spinelli, Emeline Gallo, Annie Roussel-Queval, Ana Zarubica, Bernard Malissen, Marie-Cécile Michallet, Toby Lawrence, et al.

Age-dependent meningeal macrophages protect against viral neuroinfection

Julie Rebejac(1), Elisa Eme-Scolan(1), Matei Teleman(1), Lionel Spinelli(1), Emeline Gallo(1), Annie Roussel-Queval(1), Ana Zarubica(2,3), Bernard Malissen(1,2,3), Marie-Cécile Michallet(4), Toby Lawrence(1,5), Monica Manglani(6), Dorian B. McGavern(6) & Rejane Rua(1)

Affiliations:

(1) Aix Marseille University, Inserm, CNRS, Immunology Center of Marseille-Luminy, Marseille, France;

(2) Immunophenomique Center, Aix Marseille University, Inserm, CNRS UMR, Marseille, France;

(3) Laboratory of Immunophenomics, School of Laboratory Medicine, Xinxiang Medical University, Xinxiang, China;

(4) Centre de recherche en cancérologie de Lyon, Centre Léon Bérard, Université de Lyon, Inserm, CNRS, Lyon, France.

(5) Centre for Inflammation Biology and Cancer Immunology, Cancer Research UK King's Health Partners Centre, School of Immunology and Microbial Sciences, King's College London, London SE1 1UL, UK.

(6) Viral Immunology and Intravital Imaging Section, National Institute of Neurological Disorders and Stroke, National Institutes of Health, Bethesda, MD 20892, USA;

Corresponding author

Rejane RUA, PhD

Centre d'Immunologie de Marseille Luminy

Parc Scientifique et technologique de Luminy

163 Avenue de Luminy

Case 906- 13288 Marseille cedex 9- FRANCE

CNRS UMR7280, INSERM U1104, AMU UM2

Phone: +33 (0)4 91 26 94 35

Email: rua@ciml.univ-mrs.fr

Abstract

Due to the vital importance of the Central Nervous System (CNS), its potential infection and inflammation have to be tightly controlled. The surface of the CNS is connected to the periphery by a rich and complex tissue, the meninges. They contain a vast network of macrophages subdivided in at least two subpopulations endowed with elusive functions: a neonatal, MHC-II negative macrophage population, and an age-dependent population expressing MHC-II. Using *in situ*-histocytometry, flow cytometry, and single-cell RNA sequencing approaches, we showed that those populations have opposite dynamic behaviors in response to *in vivo* peripheral challenges such as LPS, SARS-CoV2 and lymphocytic choriomeningitis virus (LCMV), with an apparent contraction of the MHC-II+ population. Focusing on LCMV infection in experimental mouse models and using innovative pharmacological and genetic depletion strategies, we show that meningeal macrophages (MM) represent an early line of protection against this neuroinvasive pathogen. In their absence, specific areas in the meninges became highly infected, leading to fatal brain disease. While their intrinsic sensing of viral replication through the Mitochondrial antiviral-signaling protein (MAVS) was dispensable, sensing of IFNs through the STAT1 pathway played an important role in controlling viral spread. Unexpectedly, the age-dependent MHC-II+ macrophage population had an important role in controlling neuroinfection, by shutting down biosynthesis pathways and efficiently blocking viral replication. This work helps understanding the spatial organization of the brain defense system and the cellular and molecular mechanisms involved in CNS protection.

Introduction

The Central Nervous System (CNS) is protected from the periphery by different anatomical barriers which ensure its structural integrity. While several studies have focused on the neuroprotective role of the blood-brain barrier (in the parenchyma) and the choroid plexus (within the brain ventricles), much less is known about the barrier localized at the surface of the CNS [1, 2].The outer surface of the CNS (brain and spinal cord) is connected to the periphery by highly vascularized membranes devoid of a blood-brain barrier, the meninges [2]. The outer layer is called the dura matter, and will be referred to as 'meninges' thereafter. Meninges were thought to represent an inert connective tissue. However, similar to other barrier tissues in the skin, lung, intestine and liver, the meninges are populated by a myriad of resident immune sentinels [3]. Recent data indicate that those immune sentinels at the brain surface are far more diverse than in the parenchyma, and include dendritic cells, lymphocytes, mast cells and also macrophages, the most abundant population [2, 4, 5, 6, 7, 8, 9, 10]. Due to their strategic location at the interface between the periphery and the brain, immune cells in the meninges can communicate with both compartments. At homeostasis, the meninges protect and nurture the CNS vascular and neural structures during development, and meningeal immune cells are already known to contribute to social and cognitive behavior at steady state in particular through the release of IL4, IL17 and IFNγ [11, 12, 13]. The meningeal immune system is also involved in inflammatory and neurodegenerative diseases [14, 15, 16, 17, 18]. We and others have shown that meninges can readily get inflamed and propagate damage to the underneath parenchyma in cases of autoimmune diseases [2].

Are meningeal immune sentinels beneficial or detrimental in case of other challenges, such as CNS infections? The surface of the CNS is seeded by 2 populations of MM (MM), MHC-II+ and MHC-II-, of elusive functions [4, 5, 19, 20]. Whether MM populations control viral neuroinvasion or promote inflammation, and by which mechanisms, is unclear.

Most studies on CNS viral infection in mouse models use an intracranial route of injection which bypasses potential antiviral mechanisms located at the CNS borders [21]. Using a more natural route of infection (hematogenous instead of intracranial), we analyzed for the first time the initial events occurring at the CNS borders, using the acute lymphocytic choriomeningitis model (LCMV Armstrong neurotropic strain 53b, noted LCMV thereafter) and uncovered an age-dependent population of macrophage able to control viral spread.

Meningeal macrophage populations coexist and differentially uptake peripheral compounds

We first analyzed the macrophage populations present at steady state in primate meninges and mouse meninges and confirmed the presence of a vast network of MM that can be identified using Ionized calcium binding adaptor molecule 1 (IBA1) (Figure 1A, primate

meninges, up) or the mannose receptor CD206 (Figure 1 A, mouse meninges, down) [20]. This macrophage network covered the spinal (Supplementary Figure 1A) and cranial meninges (Supplementary Figure 1B, C), with a higher density of MM in the brain meninges (Supplementary Figure 1D). MM density did not significantly vary over time (Supplementary Figure 1E) and looked similar across mammals (Supplementary Figure 1F). MM could be subdivided into MHC-II+ and MHC-II- populations, and the proportion of MHC-II+ cells was high in aged primates (Figure 1B). We developed a panel of antibodies allowing flow cytometric analysis of immune cells in mouse meninges (Supplementary Figure 2A) and kinetics experiments indicated an increase of the proportion of MHC-II+ MM in mouse meninges over time (Figure 1C, left panel). This was accompanied by the up-regulation of the inflammatory marker MHC-I (Figure 1C, right panel) over time. To understand whether MHC-II+ MM were coming from the neonatal pool of MM, or from blood-derived monocytes, we performed lineage-tracing experiments. In adult animals, infiltrating monocytes preferentially contributed to the MHC-II+ macrophage pool, leading to the accumulation of MHC-II+ cells over time (Supplementary Figure 2B, C). We then compared macrophage populations' ability to detect compounds injected peripherally. Because meningeal vessels do not have tight junctions, they are permeable to small molecular-weight dextran (10kDa) [2]. MM could readily pick up dextran injected in the vasculature (Figure 1D), with more uptake by MHC-II+ MM (Figure 1E). Meninges contain 2 main structures: the sinuses (superior sagittal and transverse venous sinuses), and the lobes. Using *in situ* histocytometry, a technique allowing visualization, gating and quantification of the fluorescence intensity of cell subsets, we found that the dextran was uptaken by most MHC-II+ MM in the sutures (Figure 1F). Taken together, these results indicate that MM are organized in an evolutionary conserved network allowing efficient detection of peripheral compounds at the brain surface, and that the age-dependent MHC-II+ MM are particularly efficient in this matter.

Meningeal macrophage populations differentially respond to a peripheral microbial product

To have a more integrated view of meningeal response to peripheral challenge, we performed single-cell RNA sequencing on total nucleated meningeal cells 24 hours after PBS or LPS injection (Figure 2A). Eight immune and seven non-immune populations could be detected, including MM (cluster 4). The shift of their UMAP positioning was consistent with a complete change in their transcriptional program after PBS injection (Figure 2A). When subdivided into 2 clusters, we could detect a MHC-II^{high} population and a MHC-II^{low} population, upon both PBS or LPS treatments (Figure 2B). Both MHC-II+ and MHC-II- MM populations responded to LPS, but more than two third of their transcriptomic changes was specific of each population (Figure 2C). In addition, a higher response (number of differentially expressed genes) was detected

in MHC-II- population (Figures 2C-F). We first analyzed the changes in the overall macrophage population. Gene ontology analysis revealed that the pathways differentially regulated upon macrophage activation were mainly linked with antigen processing and metabolic processes (Figure 2G). Interestingly, when focusing on each macrophage population, we uncovered that the main response of MHC-II+ MM consisted in suppressing several pathways linked with translation and antigen-presentation. The few upregulated pathways were linked with chemotaxis, IL1 response (Figure 2H) and cell death (necrosis and apoptosis) (Supplementary Figure 3). In contrast, MHC-II- MM upregulated metabolic processes linked with translation (ribosomes) and respiration (mitochondria), indicating an activation of biosynthetic processes (Figure 2I). Of note, most of the transcriptomic pathways linked with tissue development and growth were down-regulated in the MHC-II- population (Supplementary Figure 4). This suggested that the homeostatic function of MHC-II- MM (tissue nurturing) was compromised upon challenge. To check the reliability of our results based on this clustering method (Supplementary Figure 5A), we performed an additional set of analyses without pre-clustering each macrophage population. Cells expressing CD206 gene were selected and assigned to each group (MHC-II+ and MHC-II- MM) based on their MHC-II score (score threshold set to 0, for details see Material and Methods) (Supplementary Figure 5B). We found a similar trend regarding the differentially expressed genes (DEG) in each macrophage population (Supplementary Figure 1C) (Supplementary Figure 5C, D). The top 10 pathways (Supplementary Figure 5E) and the top 100 pathways (Supplementary Figure 6 and 7) showed overlapping pathways compared to the previous analysis (underlined in green in Supplementary Figure 5E). In particular, MHC-II+ macrophage down-regulated MHC-II pathway, transcription, translation, autophagy, and global response to stimulus, while upregulating chemotaxis and response to IL1 (Supplementary Figure 5E). In addition, MHC-II- MM showed upregulation of biosynthesis and oxidative phosphorylation, while down-regulating production of grown and developmental factors (Bmp, Igf) (Supplementarty Figure 5E).

Consistent with MHC-II+ macrophage transcriptome (down-regulation of MHC-II and upregulation of death-related pathways and chemotaxis), the proportion of MHC-II+ MM was decreased upon activation (from 65.3% to 46.8%) (Figure 2J). This decrease of MHC-II+ MM was also confirmed in meningeal samples of mice injected with LPS (as above, Figure 2K), LCMV (Figure 2L), and SARS-CoV2 (Figure 2M, N). These data indicate that macrophage populations had opposite behaviors in response to peripheral insult: MHC-II+ MM blocked metabolic processes which could shunt viral replication, while MHC-II- MM increased biosynthetic pathways, which could make them ideal viral factories.

Peripherally injected LCMV reaches the meninges leading to immune cells activation

Meningitis is usually triggered by intracranial injection of LCMV [20]. Peripheral injection of LCMV is more physiological but has never been used so far as a model of meningitis as it is asymptomatic. We thus tested whether the absence of pathology was in fact due to an active control of the virus at the CNS borders. We first evaluated whether LCMV could reach the CNS after a peripheral injection. We injected mice intravenously with LCMV and quantified in the meninges and brain the LCMV mRNA at 1, 6 or 30 days after infection. Real Time quantitative PCR (RT-qPCR) showed that meninges and brain were infected at 1 day and 6 days post-injection (Figure 3A,B). Only a small proportion of MM were infected (Figure 3C). Analysis of immune cells in meninges 6 days after infection showed a significant increase in the number of monocytes and CD8+ T cells (Figure 3D). Moreover, MM were activated, as shown by MHC-I upregulation (Figure 3E). Immunohistochemistry on whole-mount meninges 6 days after intravenous injection of LCMV showed clusters of MHC-II, CD11b and LCMV-specific P14 OFP+ cells (P14 mice are transgenic for a TCR that recognizes LCMV gp33/Db) in the interparietal, parietal and frontal lobes (Figure 3 F, G). This indicates that LCMV could transiently infect the CNS compartment even after a peripheral injection, where it triggered an efficient immune response.

Pharmacological depletion of MM results in fatal meningitis

Because there was no efficient tool to properly deplete MM without also depleting microglia, or without triggering massive inflammation, we developed an innovative transcranial delivery approach to deliver CSF1R antagonist (PLX3397) in the meninges, as CNS macrophages depend on CSF1R signaling for their survival [4]. Titration of the drug allowed depletion of MM with limited off-target effects (mainly affecting dendritic cells, even though not significant), as assessed by flow cytometry (Figure 4A). *In situ* histocytometry confirmed an efficient depletion of MM populations, both in the lobes and the sutures (Figure 4B,C). Although flow cytometric analysis showed that parenchymal non-microglial macrophages, that comprise barrier-associated macrophages (BAM) (pial and choroid plexus macrophages) as well as perivascular macrophages were not affected (Figure 4D), a more detailed analysis of the brain surface by pial whole mount immunohistochemistry revealed a decrease of pial macrophage density (Figure 4E). Importantly, both flow cytometric and immunohistochemistry analysis revealed that microglia number was not significantly affected by the treatment (Figure 1F, G) although a trend was detectable. Blood and spleen myeloid cells were not affected by the treatment either (Figure 4G,H). This is likely due to the higher concentration of the drug reaching the dural meninges compared to the vasculature and the parenchyma. Strikingly, in the absence of MM, LCMV viral load was specifically increased in the brain, but not the spleen, of infected mice (Figure 4J) which led to fatal meningitis (Figure 4K). Symptoms at the time of death typical of meningitis included seizure and weakness. Some areas of the meninges

became massively infected following intravenous LCMV injection after PLX treatment (Figure 4L). This pharmacological depletion of MM shed light on the new role of those cells in preventing fatal meningitis.

Genetic depletion of MM results in fatal meningitis

To further elucidate the role of MM, we used Cd163-Cre mice [22]. We first evaluated the recombination efficiency using a YFP-reporter mouse. A majority of MM were YFP+ (>50% of Macs 206+ MHC-II+ and >60% of Macs CD206+ MHC-II-, Figure 5A), while the other cell types were less affected by the recombination. Importantly, in the brain, microglia was not targeted, while a majority of parenchymal barrier-associated macrophages were YFP+ (>50% of Macs 206+ MHC-II+ and >60% of Macs CD206+ MHC-II-, Figure 5B). To efficiently deplete MM, we then used Cd163-Cre : Csfr1-LSL-DTR mice. After two consecutive days of DT injection, MM were efficiently depleted (Figure 5C), while microglia was not significantly affected (Figure 5D). Of note, this depletion strategy did not trigger an inflammatory reaction in the meninges (although a trend towards more inflammatory cells was detected) and in the brain (Figure 5C, D). Following macrophage depletion, LCMV was injected in the vasculature and mice were analyzed 6 days later. MM remained depleted (Figure 5E), while the viral load in the brain was significantly increased (Figure 5F), leading to fatal meningitis (Figure 5G). Of note, the viral loads in the spleen were also higher in Cd163-Cre : Csfr1-LSL-DTR mice (Supplementary Figure 8). Further analysis of the meninges of MM-depleted mice revealed clusters of infected cells in the lobes and the suture, around blood vessels, at day 3 post-infection. Three days later, the virus had also spread to the sutures (Figure 5H). Overall, this genetic depletion of MM confirms the role of MM in preventing fatal meningitis.

Cytokine sensing by MM, but not intrinsic viral detection, is required for LCMV control

Previous studies have shown that peripheral infection with LCMV in mice deficient for Signal transducer and activator of transcription 1 (STAT1) [23] or for Mitochondrial antiviral-signaling protein (MAVS) [24] results in higher viral loads compared to controls. Thus, both IFN-response through STAT1 and intrinsic sensing through MAVS could be involved in LCMV control by MM. We first used the LysM-Cre: $Stat1^{fl/fl}$ mice, keeping in mind that LysM-Cre targets not only macrophages but also monocytes, neutrophils and microglia. Deletion of Stat1 in LysM-derived cells resulted in increased recruitment of CD8+ T cells at day 6 post-infection (Figure 6A), which was associated with an increased viral load (Figure 6B). Mice did not succumb to the infection (Supplementary Figure 9A) although weight loss suggested a pathological response (Supplementary Figure 9B). Numerous clusters of LCMV+ cells and inflammatory myeloid cells (Ly6C+ MHC-II+) were seen around blood vessels (Figure 6C) (of note, Ly6c stains both blood vessels and monocytes). This indicated that STAT1 was important in myeloid cells to control

viral load. To more specifically target MM, we used Cd163-Cre : Stat1$^{fl/fl}$ mice. Intravenous infection of those mice with LCMV resulted in a strong recruitment of inflammatory cells in the meninges (Figure 6D), and an increased viral load (Figure 6E) compared to controls. Imaging of the meninges of Cd163-Cre : Stat1$^{fl/fl}$ mice revealed clusters of LCMV+ cells, surrounded by a massive number of infiltrating Ly6c+ monocytes (Figure 6F). Mice did not succumb to the infection (Supplementary Figure 9D) although we noted a trend towards weight loss (Supplementary Figure 9C). To know whether the antiviral effect of STAT1 in MM was dependent on chemokine release and consequent immune cells recruitment, we blocked T cell infiltration using an anti-integrin regimen (anti-LFA1 and anti-VLA4) in Cd163-Cre : Stat1$^{fl/fl}$ mice and littermate controls. This efficiently reduced CD8+ T cell recruitment in the meninges compared to isotype-treated animals (Figure 6G and Supplementary Figure 9E-F). LCMV viral load was still significantly elevated in Cd163-Cre : Stat1$^{fl/fl}$ mice compared to controls (Figure 6H). This indicated that Stat1 in MM was important to block viral spread by acting locally. Of note, after LCMV infection, the quasi absence of MHC-II+ MM upon Stat1 deletion in the aforementioned models suggests that MHC-II+ MM are derived from maturation of MHC-II- MM upon exposure to IFNγ. We next evaluated the role of viral sensing in MM, and performed bone-marrow chimeras of MAVS$^{-/-}$ mice and controls. LCMV infection in MAVS-deficient chimeric mice was characterized by a trend towards lower number of CD8+ T cells in the meninges (Supplementary Figure 9G) which correlated with an increase viral load in the brain (Supplementary Figure 9H). As MAVS has been reported to play a role in CD8+ T cell antiviral functions [25], we performed CD8+ T cell depletion (using CD8-depleting antibody at days 3 and 5 post-infection) to exclude the intrinsic role of MAVS in CD8+ T cells in this model. CD8+ T cells numbers were efficiently reduced after treatment (Supplementary Figure 9I), and viral loads in the brain became comparable between WT and MAVS$^{-/-}$ chimeras, suggesting that MAVS was require for CD8+ T cells, but not MM, antiviral functions (Supplementary Figure 9J). Of note, LCMV loads were higher in the spleen but not in the brain, suggesting that increased peripheral load does not necessarily translate into increased CNS viral (Supplementary Figure 9J). Overall, this data indicate that MM play their antiviral function through STAT1 (thus presumably through antiviral cytokines), not through MAVS (thus presumably not through intrinsic viral detection), which fits with the low proportion of LCMV+ infected MM.

Loss of age-dependent MHC-II+ MM results in viral spread

To more specifically evaluate the contribution of age-dependent MM to viral control, we developed four different strategies aiming at preferentially depleting MHC-II+ cells. First, we took advantage of the LPS-induced contraction of the MHC-II+ MM population (Figure 2K and Supplementary Figure 10A). Following LPS treatment, LCMV was injected in the vasculature.

Six days later, meningeal immune response and viral loads revealed a loss of viral control (Figure 7A and Supplementary Figure 10B). Second, we compared viral spread in the CNS of 4 months and 1 month-old mice, as younger mice have less MHC-II+ MM. Consistent with our previous results, viral loads were higher in young mice (Figure 7B) which correlated with higher inflammation in the meninges (Supplementary Figure 10C). Third, we performed MHC-II+ MM depletion using Timd4-Cre : R26-LSL-hDTR mice. Timd4 is expressed in MHC-II+ and MHC-II- MM (brainimmuneatlas.org), but empirically we found that following DT injection, MHC-II+ MM were more efficiently eliminated by the toxin, resulting in a partial loss of MHC-II+ MM with minimal inflammation (Figure 7C, Supplementary Figure 10D). LCMV infection in MHC-II+ depleted mice resulted in an increased viral load in the brain (Figure 7D) which correlated with a trend towards increased meningeal infiltration of CD8+ T cells (Supplementary Figure 10E). Of note, viral load was also increased in the spleen compared to littermate controls, although to a lesser extent than in the brain (Supplementary Figure 10F). Fourth, we noticed that in LysM-Cre : Csfr1-LSL-DTR mice injected with DT, macrophage depletion was followed by macrophage repopulation within a week (Supplementary Figure 11A-D). When we blocked monocyte recruitment using anti-integrin blockade regimen, repopulation was preferentially performed through local proliferation of MHC-II- MM with minimal off-target effects (Supplementary Figure 11A-D and 12A). The meningeal macrophage landscape was thus reminiscent of neonatal mice and we refer to these mice as ‘rejuvenated’ mice. Infection with LCMV resulted in a significant increase in viral load in ‘rejuvenated’ mice compared to controls (Figure 7F) with minimal inflammation (Supplementary Figure 12B). Of note, spleen viral loads were also increased in ‘rejuvenated’ mice (Supplementary Figure 12C). To confirm the antiviral role of MHC-II+ MM, we measured viral detection by qPCR in sorted MHC-II+ and MHC-II- macrophage populations at day 1 and day 2 after infection. Of note, we did not look at later timepoints as MHC-II could be upregulated by IFNγ in the MHC-II-population after infection and down-regulated in the MHC-II+ population as seen after LPS (Figure 2H), thus misleading the analysis. Interestingly, LCMV was detected in both macrophage populations, but with different kinetics (Supplementary Figure 13). MHC-II+ were more infected than MHC-II- cells by LCMV at day 1, which is consistent with their increased capacity of taking up blood-derived compounds. However, they quickly quenched viral replication, consistent with their metabolic shut-down. On the opposite, MHC-II+ cells became more infected (Supplementary Figure 13). This is consistent with their increased metabolic and biosynthetic response, which makes MHC-II- cells efficient viral factories. All together, these results indicate that age-dependent MHC-II+ MM are important to control viral load in the CNS following a peripheral infection.

Discussion

Recent data suggest that immune responses in the CNS are important players of neurocognition and neuropathology. The CNS is protected by highly vascularized membranes, the meninges, that contain at least two main macrophage populations (neonatal MHC-II- and age-dependent MHC-II+), of elusive functions. Using novel pharmacological and genetic approaches, we show that MM are crucial in blocking fatal neuroinfection. This protection relies more on cytokine signaling through Stat1 than on intrinsic viral detection through MAVS. In addition, the age-dependent, MHC-II+ macrophage population, seems to play a major role in this protection.

MHC-II- MM are prevalent in neonates, and MHC-II+ MM progressively appear over time. The prevalence of MHC-II+ MM in primate samples and their similar disposition suggests that MM have a conserved role in mammals. The appearance of MHC-II+ MM over time is linked with a recruitment of blood-derived cells that occurs under homeostatic conditions, as we have shown in this study and as previously reported for dural macrophages [4] and choroid plexus macrophages [4]. Alternatively, as the bone marrow of the skull has been shown to be a myeloid reservoir, it is possible that monocytes directly seed the meninges from the bone-marrow [8]. Progressive enrichment of MHC-II+ macrophage population has been observed across multiple tissues [26]. Which factors could promote MHC-II+ MM increase under homeostasis? The microbiota is part of the answer [4], but preliminary data from our lab indicate that other factors including caloric intake and T cell increase, are likely to play a role (unpublished results). Increase of MHC-II and MHC-I is coherent with the theory of inflammaging [27], which associates low level of inflammation with detrimental outcome, including cognitive functions [28, 29]. However, our study sheds light on the positive role of age-dependent MHC-II+ MM in surveying the brain borders, which is beneficial during infections.

Loss of resident macrophages upon challenge has been described in both lymphoid and non-lymphoid tissues [30, 31], although the exact function and mechanisms underlying this phenomenon are still unclear [32]. Upon peripheral challenge, we first noticed a decrease of MHC-II+ MM. This could be linked with MHC-II down-regulation, migration of MHC-II+ cells, death of MHC-II+ MM, or a combination thereof. Transcriptomic data indicate a down-regulation of MHC-II in the MHC-II+ MM population, although the loss of MHC-II+ MM population would result in an apparent ‘down-regulation’ of MHC-II related genes. Although dissecting the underlying mechanisms is beyond the scope of this manuscript, this should provide further understanding of the biology of those cells. In addition, response of both MM populations was clearly distinct, with only a third of their transcriptomic changes being shared. The transcriptomic changes of the MHC-II- populations were more drastic, and included upregulation of metabolic processes (respiration and biosynthesis). Interestingly, MHC-II- downregulated homeostatic functions, which were mainly linked with tissue nurturing and

development. In contrast, the major transcriptomic changes in the MHC-II+ MM population involved downregulation of metabolic processes and upregulation of IL1- and death-related pathways. This suggests that several subpopulations of tissue-resident macrophages coexist, and that the tissue-nurturing, neonatal, MHC-II- MM population is progressively replaced by more inflammatory, anti-microbial macrophages.

Most of the studies focusing on meningitis and encephalitis used intracranial injections of the pathogen to achieve sufficient disease penetrance, which by-passed the initial events potentially blocking CNS invasion [21]. Using the more natural route of infection (hematogenous), we analyzed the response of the barrier tissue to peripheral infection. This novel infection model resulted in a transient and asymptomatic infection. LCMV injected in the vasculature infected the meninges and the parenchyma at low levels before being cleared.

PLX treatment has been useful to deplete body macrophages, including microglia. Using a transcranial drug-delivery approach, we were able to deplete barrier macrophages without affecting microglia. This resulted in the death of LCMV-infected mice. Because macrophages in the pial meninges were also affected by the PLX treatment, it will be important to generate new tools to be able to dissect the role of dural versus pial macrophages, and within dural macrophages, to dissect the role of CD206+ (mostly studied in this manuscript) and CD206- macrophages (minor population).

Genetic mouse models to study microglia have been developed [33, 34] but tools to study barrier macrophages are scarce and not broadly used [34, 35]. The role of perivascular macrophages in viral and bacterial infection has been mainly assessed using clodronate which is inflammatory and non-specific to resident macrophages, and might bias the results [36, 37, 38, 39]. Using novel Cd163-Cre mice, we uncovered the role of MM in control of neuroinfection. The higher mortality rate found upon genetic depletion of MM compared to pharmacological depletion could be linked to a higher peripheral viral load in Cd163-Cre : Csf1r-LSL-DTR and to low-grade inflammatory effects of the DT, indicating the importance of combining both pharmacological and genetic methods to provide definitive conclusions.

Outcome of the infection with the LCMV strain used in this study depends both on intrinsic sensing through MAVS pathway [24] and IFN-response through STAT1 pathway [23]. Our data indicate that MM may not be important as primary sensors of infection, but rather act as an amplifier to block further infection, which is consistent with their numerous cytokine receptors [20]. Whether Stat1 plays a role in MHC-II+ or MHC-II- MM is unknown due to the lack of genetic tools to perform conditional KO in those populations. However, as MHC-II+ MM population undergoes contraction, it is likely that IFNs are mainly acting on the MHC-II- MM. Moreover, because Stat1 deletion in meningeal macrophages do not lead to fatal meningitis, other mechanisms are probably involved in their antiviral functions.

The discovery of macrophage ontogeny led to the distinction of resident versus infiltrating macrophages [26, 40, 41]. Tissue-resident macrophages have regulatory properties which contribute to tissue repair [42], but can also promote tumor progression [42]. However, the functions of the subpopulations of tissue-resident macrophages is less clear, mainly because of the lack of tools to selectively deplete each subpopulation. In particular, the role of MHC-II+ versus MHC-II-, or peripherally-derived versus embryonic macrophages, is still controversial. Using 4 different models to target MHC-II+ MM, we show that their loss is sufficient to increase viral spread into the CNS. This contrasts with their apparent contraction upon challenge. We hypothesize that this contraction is actually part of the local antiviral response, by quickly releasing alarmins and IL1, or by shutting down viral replication and subsequent spread to stromal cells. After this initial phase, the few MHC-II- MM that become infected probably depend on IFN-signaling to quench viral biosynthesis and release antiviral compounds. Our transcriptomic data suggest that neonatal, MHC-II- MM, provide trophic support for the meningeal tissue, the bone and the brain. This might be associated with a high metabolic biosynthetic response allowing quick adaptation and resistance to chemical, radiation and microbial stress. This could come at the risk of also supporting viral biosynthesis, especially in the absence of IFNs. It will be important to generate tools to address the specific role of MHC-II- MM. In contrast, MHC-II+ MM, that are acquired over time, can be reconstituted from blood monocytes, and might be more important to fight against microbial compounds, even if this is at the cost of their survival.

Overall, our study unraveled the key role of MM in protecting the brain borders. Age-depedent MM were crucial at early time points to block viral infection which led to a decrease of MHC-II+ MM, while IFNs allowed MM to counteract viral spread. This unraveled key cellular pillars of neuroinvasion that have been elusive for decades. As MHC-II+ MM appear after the neonatal period, this study should also set the ground for understanding the high susceptibility of neonates to CNS infections (e.g. LCMV, HIV, Zika). The data that we obtained did not only increase our understanding of the role of immune sentinels in neuroinvasion but could also provide a rationale for targeting innate immune meningeal sentinels in the clinic.

Legend

Figure 1. MM populations inhabit mouse and primate meninges

A. A representative maximal projection of a confocal z-stack shows a meningeal whole mount from an aged baboon (top) and an adult mouse (bottom). The image shows a region of the lobe with MHC-II stain (red) and IBA1 or CD206+ stain (green). Scale bar: 100 µm. Image is representative of 4 baboons and 5 mice.

B. Baboon meninges were cleared and stained for IBA1 and MHC-II. The proportion of MHC-II+ MM in baboons is indicated. Bar graphs show the mean ± s.e.m. Data are representative of four baboons (2 areas per baboon were counted).

C. At different ages, expression of MHC-II and MHC-I by MM was assessed by flow cytometry on mouse meninges. MM were gated on LiveDead- CD45+ CD11b+ Thy1.2- Ly6C- Ly6G- CD11c- CD64+ CD206+ cells. Bar graphs show the mean ± s.e.m. and asterisks denote statistical significance (*P<0.05, ***P<0.0001; Pearson correlation test, with “r” correlation coefficient indicated). Data are representative of six independent experiments with 3 mice (d120, d150, d210), 6 mice (d10, d14), 5 mice (d60), 10 mice (d30) and 15 mice (d90) per group.

D. Representative maximal projection of meningeal whole mounts from B6 mice injected intravenously with 10 kDa fluorescent dextran 30 min prior, showing expression of CD31+ (blue, vessels), CD206+ (red, MM) and dextran (green). The insets show an area of the right parietal lobe (left) and of the superior sagittal sinus (right). Scale bar : 1 mm, 200 µm. Data are representative of two independent experiments with 2 mice (Control) and 3 mice (Dextran) per group. IL: interparietal lobe; PL: parietal lobe; FL: frontal lobe; SSS: superior sagittal sinus; TS: transverse sinus.

E. Dextran uptake was quantified in MHC-II+ and MHC-II- MM (identified with CD206). Intensity of dextran fluorescence was significantly higher in MHC-II+ MM. Bar graphs show the mean ± s.e.m. for the indicated groups and asterisks denote statistical significance (*P<0.05; unpaired two-tailed Student’s t test). Data are representative of two independent experiments with 2 mice (Control) and 3 mice (Dextran) per group.

F. Dextran uptake by MHC-II+ MM (red) and MHC-II- MM (green) subsets was visualized by histocytometry. For both macrophage subsets, CD206+ surfaces positive for dextran (‘Dextran +’) and negative for dextran (‘Dextran-‘) were plotted on an xy coordinate scale to identify their anatomical distribution on meningeal whole mounts. Data are representative of two independent experiments with 2 mice (Control) and 3 mice (Dextran) per group.

Figure 2.

A. UMAP representation of nucleated meningeal cells (7,035 cells). MM are indicated by the red box. Single-cell RNA sequencing was performed on 4 meningeal samples (from 2 mice injected with PBS and 2 with LPS) using 10X genomics and data was analyzed using Seurat software in combination with public datasets (brainimmuneatlas.org). Clustering was done with 50 dimensionalities of PCA, 30 PC and a resolution of Louvain's algorithm of 2. The 29 resultant clusters were regrouped into 16 cell clusters to facilitate visualization, based on their marker genes.

B. UMAP representation of MM subset (497 cells). The clustering was done with 50 dimensionalities of PCA, 30 PC and a resolution of Louvain's algorithm of 0.3 (left), resulting in 4 clusters. Visualization of H2-Ab1 expression within MM subset (right).

C. Venn diagram of differentially expressed genes (DEGs) in LPS versus PBS conditions (adjusted p-value <0.05, abs(log2FC)>0.25) in MHC-II+ MM and MHC-II- MM.

D-F. Volcano plot of genes expressed in LPS versus PBS conditions in MM (D), MHC-II+ MM (E) and MHC-II- MM (right) obtained with EnhancedVolcano R package.

G-I. Gene Ontology pathways of DEGs in LPS versus PBS condition in total MM (G), MHC-II+ MM (H) and MHC-II- MM (I) obtained with clusterProfiler R package.

J. Violin plot of the expression of MHC-II in MM according to the treatment (PBS or LPS), and proportion of cells positive for H2-Ab1.

K. CD206+ MHC-II+ and MHC-II- macrophage populations were enumerated by flow cytometry 24h after LPS or PBS intravenous injection. MM were gated on LiveDead- CD45+ CD11b+ Thy1.2- Ly6C- Ly6G- CD11c- CD64+, CD206+, with MHC-II subsets. MM counts after LPS injection were normalized to PBS control. Bar graphs show the mean ± s.e.m. and asterisks denote statistical significance (NS=Not Significant, *P<0.05; Kruskall Wallis test followed by Mann-Whitney two-tailed test with Holm-Sidak correction for multiple analysis). Data are representative of 3 independent experiments with 6 mice (PBS) and 8 mice (LPS) per group.

L. MHC-II+ and MHC-II- MM populations were enumerated by flow cytometry 48h after LPS or LCMV intravenous injection. MM were gated on LiveDead- CD45+ CD11b+ Thy1.2- Ly6C- Ly6G- CD11c- CD64+, CD206+, with MHC-II subsets. CD206+ macrophage counts after LCMV injection were normalized to PBS control. Bar graphs show the mean ± s.e.m. and asterisks denote statistical significance (NS=Not Significant, **P<0.01; one-way ANOVA test followed by Holm-Sidak multiple comparison test). Data are representative of 3 independent experiments with 4 mice (PBS) and 6 mice (LCMV) per group.

M-N. K18-hACE2 mice (noted Tg-K18) were infected intranasally with 10^5 PFU of SARS-CoV2 and harvested at 2, 3, 4, 5, 6 and 7 days post-infection. In addition, one control group of K18-hACE2 non-carrier animals ('WT') was intranasally inoculated with 10^5 PFU of SARS-CoV-2 and one control group of K18-hACe2 animals was injected with saline solution (PBS). (M) MHC-II+ MM and MHC-II- MM proportion were enumerated based on IBA1 staining at different timepoints after SARS-CoV2 intranasal infection. Bar graphs show the mean ± s.e.m. and asterisks denote statistical significance (NS=Not Significant, *P<0.05; ****P<0.0001; one-way ANOVA test followed by Holm-Sidak test for pairwise comparison with the PBS control). (N) MM were identified based on IBA1 staining in Tg-K18 mice, depicting loss of MHC-II expression on MM 6 days after infection with SARS-CoV-2 infection. Data are representative of 3 independent experiments with 6 mice (NI D6), 6 mice (WT D6), 8 mice (Tg D2), 2 mice

(Tg D3), 7 mice (Tg D4), 3 mice (Tg D5), 7 mice (Tg D6) and 4 mice (Tg D7) per group, and 1 to 3 regions per mouse were analyzed.

Figure 3. Infection of LCMV via the intravenous route leads to a transient infection in the meninges and the brain.

A, B. LCMV mRNA levels were quantified by quantitative PCR (Q-PCR) in the meninges (A) and brains (B) at days 1, 6 and 30 post-infection and compared to mock-infected mice. LCMV RNA levels were significantly higher than controls in both the meninges and brains starting at day 1 and reaching a peak at day 6. Bar graphs show the mean ± s.e.m. and asterisks denote statistical significance (NS=Not Significant; ***P<0.001; ****P<0.0001; Kruskall-Wallis test with Dunn's post-hoc test). Data are representative of 4 independent experiments with 12 mice (naive) and 6 mice (d1, d6, d30) per group.

C. At day 6 post LCMV infection, LCMV+ MM (gated on LiveDead- CD45+ CD11b+ Thy1.2- Ly6C- Ly6G- CD11c- CD64+ CD206+ cells) were enumerated, indicating low levels of infection. Bar graphs show the mean ± s.e.m. and asterisks denote statistical significance (*P<0.05; Unpaired two-tailed Student's *t*-test). Data are representative of 2 independent experiments with 4 (PBS) and 3 (LCMV) mice per group.

D,E. . At day 6 post LCMV infection, meningeal infiltrating cells were enumerated (D) Neutrophils (gated on LiveDead− CD45+ Thy1.2– CD11b+ Ly6C− Ly6G+ cells), monocytes (gated on LiveDead− CD45+ Thy1.2– CD11b+ Ly6G− Ly6C+ cells) and CD8+ T cells (gated on LiveDead− CD45+ CD11b+ Thy1.2+ CD8+ cells) were present in the meninges, with monocytes and CD8+ T cells numbers increasing after LCMV infection when compared to mock-infected controls. (E) MHC-I expression on MM (gated on LiveDead- CD45+ CD11b+ Thy1.2- Ly6C- Ly6G- CD11c- CD64+ CD206+ cells) was increased after LCMV infection. Bar graphs show the mean ± s.e.m. and asterisks denote statistical significance (NS=Not Significant; **P<0.01, ****P<0.0001; one-way ANOVA test with Holm-Sidak post-hoc test for D; Unpaired two-tailed Student's *t*-test for E). Data are representative of 2 independent experiments with 7 (PBS) and 8 (LCMV) mice per group.

F,G. B6 mice were injected intravenously with P14-OFP+ CD8+ T cells and with either PBS or LCMV at day 6 post-infection. (F) Immune clusters of MHC-II+ cells were analyzed and quantified by histocytometry in interparietal, parietal and frontal regions of the meninges. The density of clusters was significantly increased in LCMV-infected mice in all regions of the meninges (**P<0.01; Kruskall Wallis test followed by Mann-Whitney two-tailed test with Holm-Sidak correction for multiple analysis). Bar graphs show the mean ± s.e.m. for the indicated groups. (G) Maximal projections of meningeal whole mounts from B6 mice showing MHC-II (blue), CD11b (green) and P14-OFP+ T cells (red) expression. Scale bar: 1mm. Magnified

area highlighted in the red box are shown underneath. Scale bar: 50 μm. Data are representative of 2 independent experiments with 7 mice per group.

Figure 4. MM depletion through pharmacological PLX increases susceptibility to fatal meningitis.

A. B6 mice were injected transcranially with a CSF1-R antagonist (PLX3397) to deplete MM and compared to mock-injected mice (gel). Neutrophils (gated on LiveDead- CD45+ CD11b+ Thy1.2- Ly6C- Ly6G+ cells), monocytes (gated on LiveDead- CD45+ CD11b+ Thy1.2- Ly6C+ Ly6G-), MM (gated on LiveDead- CD45+ CD11b+ Thy1.2- Ly6C- Ly6G- CD11c- CD64+, with CD206 and MHC-II subsets), CD11b+ DC (gated on LiveDead- CD45+ CD11b+ Thy1.2- Ly6C- Ly6G- CD11c+ MHC-II+ cells), CD11b- DC (gated on LiveDead- CD45+ CD11b+ Thy1.2- CD11b- CD11c+ MHC-II+ cells), CD8+ T cells (gated on LiveDead- CD45+ CD11b+ Thy1.2+ CD8+ cells), CD4+ T cells (gated on LiveDead- CD45+ CD11b+ Thy1.2+ CD4+ cells), NK cells (gated on LiveDead- CD45+ NK1+ Thy1.2-), NKT cells (gated on LiveDead- CD45+ CD11b+ Thy1.2+ NK1+ cells) and other T cells (gated on LiveDead- CD45+ CD11b+ Thy1.2+ CD4- CD8- NK1-) were assessed by flow cytometry. Bar graphs show the mean ± s.e.m and asterisks denote statistical significance (NS=Not Significant; **P<0.01; ****P<0.0001; Kruskall Wallis test followed by Mann-Whitney two-tailed test with Holm-Sidak correction for multiple analysis). Data are representative of 5 independent experiments with 21 mice (gel) and 20 mice (PLX) mice per group. A representative FACS plot of MM in Control and PLX-treated is shown on the right.

B. MM macrophage density was assessed on whole-mount images and shows reduction of numbers in both the lobes and sutures after PLX treatment. Bar graphs show the mean ± s.e.m and asterisks denote statistical significance (NS=Not Significant, *P<0.05, **P<0.01; Kruskall Wallis test followed by Mann-Whitney two-tailed test with Holm-Sidak correction for multiple analysis). Data are representative of 3 independent experiments with 7 mice (Gel) and 12 mice (PLX) per group.

C. Maximal projection of meningeal whole mounts from PLX-treated mice were stained for CD206 (green), Ly6C (blue) and MHC-II (red). Scale bar: 1mm. The insets show a region of the suture and of the lobe. Scale bar: 100 μm. Data are representative of 3 independent experiments with 7 mice (Gel) and 12 mice (PLX) per group.

D. Brain macrophages (perivascular macrophages, choroid plexus macrophages and pial macrophages), gated on LiveDead- CD45+ CD11b+ Thy1.2- Ly6C- Ly6G- CD64+ CD11c- CD206+ were assessed by flow cytometry. Bar graphs show the mean ± s.e.m. (NS=Not Significant; Mann-Whitney two-tailed test). Data are representative of 2 independent experiments with 10 mice (gel) and 9 mice (PLX) per group.

E. Density of pial macrophages was assessed on brain surfaces stained with CD206 for macrophage quantification in control and PLX-treated mice. Bar graphs show the mean ± s.e.m. (****P<0.0001; Unpaired two-tailed Student's *t*-test). Data are representative of one experiment with 5 mice per group, 2 lobes per mouse and 2 to 3 regions per lobe.

F. Microglia (gated on LiveDead- CD45+ CD11b+ Thy1.2- Ly6C- Ly6G- CD64+ CD11c-) were assessed by flow cytometry (left panel). Bar graphs show the mean ± s.e.m. (NS=Not Significant; Mann-Whitney two-tailed test). Data are representative of 3 independent experiments with 13 mice (gel) and 12 mice (PLX) per group. Maximal projection of brain sections from PLX treated mice and controls were stained for IBA1 (green) and DAPI (blue) (left) (middle panel). Scale bar: 100 µm. Microglial density was quantified (right panel). Bar graphs show the mean ± s.e.m. (NS=Not Significant; Unpaired two-tailed Student's *t*-test). Data are representative of 3 independent experiments with 10 mice per group.

G. Blood neutrophils (gated on LiveDead− CD45+ Thy1.2– CD11b+ Ly6C− Ly6G+ cells) and monocytes (gated on LiveDead- CD45+ CD11b+ Thy1.2- CD115+ Ly6G-) were quantified by flow cytometry. Bar graphs show the mean ± s.e.m. (NS=Not Significant; Kruskall Wallis test followed by Mann-Whitney two-tailed test with Holm-Sidak correction for multiple analysis). Data are representative of 3 independent experiments with 13 mice (Control) and 12 mice (PLX) per group.

H. Spleen neutrophils (gated on LiveDead− CD45+ Thy1.2– CD11b+ Ly6C− Ly6G+ cells), monocytes (gated on LiveDead- CD45+ CD11b+ Thy1.2- Ly6C+ Ly6G-) and macrophages (gated on LiveDead- CD45+ CD11b+ Thy1.2- Ly6C- Ly6G- CD64+ cells) were quantified by flow cytometry. Bar graphs show the mean ± s.e.m. (NS=Not Significant, Kruskall Wallis test followed by Mann-Whitney two-tailed test with Holm-Sidak correction for multiple analysis). Data are representative of 3 independent experiments with 13 mice per group.

I. PLX-treated mice were infected with LCMV intravenously. At day 6 post-infection, meningeal neutrophils (gated on LiveDead- CD45+ CD11b+ Thy1.2- Ly6C- Ly6G+ cells), monocytes (gated on LiveDead- CD45+ CD11b+ Thy1.2- Ly6C+ Ly6G-), MM (gated on LiveDead- CD45+ CD11b+ Thy1.2- Ly6C- Ly6G- CD11c- CD64+, CD206+ cells) and CD8+ T cells (gated on LiveDead- CD45+ CD11b- Thy1.2+ CD8+ cells) were enumerated. Bar graphs show the mean ± s.e.m and asterisks denote statistical significance (NS=Not Significant; ***P<0.001; Kruskall Wallis test followed by Mann-Whitney two-tailed test with Holm-Sidak correction for multiple analysis). Data are representative of 2 independent experiments with 9 mice (Control) and 8 mice (PLX) per group.

J. LCMV mRNA levels were quantified by quantitative PCR (Q-PCR) in the brains (left) and spleens (right) of PLX-treated mice, at day 6 post-infection. LCMV mRNA levels were significantly higher in the brain, but not the spleen, of PLX-treated mice compared to controls. Bar graphs show the mean ± s.e.m. and asterisks denote statistical significance (NS=Not

Significant, **P<0.01; Mann-Whitney two-tailed test). Data are representative of two independent experiments with 5 (Gel, Brain) and 5 (PLX, Brain), 9 (Gel, Spleen) and 8 (PLX, Spleen) mice per group.

K. Survival curves of PLX- or mock-injected mice after infection. Macrophage depletion leads to decreased chances of survival. Asterisk denote statistical significance (*P<0.05; Log-rank Mantel Cox test). Data are representative of 3 independent experiment with 14 mice (Gel) and 19 mice (PLX) per group.

L. A representative zoom on whole-mount meninges showing Ly6C+ vessels (red), CD8+ T cells (blue), and LCMV (green) at day 6 post-infection of naive (left), mock-injected (middle) and PLX-treated mice (right). Scale bar: 100 µm. Data are representative of two independent experiment with 2 mouse (NI), 4 mice (Gel) and 4 mice (PLX).

Figure 5. MM genetic depletion increases susceptibility to fatal meningitis

A, B. MM and brain macrophages but not microglia, are targeted by the CD163-Cre reporter. CNS Immune cells of Cd163-Cre : R26-LSL-YFP mice were analyzed by flow cytometry. (A) Bar graphs show the percentage of YFP+ in neutrophils (gated on LiveDead- CD45+ CD11b+ Thy1.2- Ly6C-Ly6G+ cells), monocytes (gated on LiveDead- CD45+ CD11b+ Thy1.2- Ly6C+ Ly6G-, with MHC-II+ and MHC-II- subsets), MM (gated on LiveDead- CD45+ CD11b+ Thy1.2- Ly6C- Ly6G- CD11c- CD64+, with CD206 and MHC-II subsets), CD11b+ DC (gated on LiveDead- CD45+ CD11b+ Thy1.2- Ly6C- Ly6G- CD11c+ MHC-II+ cells), CD11b- DC (gated on LiveDead- CD45+ CD11b- Thy1.2- CD11c+ MHC-II+ cells), CD8+ T cells (gated on LiveDead- CD45+ CD11b- Thy1.2+ CD8+ cells), CD4+ T cells (gated on LiveDead- CD45+ CD11b- Thy1.2+ CD4+ cells), NK cells (gated on LiveDead- CD45+ NK1+ Thy1.2-), NKT cells (gated on LiveDead- CD45+ CD11b- Thy1.2+ NK1+ cells), other T cells (gated on LiveDead- CD45+ CD11b- Thy1.2+ CD4- CD8- NK1-) and CD45neg cells (gated on LiveDead- CD45-). Bar graphs show the mean ± s.e.m. for the indicated groups, and asterisks denote statistical significance (*P<0.05, **P<0.01, ****P<0.0001; Kruskall Wallis test followed by Mann-Whitney two-tailed test with Holm-Sidak correction for multiple analysis). Data are representative of 4 independent experiments with 8 mice (Control) and 17 mice (Cd163-Cre : R26-LSL-YFP) per group. A representative FACS plot of YFP expression in MM of control versus Cd163-Cre : R26-LSL-YFP mice is shown (right). (B) Bar graphs show the percentage of YFP+ in microglia (gated on LiveDead- CD45int CD11b+ Thy1.2- Ly6C- Ly6G- CD11c- CD64int), neutrophils (gated on LiveDead- CD45+ CD11b+ Thy1.2- Ly6C- Ly6G+ cells), monocytes (gated on LiveDead- CD45+ CD11b+ Thy1.2- Ly6C+ Ly6G- and subdivided using MHC-II), MM (gated on LiveDead- CD45+ CD11b+ Thy1.2- Ly6C- Ly6G- CD11c- CD64+, with CD206 and MHC-II subsets), CD11b+ DC (gated on LiveDead- CD45+ CD11b+ Thy1.2- Ly6C- Ly6G- CD11c+ MHC-II+ cells), CD11b- DC (gated on LiveDead- CD45+ CD11b- Thy1.2- CD11c+ MHC-II+

cells), CD8+ T cells (gated on LiveDead- CD45+ CD11b- Thy1.2+ CD8+ cells), CD4+ T cells (gated on LiveDead- CD45+ CD11b- Thy1.2+ CD4+ cells), NK cells (gated on LiveDead- CD45+ NK1+ Thy1.2-), NKT cells (gated on LiveDead- CD45+ CD11b- Thy1.2+ NK1+ cells), other T cells (gated on LiveDead- CD45+ CD11b- Thy1.2+ CD4- CD8- NK1-) and CD45neg cells (gated on LiveDead- CD45-). Bar graphs show the mean ± s.e.m. for the indicated groups, and asterisks denote statistical significance (NS=Not Significant, **P<0.01, ***P<0.001, Kruskall Wallis test followed by Mann-Whitney two-tailed test with Holm-Sidak correction for multiple analysis). Data are representative of 4 independent experiments with 5 mice (Control) and 17 mice (Cd163-Cre : R26-LSL-YFP) per group. A representative FACS plot of YFP expression in microglia of control versus Cd163-Cre : R26-LSL-YFP mice is shown (right).

C,D. Cd163-Cre : Csf1r-LSL-DTR mice were administered 100ng of diphteria toxin (DT) subcutaneously on two consecutive days and analyzed by flow cytometry for meningeal immune cells in the meninges (C) and the brain (D). (C) Bar graphs show the number of neutrophils (gated on LiveDead- CD45+ CD11b+ Thy1.2- Ly6C- Ly6G+ cells), monocytes (gated on LiveDead- CD45+ CD11b+ Thy1.2- Ly6C+ Ly6G- and subdivided using MHC-II), MM (gated on LiveDead- CD45+ CD11b+ Thy1.2- Ly6C- Ly6G- CD11c- CD64+, with CD206 and MHC-II subsets), CD11b+ DC (gated on LiveDead- CD45+ CD11b+ Thy1.2- Ly6C- Ly6G- CD11c+ MHC-II+ cells), CD11b- DC (gated on LiveDead- CD45+ CD11b- Thy1.2- CD11c+ MHC-II+ cells), CD8+ T cells (gated on LiveDead- CD45+ CD11b- Thy1.2+ CD8+ cells), CD4+ T cells (gated on LiveDead- CD45+ CD11b- Thy1.2+ CD4+ cells), NK cells (gated on LiveDead- CD45+ NK1+ Thy1.2-) and NKT cells (gated on LiveDead- CD45+ CD11b- Thy1.2+ NK1+ cells). Bar graphs show the mean ± s.e.m. for the indicated groups, and asterisks denote statistical significance (NS=Not Significant, **P<0.01, ****P<0.0001, Kruskall Wallis test followed by Mann-Whitney two-tailed test with Holm-Sidak correction for multiple analysis). MM were efficiently depleted by the treatment. Data are representative of 4 independent experiments with 12 mice (Control) and 10 mice (Cd163-Cre : Csf1r-LSL-DTR) per group. (D) Bar graphs show the number of microglia (gated on LiveDead- CD45int CD11b+ Thy1.2- Ly6C- Ly6G- CD11c- CD64int), neutrophils (gated on LiveDead- CD45+ CD11b+ Thy1.2- Ly6C- Ly6G+ cells), monocytes (gated on LiveDead- CD45+ CD11b+ Thy1.2- Ly6C+ Ly6G- and subdivided using MHC-II), MM (gated on LiveDead- CD45+ CD11b+ Thy1.2- Ly6C- Ly6G- CD11c- CD64+, with CD206 and MHC-II subsets), CD11b+ DC (gated on LiveDead- CD45+ CD11b+ Thy1.2- Ly6C- Ly6G- CD11c+ MHC-II+ cells), CD11b- DC (gated on LiveDead- CD45+ CD11b- Thy1.2- CD11c+ MHC-II+ cells), CD8+ T cells (gated on LiveDead- CD45+ CD11b- Thy1.2+ CD8+ cells), CD4+ T cells (gated on LiveDead- CD45+ CD11b- Thy1.2+ CD4+ cells), NK cells (gated on LiveDead- CD45+ NK1+ Thy1.2-) and NKT cells (gated on LiveDead- CD45+ CD11b- Thy1.2+ NK1+ cells). Bar graphs show the mean ± s.e.m. for the indicated groups, and asterisks denote statistical significance (NS=Not Significant; Kruskall

Wallis test followed by Mann-Whitney two-tailed test with Holm-Sidak correction for multiple analysis). Data are representative of 4 independent experiments with 11 mice (Control) and 10 mice (Cd163-Cre : Csf1r-LSL-DTR) per group.

E, F. Cd163-Cre : Csf1r-LSL-DTR mice were subjected to DT injections as previously described, infected with LCMV and analyzed by flow cytometry (meninges) and RT-qPCR (brain) 6 days later. (E) Bar graphs show the number of neutrophils (gated on LiveDead- CD45+ CD11b+ Thy1.2- Ly6C-Ly6G+ cells), monocytes (gated on LiveDead- CD45+ CD11b+ Thy1.2- Ly6C+ Ly6G-, with MHC-II+ and MHC-II- subsets), MM (gated on LiveDead- CD45+ CD11b+ Thy1.2- Ly6C- Ly6G- CD11c- CD64+, with CD206 and MHC-II subsets), CD11b+ DC (gated on LiveDead- CD45+ CD11b+ Thy1.2- Ly6C- Ly6G- CD11c+ MHC-II+ cells), CD11b- DC (gated on LiveDead- CD45+ CD11b- Thy1.2- CD11c+ MHC-II+ cells), CD8+ T cells (gated on LiveDead- CD45+ CD11b- Thy1.2+ CD8+ cells), CD4+ T cells (gated on LiveDead- CD45+ CD11b- Thy1.2+ CD4+ cells), NK cells (gated on LiveDead- CD45+ NK1+ Thy1.2-), NKT cells (gated on LiveDead- CD45+ CD11b- Thy1.2+ NK1+ cells) and other T cells (gated on LiveDead- CD45+ CD11b- Thy1.2+ CD4- CD8- NK1-). Bar graphs show the mean ± s.e.m. for the indicated groups, and asterisks denote statistical significance (NS=Not Significant, Kruskall Wallis test followed by Mann-Whitney two-tailed test with Holm-Sidak correction for multiple analysis). Data are representative of 3 independent experiments with 8 mice (Control) and 4 mice (Cd163-Cre : Csf1r-LSL-DTR) per group. (F) LCMV mRNA levels were quantified by quantitative PCR (Q-PCR) in the brains of Cd163-Cre : Csf1r-LSL-DTR mice injected with DT, at day 6 post LCMV infection. LCMV mRNA levels were significantly higher than in mock-injected mice. Bar graphs show the mean ± s.e.m. and asterisks denote statistical significance (****P<0.0001; Mann-Whitney two-tailed test). Data are representative of 2 independent experiments with 4 mice (Control) and 5 mice (Cd163-Cre : Csf1r-LSL-DTR) per group.

G. Survival curves of Cd163-Cre : Csf1r-LSL-DTR or control mice after infection. Macrophage depletion leads to decreased chances of survival. Asterisk denote statistical significance (**P<0.01; Log-rank Mantel Cox test). Data are representative of 2 independent experiment with 13 mice (Control) and 10 mice (Cd163-Cre : Csf1r-LSL-DTR) per group.

H. Maximal projection of meningeal whole mounts from Cd163-Cre : Csf1r-LSL-DTR injected with DT prior to infection, showing LCMV (green) and IBA1 (red) expression at day 3 and day 6 post-infection. Meninges of non-infected and WT mice at day 3 and day 6 post-infection controls are shown the left. Scale bar: 1mm. Magnified areas highlighted in white boxes are shown in lower panel. Scale bar: 50 µm. Data are representative of 3 independent experiments with 5 mice (PBS D3), 2 mice (WT D3), 2 mice (CD163-Cre : Csf1r-LSL-DTR D3), 7 mice (WT d6), 8 mice (CD163-Cre : Csf1r-LSL-DTR D6).

Figure 6. MM antiviral action requires Stat1

A. At day 6 post-infection, meningeal immune cells of LysM-Cre : Stat1$^{fl/fl}$ mice were analyzed by flow cytometry to quantify the number of monocytes (gated on LiveDead- CD45+ CD11b+ Thy1.2- Ly6C+ Ly6G-, with MHC-II+ and MHC-II- subsets), MM (gated on LiveDead- CD45+ CD11b+ Thy1.2- Ly6C- Ly6G- CD11c- CD64+, with CD206 and MHC-II subsets), and CD8+ T cells (gated on LiveDead- CD45+ CD11b- Thy1.2+ CD8+ cells). Bar graphs show the mean ± s.e.m. and asterisks denote statistical significance (NS=Not Significant, **P<0.01, ****P<0.0001; Kruskall Wallis test followed by Mann-Whitney two-tailed test with Holm-Sidak correction for multiple analysis). CD206+ MHC-II+ macrophage numbers were reduced and CD8+ T cells numbers were increased. Data are representative of 3 independent experiments with 20 mice (Control) and 8 mice (LysM-Cre : Stat1$^{fl/fl}$) per group.

B. LCMV mRNA levels were quantified by quantitative PCR (Q-PCR) in the brains of LysM-Cre : Stat1$^{fl/fl}$ mice at day 6 post-infection. LCMV mRNA levels were significantly higher than in control mice. Bar graphs show the mean ± s.e.m. and asterisks denote statistical significance (****P<0.0001; Mann-Whitney two-tailed test). Data are representative of 4 independent experiments with 18 mice (Control) and 9 mice (LysM-Cre : Stat1$^{fl/fl}$) per group.

C. Maximal projection of meningeal whole mounts from LysM-Cre : Stat1$^{fl/fl}$ at day 6 post-infection show numerous clusters of LCMV (green) surrounded by monocytes (red) and MHC-II+ cells (blue) compared to littermate controls. Magnified areas of highlighted white boxes show viral patches in LysM-Cre : Stat1$^{fl/fl}$ mice. Data are representative of 2 independent experiments with 2 mice per group. Scale bar: 1mm (full meninges) and 200 µm (inset).

D. At day 6 post-infection, meningeal immune cells of Cd163-Cre : Stat1$^{fl/fl}$ were analyzed by flow cytometry to quantify the number of monocytes (gated on LiveDead- CD45+ CD11b+ Thy1.2- Ly6C+ Ly6G-, with MHC-II+ and MHC-II- subsets), MM (gated on LiveDead- CD45+ CD11b+ Thy1.2- Ly6C- Ly6G- CD11c- CD64+, CD206+ with MHC-II subsets) and CD8+ T cells (gated on LiveDead- CD45+ CD11b- Thy1.2+ CD8+ cells). The number of monocytes and CD8+ T cells is significantly increased in Cd163-Cre : Stat1$^{fl/fl}$ mice compared to controls. Bar graphs show the mean ± s.e.m. and asterisks denote statistical significance (NS=Not Significant, ***P<0.001, ****P<0.0001; Kruskall Wallis test followed by Mann-Whitney two-tailed test with Holm-Sidak correction for multiple analysis). Data are representative of 6 independent experiments with 25 mice (Control) and 15 mice (Cd163-Cre : Stat1$^{fl/fl}$) per group.

E. LCMV mRNA levels were quantified by quantitative PCR (Q-PCR) in the brains of Cd163-Cre : Stat1$^{fl/fl}$ mice at day 6 post-infection. LCMV mRNA levels were significantly higher than in control mice. Bar graphs show the mean ± s.e.m. and asterisks denote statistical significance (****P<0.0001; Mann-Whitney two-tailed test). Data are representative of 7 independent experiments with 20 mice (Control) and 11 mice (Cd163-Cre : Stat1$^{fl/fl}$) per group.

F. Maximal projection of meningeal whole mounts from Cd163-Cre : Stat1$^{fl/fl}$ at day 6 post-infection show few clusters of LCMV (green) surrounded by monocytes (red) compared to

littermate controls. Data are representative of 3 independent experiments with 6 mice (Control) and 7 mice (Cd163-Cre : Stat1$^{fl/fl}$) per group. Scale bar: 1mm. Magnified areas of highlighted white boxes show viral patches in Cd163-Cre : Stat1$^{fl/fl}$ mice. Scale bar: 1mm (full meninges) and 200 µm (inset).

G, H. Cd163-Cre : Stat1$^{fl/fl}$ mice were injected with blocking antibodies (anti-LFA-1 & anti-VLA-4) at day 3 and day 5 after infection to block infiltration of immune cells into the meninges and study the local, intrinsic antiviral role of MM. (G) At day 6 post-infection, monocytes (gated on LiveDead- CD45+ CD11b+ Thy1.2- Ly6C+ Ly6G-, with MHC-II+ and MHC-II- subsets), MM (gated on LiveDead- CD45+ CD11b+ Thy1.2- Ly6C- Ly6G- CD11c- CD64+, CD206+ with MHC-II subsets), and CD8+ T cells (gated on LiveDead- CD45+ CD11b- Thy1.2+ CD8+ cells) were assessed. T cell infiltration was efficiently blocked. Bar graphs show the mean ± s.e.m. and asterisks denote statistical significance (NS=Not Significant; *P<0.05, ****P<0.0001; Kruskall Wallis test followed by Mann-Whitney two-tailed test with Holm-Sidak correction for multiple analysis).

H. LCMV mRNA levels were quantified by quantitative PCR (Q-PCR) in the brains of Cd163-Cre : Stat1$^{fl/fl}$ mice treated with blocking antibodies, at day 6 post-infection. Cd163-Cre : Stat1$^{fl/fl}$ mice still have an increased viral load compared to littermate controls when treated with blocking antibodies. Bar graphs show the mean ± s.e.m asterisks denote statistical significance (***P<0.001; Mann-Whitney two-tailed test). Data are representative of 2 independent experiments with 11 mice (Control + anti-LFA/VLA) and 10 mice (Cd163-Cre : Stat1$^{fl/fl}$ + anti-LFA/VLA) per group.

Figure 7. MHC-II+ MM block neuroinfection.

A. Mice were subjected to an injection of lipopolysaccharide (LPS) or of saline solution (PBS) before infection with LCMV. At day 6 post-infection, LCMV mRNA was assessed by quantitative PCR (Q-PCR) in brains of mice injected with LPS and compared to controls, showing significantly higher viral load in LPS-injected mice than in PBS-injected mice. Bar graphs show the mean ± s.e.m. (**P<0.01; Mann-Whitney two-tailed test). Data are representative of 2 experiments with 4 mice (PBS) and 6 mice (LPS) per group.

B. Four months-old and 1 month-old mice were injected with LCMV. At day 6 post-infection, LCMV mRNA levels were quantified by quantitative PCR (Q-PCR) in the brains, showing significantly higher viral load in 1-month old mice than in 4-months old mice. Bar graphs show the mean ± s.e.m. and asterisks denote statistical significance (**P<0.01; Mann-Whitney two-tailed test). Data are representative of 3 independent experiments with 11 mice per group.

C, D. Mice were preferentially depleted of MM MHC-II+ before LCMV infection. (C) Timd4-Cre : R26-LSL-hDTR mice and littermate controls were injected transcranially with 100ng of diphteria toxin (DT) on two consecutive days. On the third day, MM (gated on LiveDead-

CD45+ CD11b+ Thy1.2- Ly6C- Ly6G- CD11c- CD64+, with CD206 and MHC-II subsets) were analyzed by flow cytometry, revealing a trend towards a reduction of MHC-II+ MM in Timd4-Cre : R26-LSL-hDTR mice compared to controls, with no changes in the number of MHC-II- MM. Bar graphs show mean ± s.e.m and asterisks denote statistical significance (NS=Not Significant, One-way ANOVA followed by unpaired two-tailed Student's *t*-test with Holm-Sidak test for pairwise comparison). Data are representative of one experiment with 5 mice per group. (D) One day after DT treatment, LCMV was injected intravenously into mice. At day 6 post-infection, LCMV mRNA was assessed by Q-PCR in brains of Timd4-Cre : R26-LSL-hDTR mice and compared with littermate controls. Bar graphs show the mean ± s.e.m. (****P<0.0001, Mann-Whitney two-tailed test). Data are representative of one experiment with 5 mice (Control) and 4 mice (Timd4-Cre : R26-LSL-hDTR) per group.

E, F. Mice were subjected to 'meningeal rejuvenation' before infection with LCMV. (E) LysM-Cre : Csf1r-LSL-DTR mice and littermate controls were injected with 100ng of diphteria toxin (DT) transcranially at days 0 and 1 to deplete myeloid cells and then injected i.v. with blocking antibodies (anti-LFA-1 & anti-VLA-4) at day 2 and day 4 to promote local MHC-II- cells proliferation over MHC-II+ cells infiltration. MM (gated on LiveDead- CD45+ CD11b+ Thy1.2- Ly6C- Ly6G- CD11c- CD64+, with CD206 and MHC-II subsets) were analyzed by flow cytometry at day 7 post DT, revealing a reduction of MHC-II+ MM in 'rejuvenated' mice compared to controls, with no changes in the number of MHC-II- MM. Bar graphs show mean ± s.e.m and asterisks denote statistical significance (NS=Not Significant, **P<0.01; One-way ANOVA followed by unpaired two-tailed Student's *t*-test with Holm-Sidak test for pairwise comparison). Data are representative of 2 independent experiments with 5 mice per group. (F) At day 8 post DT injection, mice were infected with LCMV. LCMV mRNA was assessed by quantitative PCR (Q-PCR) in brains of 'rejuvenated' mice and compared with mock-injected controls at day 6 post-infection. Bar graphs show the mean ± s.e.m. (****P<0.0001; Mann-Whitney two-tailed test). Data are representative of 2 experiments with 7 mice per group.

Material and Methods

Mice. C57BL/6J (B6), C57BL/6-Gt(ROSA)26Sortm1(HBEGF)Awai/J (R26-LSL-DTR), B6.129P2(Cg)-Cx3cr1tm2.1(cre/ERT2)Litt/WganJ (Cx3cr1-creERT2), B6.129P2-Lyz2tm1(cre)Ifo/J (LysM-Cre), B6.Cg-Gt(ROSA)26Sortm14(CAG-tdTomato)Hze/J (R26- LSL-TdTomato), B6.129X1-Gt(ROSA)26Sortm1(EYFP)Cos/J (R26-LSL-YFP) and B6;129S-Stat1tm1Mam/Mmjax (Stat1$^{fl/fl}$), Tg(Csf1r-HBEGF) (Cs1fr-LSL-DTR) mice were purchased from The Jackson Laboratory (Bar Harbor, ME). K18-hACE2 transgenic mice that express human ACE2 kindly provided by Jackson laboratory. B6.SJL-*Ptprc*^{a}*Pepc*^{b}/BoyCr: Ly5.1 were purchased at Charles River. B6 D^{b}GP$_{33–41}$ TCR-tg (P14) were bred and maintained at the National Institutes of Health (NIH). Cd163-Cre and Timd4-Cre were kindly provided by Toby

Lawrence (CIML) and were generated by modifying embryonic stem cells on a C57BL/6 background. MAVS$^{-/-}$ femurs and tibias for bone marrow transplantation were provided by Marie-Cécile Michallet (Cancer Research Center Lyon, France). Cd163-Cre : R26-LSL-YFP, CD163-Cre : Csf1r-LSL-DTR, Cd163-Cre : Stat1$^{fl/fl}$, LysM-Cre : Stat1$^{fl/fl}$, LysM-Cre : Csf1r-LSL-DTR, Timd4-Cre : R26-LSL-DTR, Cx3cr1-creERT2: R26-LSL-DTR and littermate controls were obtained in the F1 and F2 generations by originally crossing the aforementioned homozygous mouse lines. Male and female mice in this study were used at 6–8 weeks of age unless otherwise specified. Unless specified, all mice were then bred and maintained under specific pathogen free conditions at Centre d'Immunologie de Marseille-Luminy (CIML), with water and food ad libitum and 12-h/12-h night/daylight cycle. All animal experiments were approved and performed in accordance with the limiting principles for using animal in testing (the three Rs: replacement, reduction, and refinement) and approved by the French Ministry of Higher Education and Research.

Baboons. Adult baboons were maintained at the local primate center (Rousset, France) which harvested and provided by the tissues.

LCMV Virus. To induce meningitis and subacute meningitis, adult mice at 6 to 8 weeks of age were infected intravenously (i.v.) with 1×10^7 plaque forming units (PFU) of LCMV Armstrong clone 53b. Survival following infection was monitored. Stocks were prepared by a single passage on BHK-21 cells, and viral titers were determined by plaque formation on Vero cells.

SARS-CoV2 Virus. K18-hACE2 mice (noted Tg-K18) were intranasally inoculated with 10^5 PFU (40 ul) of SARS-CoV-2 (strain BetaCoV/France/IDF0372/2020) or saline injection solution (PBS). Mice were harvested at 2, 3, 4, 5, 6 and 7 days post-infection. In addition, one control group of K18-hACE2 non-carrier animals ('WT') was intranasally inoculated with of SARS-CoV-2 and one control group of K18-hACe2 animals was injected with saline solution (PBS).

Meningeal whole-mount immunohistochemistry of mouse meninges. Mice were euthanized with overdose of ketamine-xylazine anesthetic and perfused with phosphate buffered saline (PBS) for subsequent antibody staining. Skull caps were removed, and following a brief wash in PBS, meninges were incubated at room temperature for 15 min in 1.5 ml of blocking solution containing mouse IgG (0.5 mg/ml, Jackson Research) and Fc Block CD16/32 (24G2 supernatant purified from tissue culture supernatant, 1/100). The meninges were subsequently stained with primary antibodies at room temperature for 1 h. The following primary antibodies were used: Brilliant Violet 421 anti- IA^b/IE^b (1.25 µg/ml; clone M5/114.15.2, BD), Alexa Fluor® 488 and Alexa Fluor® 647 anti-Ly6C (2.5 µg/ml; clone HK1.4; BioLegend),

Alexa Fluor® 488 and Alexa Fluor® 647 anti-CD206 (2.5 µg/ml; clone C068C2; BioLegend), PE anti-CD31 (clone 390; BioLegend). All antibodies were diluted in PBS + 2% fetal bovine serum (staining buffer). Meninges were then washed three times in staining buffer for 30 seconds and fixed overnight at 4°C in 5% formalin. The following day the meninges were carefully removed from the skull caps with fine-tipped forceps. The meninges were placed in mounting medium (FluorSave Reagent with or without DAPI; Vectashield) on a glass slide (Superfrost ® Plus; ThermoScientific), spread out and flattened with forceps, and cover-slipped. For uncoupled primary antibody staining, the meninges were incubated at 4°C overnight in formalin 5% (Sigma). The next day, the following primary antibodies were used: goat anti-mouse IBA1 (Novus Biologicals), rabbit anti-mouse IBA1-1 (Fujifilm-Wako), chicken anti-mouse NF-H (Abcam) in staining buffer with Triton at 0.5%, overnight at 4°C. The third day, the meninges were washed three times in staining buffer for 30s and stained with secondary antibodies. The following secondary antibodies were used: donkey anti-rabbit IgG Alexa Fluor® 647 (clone Poly4064, BioLegend), donkey anti-goat IgG Alexa Fluor® Plus 488 (Thermofischer). All secondary antibodies were diluted at 1:500 in staining buffer and secondary stainings were at room temperature for 2 hrs. For LCMV staining, meninges were briefly fixed in 5% formalin, 10min on ice, to facilitate LCMV detection. This was followed by intracellular staining overnight at 4°C of anti-LCMV (clone VL-4; BioXCell). Anti-LCMV mAb was directly conjugated to Alexa Fluor 647 using an antibody-labeling kit (Invitrogen) according to manufacturer's instructions. Alternatively, purified anti-LCMV (clone VL-4; BioXCell) was used overnight at 4°C, and followed by aforementioned washes and secondary stains.

Meningeal whole-mount immunohistochemistry of baboon meninges. Baboon meninges were fixed in 4% paraformaldehyde (Sigma) for 24h. The following primary antibodies were used for staining: chicken anti-human Iba1 (1.25 µg/ml, Synaptic Systems) and mouse IgG2a anti-human HLA-DR (1.25 µg/ml, L243; BL) for 48h at 4°C in FACS Buffer supplemented with 0.5% Titon-X100 (Sigma). After three 5-min washes in PBS, meninges were incubated for 24h at 4°C with secondary antibodies. Following three 5-min washes in PBS, meninges were incubated in clearing medium (Histodenz, Sigma) for 48 hours at °C. For EdU staining, 1 mg of EdU was injected 1 hour prior to sacrifice, and EdU was revealed following the manufacturer's instructions (Click-iT EdU, Thermofischer).

Pia mater immunohistochemistry. Brain samples were fixed in a solution of formalin 5% during 10 mins on ice and incubated in a staining solution containing PBS supplemented with 2% FBS and 0.5% Triton X-100 (Sigma) and staining was then performed as for meningeal whole mounts.

Brain immunohistochemistry. Brains and spleens were fixed in formalin 5% overnight at 4°C. The next day, samples were washed with PBS before dehydration in a solution of 30% sucrose (Sigma) overnight at 4°C. For inclusion, each brain and spleen were individually placed in clear base molds (37x24x5mm, Leica) and covered with OCT Embedding Medium (ThermoScientific) and frozen using isopenthane. Brain slices were cut with a cryostat at a thickness of 25µm and stained with antibodies in Triton-supplemented staining buffer as for meningeal wholemounts.

Imaging acquisition and analysis. Fluorescent images were acquired using an Zeiss LSM780 x 2 laser scanning confocal microscope (Carl Zeiss Microscopy) equipped with 405, 488, 561, and 635 laser lines, 4 side window PMTs for simultaneous 4 channel acquisition, and a 10× objective. 3D tile scans encompassing the entire meninges were collected (*z* depth = 400 µm, *z* step size = 20 µm for meninges, and 10 µm for brain sections) and analyzed using Imaris 8.1.2 software.

Histocytometry-*Cell quantification and phenotyping.* After collecting tile scans by confocal microscopy, entire meningeal whole mounts or specific anatomical regions within the meninges (e.g. lobe, suture) were analyzed by histocytometry. The Surface Creation Wizard in Imaris 8.1.2 software was used to threshold on and identify positively stained cells within the 3D meningeal tile scans. Once identified a value-based visual surface was generated for all positively stained cells, which enabled quantification of fluorescence intensity as well as the frequency of labeled and unlabeled cells. Channel statistics for MHC-II or dextran were obtained for 3D cellular surfaces defined based on CD206 or IBA1. These channel statistics were subsequently exported into Excel (Microsoft), and mean voxel fluorescence was plotted in FlowJo software by utilizing the Text to FCS conversion utility (TreeStar Inc). Percentages of surfaces either positive or negative for MHC-II or dextran were gated using traditional log-scale based flow cytometry plots in FlowJo and then graphed on linear *xy* plots to map their respective positions within the meninges.

Histocytometry-*Clustering* This approach was also used to quantify MHCII+ cells cluster quantities and total meningeal area, using adequate object size parameter.

Mononuclear cell isolation. Anesthetized mice received an intracardiac perfusion with PBS to remove contaminating erythrocytes. Leukocytes were isolated from the meninges using forceps to gently separate them from the underside of skull cap (the same method used to prepare meningeal whole mounts above). This was followed by enzymatic digestion in RPMI containing 2.5 mg/ml collagenase D (Roche) + 0.1 mg/ml DNase (Roche) for 30 min at 37 °C

with gentle shaking every 10 min. Leukocytes were also isolated from the brain and the spleen as described. Following digestion, supernatants were isolated, washed, and finally passed through a 35-µm pore cell strainer. After this step, meningeal cells were used for staining. Cells from the brain, however, were resuspended in 40% Percoll (GE Healthcare) gradient in PBS1X and centrifuged to remove myelin and debris from the preparation. Afterwards, brain leukocytes were stained comparably to meningeal cells. Spleen samples were similarly digested. After straining, spleen leukocytes were treated with RBC1X to eliminate red blood cells, then washed and 1:20 of total cells were isolated for cell staining.

Blood cell isolation. Blood samples were collected by retro-orbital bleeding using capillary tubes (Cat No 749321) and placed in 1mL PBS1X (Sarstedt). Red blood cells were lysed with RBC 1X lysis buffer (eBioscience) and samples were washed twice with PBS containing 2% FBS before antibody staining.

Flow cytometry. Surface staining was performed by incubating cell suspensions for 30 min on ice with cocktails of mAbs in PBS containing 2% FBS. Prior to staining, cell preparations were blocked with 5 µg/ml rat anti–mouse CD16/32 (Fc receptor block; BD) and 0.5 mg/ml whole mouse IgG (Jackson ImmunoResearch Laboratories, Inc.) for 10 min on ice to reduce unspecific antibody binding. Dead cells were excluded from the analysis by using the LiveDead fixable Blue Cell Staining kit (Invitrogen). The following antibodies were obtained from BioLegend (BL), BD, or eBioscience (eB): CD45.2 BUV737 (104, BL), CD11b Brilliant Violet 570 (M1/70, BL), CD90.2 (Thy1.2) BUV395 (30-H12, BD), Ly6G Brilliant Violet 711 (RA3–6B2, BL), CD206 AF488 (C068C2, BL), IA^b/IE^b Brilliant Violet 421 (M5/114.15.2, BL), H-$2D^b$ H-$2K^b$ PE (28–8-6, BL), Ly6C PE-CF594 (AL-21, BD), CD8a Alexa700 (SK1, BL), CD4 Brilliant Violet 786 (RM4.5, BD), NK1.1 APC (S17016D, BL) CD64 Brilliant Violet 605 (X54–5/7.1, BL), CD11c PE-Cyanine5.5 (N418, eB), CD45.1 Brilliant Violet 650 (A20, BL) and corresponding isotype controls. All antibodies were used at a concentration of 0.5µg/ml. Samples were acquired using BD FACSymphony™ A5 Cell Analyzer, and data were analyzed using FlowJo software version 10.5.3.

Sorting of MM. MM were isolated from PBS or LCMV-infected mice at day 1 and day 2 post-infection using a Melody Cell Sorter (BD) equipped with an integrated BSL-2 enclosure. Meningeal cells were extracted and stained as described in the Mononuclear cell isolation and Flow cytometry sections above. Two different cell populations (CD206+ MHC II+ MM, CD206+ MHC II- MM) were sorted to >95% purity.

Adoptive transfers. Mice were seeded i.v. with 10^5 OFP^+ P14 $CD8^+$ T cells in PBS purified from the splenocytes of naive transgenic mice using a CD8 negative selection kit (Stem Cell Technologies). The purity after enrichment was determined to be greater than 98%. One day later the mice were challenged i.v. with LCMV Armstrong.

Bone marrow (BM) chimeras. BM was harvested from femurs and tibias of $MAVS^{-/-}$, Ly5.1 and B6 mice and 10^7 BM cells were i.v. injected into recipient mice following a two irradiations dose (4 hours apart) of 1.1 Gy/min during 4 mins. Mice received antibiotics (Bactrim) in drinking water for 4 weeks following irradiation and were allowed 6 weeks to reconstitute their hematopoietic system.

***In vivo* cell depletions.** In order to deplete CD8+ T cells, mice were injected intravenously twice at day 3 and 5, post LCMV infection with 250 µg of CD8 depleting antibody (clone YTS 169.4, BioXcell), or the rat IgG2b control antibody (clone LTF-2, BioXcell). To block infiltration of immune cells, mice were injected intravenously at day 3 and 5 post-infection with 500 µg of anti-LFA-1 (clone M17/4, BioXcell) and 500 µg anti-VLA-4 (clone PS/2, BioXcell) or with the same amount of rat IgG2b and rat IgG2a control antibodies (clones LTF-2 and IA3, BioXcell).

PLX administration. Mice are anesthetized with isoflurane before being injected subcutaneously under the scalp with 200 µL of PLX or mock gel (control). The PLX gel is composed 2 mg of Pexidartinib (PLX3397, DC Chemicals, China) dissolved in 20 uL of dimethyl sulfoxide (Sigma Aldrich) and 180 µL of Corn oil (delivery vehicle for fat soluble, Sigma Aldrich). The mock gel is composed equally but does not contain Pexidartinib.

LPS and Dextran injections. Hundred µl of LPS (Sigma, 0.1 mg/ml) or Dextran-Rhodamine B isothiocyanate (10kDa; Sigma Aldrich, 10mg/ml) were injected intraveinously via the retro-orbital vein.

DT administration. 100µl is injected subcutaneously under the scalp of mice which contains 0.1µg of diphteria toxin (DT, Sigma) in carboxymethycellulose (12 mg/ml, Sigma). DT was injected on two consecutive days before infection or sacrifice.

Isolation of nucleated meningeal cells and scRNA-sequencing using 10X Genomics platform. Meningeal cells were extracted as described in the Mononuclear cell isolation and Flow cytometry sections above (apart from sacrifice, which was performed using an overdose of Ketamine/Xylasine) and stained with Hoescht 33342 (10µg/ml, Sigma) and Draq7 (0.3µM, ThermoFischer). The 4 samples were differentially labelled using 4 Hashtags (TotalSeq-A,

clone M1/42; 30-F11, Biolegend) at 0.1mg/ml for 15min at 4°C. After a wash, nucleated cells were isolated from 2 PBS or 2 LPS-injected mice (7 weeks-old males) at day 1 post-injection using a FACS Aria III SORP (BD) using a 100 µm nozzle. 52 000 cells of each sample were pooled, centrifuged at 350g for 3 minutes, and 35 000 cells of the pool were loaded on a GemCode Single Cell Instrument (10x Genomics) to generate single-cell gel beads-in-emulsion (GEM). GEM and scRNA-libraries were prepared using the GemCode Single Cell 3'v3 Gel Bead and Library Kit (10X Genomics, No. 120237) and the Chromium i7 Multiplex kit (10x Genomics, No 120262) according to the manufacturer's instructions. Briefly, GEM reverse-transcription incubation was performed in a 96-deep-well reaction module at 53 °C for 45 min, 85 °C for 5 min and ending at 4 °C. Next, GEMs were broken and complememtary DNA (cDNA) was cleaned up with DynaBeads MyOne Silane Beads (Thermo Fisher Scientific, No. 37002D) and SPRIselect Reagent Kit (Beckman Coulter, No. B23318). Fulllength, barcoded cDNA was PCR amplified with a 96-deep-well reaction module at 98 °C for 3 min, 11 cycles at 98 °C for 15 s, 63 °C for 20 s and 72 °C for 1 min, one cycle at 72 °C for 1 min and ending at 4 °C. Following cleaning up with the SPRIselect Reagent Kit and enzymatic fragmentation, library construction to generate Illumina-ready sequencing libraries was performed by the addition of R1 (read 1 primer), P5, P7, i7 sample index and R2 (read 2 primer) via endrepair, A-tailing, adapter ligation, post-ligation SPRIselect cleanup/size selection and sample index PCR. After generation of the gene expression and HTO libraries, the cDNA content of post-sample index PCR samples was analyzed using the 2100 BioAnalyzer (Agilent) and the samples were sequenced by the TGML platform (TAGC, Marseille). Sequencing libraries (molar ratio 92/8 for gene expression/HTO) were loaded on a NextSeq500 Illumina flow cell High output (75 cycles) with sequencing settings following the recommendations of 10x Genomics (read 1:28 cycles; read 2: 55 cycles; index i7: 8 cycles; index i5: no cycles; 1.8 pM loading concentration).

scRNA-seq analysis. Preprocessing and analysis of data were done through the usage of standard tools and custom R and bash scripts. We notably used R version 4.0.3, Seurat package version 3.2.2 (Stuart et al., 2019), 10x Genomics CellRanger version 4, CITE-seq-count version 1.4.3 (Stoeckius et al., 2018). Docker and Singularity containers were used to ensure the reproducibility of analyses. All codes and data are available on Github and Zenodo.

Pre-processing of 10x 3' datasets. Raw fastq files from gene expression libraries were processed using Cell Ranger software, with alignment on the mm10 reference genome. For each experiment, cells with less than 200 genes detected and genes detected in less than 3 cells were removed. We further excluded bad quality cells expressing less than 1,000 UMI, more than 20% mitochondrial genes or less than 3% ribosomal genes. HTO barcodes for

sample demultiplexing after hashing were counted using CITE-seq-count and were normalized for each cell using a centered log ratio (CLR) transformation across cells implemented in the Seurat function NormalizeData. Cells were demultiplexed using Seurat MULTIseqDemux function and barcodes assigned as doublets or negative were excluded from further analysis. The resulting filtered UMI count matrices were log-normalized with Seurat NormalizeData with a scale factor of 10,000.

10x Dataset analysis. Analysis of datasets were performed using custom R scripts. Variable genes (n=2000) were identified with Seurat FindVariableFeatures (vst method). After centering with Seurat ScaleData, principal component analysis was performed on variable genes with Seurat RunPCA, and embedded in two-dimensional UMAP plots with Seurat RunUMAP on 50 principal components. UMAP embeddings colored by sample metadata or clusters were generated by Seurat DimPlot, those colored by single gene expression or module scores were generated by Seurat FeaturePlot or with ggplot2 ggplot. Clustering was performed using the FindNeighbors and FindClusters methods of the Seurat package using 30 PC for SNN graph build and Leiden clustering method with a sensitivity set to 2.0 within the global data and with a sensitivity set to 0.3 within the MM subset. Subsetting was performed using *subset* function of the Seurat package using the identities of relevant clusters. Marker genes between clusters were identified using the FindAllMarkers method of the Seurat package using the Wilcoxon Rank Sum test on genes expressed at least in 10% of the cells, a logFC threshold of 0.25 and a FDR threshold of 0.001. Heatmap of gene expression along tissue clusters was done performing a mean of the expression of the genes of interest over the clusters, using the heatmap package (version 1.0.12) for the plot. Heatmap of Szymkiewicz–Simpson coefficient were computed using the set of identified marker genes of each cluster and the ggplot2 ggplot function (version 3.3) for the plot. For the 'thresholding method', cells expressing CD206 were selected, and the expression score of MHC-II was obtained with *AddModuleScore* function of the Seurat package based on the expression score of H2-Ab1, Cd74, H2-Eb1 and H2-Aa. The selection of cells depending on the expression score was set with a threshold of 0. Gene Ontology pathways were obtained with clusterProfiler v4.0.0 R package and volcano plots were obtained with EnhancedVolcano v.1.9.13 R package.

Quantitative PCR. Meningeal, brain and spleen tissues or FACS-sorted cells were collected in TRIzol (Invitrogen), and total RNA was extracted using RNeasy Mini Kit (Qiagen) per the manufacturer's instructions. Purified RNA was reverse transcribed into cDNA by using an iScript cDNA Synthesis kit (Life Technologies). Real-time PCR was performed using SYBR® Premix Ex Taq™ (Takara) reactions and cDNA template or water (non-template negative control) with the Applied Biosystems 7500 Real-Time PCR System. Reactions were conducted

in duplicates, and PCR products were subjected to melt analysis to confirm purity after DNA amplification. For each gene, expression values were normalized to a *Actb* housekeeping genes. The resulting relative gene expression was then expressed relative to the housekeeping gene or as a fold-change from indicated control samples. Primers were designed and obtained from Integrated DNA Technologies (IDT), and sequences are provided in the Supplementary Table.

Statistical analysis. Statistical analyses for data for experiments containing two groups were performed using a Student's *t* test (parametric datasets) or a Mann-Whitney rank sum test (non-parametric datasets). Experiments involving more than two groups were analyzed by ANOVA followed by a Student-Newman-Keuls test or a Holm-Sidak test for pairwise comparisons. All statistical analyses were performed in Graphpad Prism 6.0 and were considered statistically different at a *P* value of <0.05. All data are displayed as the mean ± SEM.

Data availability.

The datasets and primary data that support the findings of this study are available from the corresponding author upon request.

Acknowledgements

We thank Lionel Chasson (Histology Platform, Centre d'Immunologie Marseille-Luminy) for assistance with histology and Pierre Golstein (Centre d'Immunologie Marseille-Luminy) for critical advice. These studies were supported by the Marie-Curie, European Research Council and AMIDEX (Aix-Marseille University) grants and by institutional funding from the Institut National de la Santé et de la Recherche Médicale, Centre National de la Recherche Scientifique, and Aix-Marseille-Université. Microscopy facilities are supported by L'Agence Nationale de la Recherche (grant ANR-10-INBS-04-01 France Bio Imaging). High throughput sequencing was performed at the TGML Platform, supported by grants from Inserm, GIS IBiSA, Aix-Marseille Université, and ANR-10-INBS-0009-10." The authors declare no competing financial interests.

Author contributions: JR and RR designed the experiments. JR, EES and RR performed the experiments with help from EG and ARQ. AZ and BM performed SAS-CoV2 infections. MT and LS performed the bioinformatics analyses. MCM provided MAVS-/- mice. DM provided critical advice as well as LCMV virus and P14 mice. JR and RR wrote the manuscript.

Supplementary material

Table 1 provides the list of primers used in this study.

Supplementary legends

Supplementary Figure 1.

A. Maximal intensity projections of meningeal whole mounts of B6 mice, showing the presence of MM stained with CD206 (green) in the dura mater of the spinal cord. Scale bar: 1 mm. Data is representative of 2 independent experiments, with 5 mice.

B, C. (B) Maximal intensity projections of meningeal whole mounts of B6 mice, showing the presence of MM (CD206), blood vessels (CD31) and nerve fibers (NF-H) in the dura mater of the brain. Scale bar: 1 mm. (C) Magnified view of the lobe area. Scale bar: 30 µm. Data is representative of 2 independent experiments, with 5 mice.

D. Quantification of the density of MM based on CD206 staining, showing a higher density of MM in the brain meninges compared to spinal ventral ('Ventral Sp.") and dorsal ("Dorsal Sp.") meninges. Bar graphs show mean ± s.e.m and asterisks denote statistical significance (NS=Not Significant, *P<0.05, ***P<0.001; Kruskal-Wallis test followed by Dunn's multiple comparison test). Data are representative of 2 independent experiments, with 4 mice (Spinal meninges) and 8 mice (Brain meninges) per group, and 2 regions (Spinal meninges) and 4 regions (Brain meninges) quantified per mouse.

E. Quantification of the density of MM based on CD206 staining showing a constant density over time. Bar graphs show mean ± s.e.m and asterisks denote statistical significance (NS=Not Significant; Kruskal-Wallis test). Data are representative of 2 independent experiments, with 5 mice per group, and 2 regions quantified per mouse.

F. Quantification of the density of MM based on IBA1 staining showing the density of MM in the baboon meninges. Bar graphs show mean ± s.e.m. for the indicated groups. Data are representative of 4 independent baboons, with 3 regions quantified per baboon.

Supplementary Figure 2.

A. Gating strategy for neutrophils (gated on LiveDead- CD45+ CD11b+ Thy1.2- Ly6C- Ly6G+ cells), monocytes (gated on LiveDead- CD45+ CD11b+ Thy1.2- Ly6C+ Ly6G-, with MHC-II+ and MHC-II- subsets), MM (gated on LiveDead- CD45+ CD11b+ Thy1.2- Ly6C- Ly6G- CD11c- CD64+, with CD206 and MHC-II subsets), CD11b+ DC (gated on LiveDead- CD45+ CD11b+ Thy1.2- Ly6C- Ly6G- CD11c+ MHC-II+ cells), CD11b- DC (gated on LiveDead- CD45+ Thy1.2- CD11b- CD11c+ MHC-II+ cells), CD8+ T cells (gated on LiveDead- CD45+ CD11b- Thy1.2+ CD8+ cells), CD4+ T cells (gated on LiveDead- CD45+ CD11b- Thy1.2+ CD4+ cells), NK cells (gated on LiveDead- CD45+ NK1+ Thy1.2-), NKT cells (gated on LiveDead- CD45+ CD11b- Thy1.2+ NK1+ cells), other T cells (gated on LiveDead- CD45+ CD11b- Thy1.2+ CD4- CD8- NK1-) and CD45neg cells (gated on LiveDead- CD45-).

B, C. CX3CR1-CreERT2: R26-LSL-TdTom mice were pulsed at 6 weeks old with tamoxifen. Only resident cells with slow turn-over remained TdTomato+, whereas blood myeloid populations became TdTomato-. Myeloid cells from the meninges, brain, and blood were analyzed 2 months later by flow cytometry for TdTomato expression. (B) A majority of blood monocytes (gated on LiveDead- CD45+ CD11b+ Thy1.2- Ly6G- CD115+ cells) were TdTom- and brain microglia (gated on LiveDead- CD45+ CD11b+ Thy1.2- Ly6C- Ly6G- CD206- cells) were TdTom+, while MM (gated on LiveDead- CD45+ CD11b+ Thy1.2- Ly6C- Ly6G- CD206+ cells) were divided into two populations of TdTom+ and TdTom- cells. (C) Subdivision of MM into CD206+ MHC-II+ and CD206+ MHC-II- subsets shows that the majority of blood-derived cells were differentiating into CD206+ MHC-II+ MM, leading to an accumulation of CD206+ MHC-II+ cells especially in the Td-Tom- compartment. Bar graphs show mean ± s.e.m. for the indicated groups, and asterisks denote statistical significance (*P<0.05; unpaired two-tailed Student's *t*-test). Data are representative of 2 experiments, with 5 mice per group.

Supplementary Figure 3.

Gene Ontology pathways of DEGs in LPS condition compared to PBS condition in MHC-II+ MM obtained with clusterProfiler R package (top 100 pathways). MHC-II+ MM were defined based on the 'clustering' method (for details, see Material and Methods).

Supplementary Figure 4.

Gene Ontology pathways of DEGs in LPS condition compared to PBS condition in MHC-II- MM obtained with clusterProfiler R package (top 100 pathways). MHC-II- MM were defined based on the 'clustering' method (for details, see Material and Methods).

Supplementary Figure 5.

A. UMAP representation of nucleated meningeal cells (7,035 cells). MM are indicated by the red box. Single-cell RNA sequencing was performed on 4 meningeal samples (from 2 mice injected with PBS and 2 with LPS) using 10X genomics and data was analyzed using Seurat software in combination with public datasets (brainimmuneatlas.org). Clustering was done with 50 dimensionalities of PCA, 30 PC and a resolution of Louvain's algorithm of 2 and the 29 clusters were regrouped into 16 cell clusters to facilitate visualization, based on similarity of their marker genes.

B. UMAP representation of macrophage subsets using CD206 and MHC-II threshold identification. MM CD206+ are selected with a score of CD206 (Mrc1) > 0. Expression score of MHC-II was obtained with AddModuleScore function of the Seurat package based on the expression score of H2-Ab1, Cd74, H2-Eb1 and H2-Aa giving an average score of these four MHC-II related genes. The selection of cells depending on the expression score was set with

a threshold of 0 with subset function of the Seurat package. MHC-II+ MM with a score of MHC-II > 0 and MHC-II- MM with a score of MHC-II <= 0.

C. Venn diagram of DEGs (adjusted p-value <0.05, abs(log2FC)>0.25) in LPS condition ('Activated') compared to PBS condition, in MHC-II+ and MHC-II- MM.

D. Volcano plot of genes expressed in LPS versus PBS condition in MM obtained with EnhancedVolcano R package.

- Volcano plot of genes expressed in LPS versus PBS condition in MHC-II+ MM obtained with EnhancedVolcano R package.
- Volcano plot of genes expressed in LPS versus PBS condition in MHC-II- MM obtained with EnhancedVolcano R package.

E. Gene Ontology pathways of DEGs expressed in LPS versus PBS condition in MM, obtained with clusterProfiler R package.

- Gene Ontology pathways of DEGs expressed in LPS versus PBS condition in MHC-II+ MM, obtained with clusterProfiler R package.
- Gene Ontology pathways of DEGs upregulated in LPS versus PBS condition in MHC-II- MM, obtained with clusterProfiler R package.

Supplementary Figure 6.

Gene Ontology pathways of DEGs in LPS condition compared to PBS condition in MHC-II+ MM obtained with clusterProfiler R package (top 100 pathways). MHC-II+ MM were defined based on the 'thresholding' method (for details, see Material and Methods).

Supplementary Figure 7.

Gene Ontology pathways of DEGs in LPS condition compared to PBS condition in MHC-II- MM obtained with clusterProfiler R package (top 100 pathways). MHC-II- MM were defined based on the 'thresholding' method (for details, see Material and Methods).

Supplementary Figure 8.

A. LCMV mRNA levels were quantified by quantitative PCR (Q-PCR) in the spleens of Cd163-Cre : Csf1r-LSL-DTR mice and controls treated with DT, at day 6 post-infection. LCMV mRNA levels were significantly higher in Cd163-Cre : Csf1r-LSL-DTR mice. Bar graphs show the mean ± s.e.m. and asterisks denote statistical significance (****P<0.0001; Mann-Whitney two-tailed test). Data are representative of 2 independent experiments with 4 (Control) and (Cd163-Cre : $Stat1^{fl/fl}$) mice per group.

Supplementary Figure 9.

A,B. LysM-Cre : Stat1$^{fl/fl}$ mice and littermate controls were injected intravenously with 1x10^6 PFU of wild type (WT) LCMV Armstrong. (A) Survival was monitored and showed no statistical differences between groups (NS=Not Significant; Kaplan Meier Survival Analysis). (B) Weight was measured in LysM-Cre : Stat1$^{fl/fl}$ mice and littermate controls following infection, showing a loss of weight in LysM-Cre : Stat1$^{fl/fl}$ mice peaking at day 8 post-infection. Graphs show the mean ± s.e.m. and asterisks denote statistical significance (NS=Not Significant, *P<0.05, **P<0.01, ****P<0.0001; One-way ANOVA followed by Holm-Sidak pairwise comparison test). Data are representative of 2 independent experiments with 6 mice (Control) and 14 mice (LysM-Cre : Stat1$^{fl/fl}$) per group.

C,D. Cd163-Cre : Stat1$^{fl/fl}$ mice and littermate controls were injected with 1x10^6 PFU of wild type (WT) LCMV Armstrong. (C) Weight was measured in Cd163-Cre : Stat1$^{fl/fl}$ mice and littermate controls following infection, showing a loss of weight in Cd163-Cre : Stat1$^{fl/fl}$ mice peaking at day 6 post-infection. Graphs show the mean ± s.e.m. and asterisks denote statistical significance (NS=Not Significant, Kruskall Wallis test followed by Mann-Whitney two-tailed test with Holm-Sidak correction for multiple analysis). (D) Survival was monitored and showed no statistical differences between groups (NS=Not Significant; Kaplan Meier Survival Analysis). Data are representative of 2 independent experiments with 3 mice (Control) and 7 mice (Cd163-Cre : Stat1$^{fl/fl}$) per group.

E. Cd163-Cre : Stat1$^{fl/fl}$ mice and littermate controls were infected with LCMV and treated with Rat IgG2b and Rat IgG2a (0.5mg) isotype antibodies at day 3 and day 5 post-infection. Six days later, neutrophils (gated on LiveDead- CD45+ CD11b+ Thy1.2- Ly6C- Ly6G+ cells), monocytes (gated on LiveDead- CD45+ CD11b+ Thy1.2- Ly6C+ Ly6G-, with MHC-II+ and MHC-II- subsets), MM (gated on LiveDead- CD45+ CD11b+ Thy1.2- Ly6C- Ly6G- CD11c- CD64+, with CD206 and MHC-II subsets), CD11b+ DC (gated on LiveDead- CD45+ CD11b+ Thy1.2- Ly6C- Ly6G- CD11c+ MHC-II+ cells), CD11b- DC (gated on LiveDead- CD45+ Thy1.2- CD11b- CD11c+ MHC-II+ cells), CD8+ T cells (gated on LiveDead- CD45+ CD11b- Thy1.2+ CD8+ cells), CD4+ T cells (gated on LiveDead- CD45+ CD11b- Thy1.2+ CD4+ cells), NKT cells (gated on LiveDead- CD45+ CD11b- Thy1.2+ NK1+ cells) in the meninges were analyzed by flow cytometry. As in infected mice (not treated with isotype), infection triggers an inflammatory reaction with a trends towards an increase in monocytes and CD8+ T cells in Cd163-Cre : Stat1$^{fl/fl}$ mice compared to controls. Bar graphs show the mean ± s.e.m. for the indicated groups, and asterisks denote statistical significance (NS=Not Significant, Kruskall Wallis test followed by Mann-Whitney two-tailed test with Holm-Sidak correction for multiple analysis). Data are representative of 2 independent experiments with 6 (Control) and 5 (Cd163-Cre : Stat1$^{fl/fl}$) mice per group.

F. LCMV mRNA levels were quantified by quantitative PCR (Q-PCR) in the brains Cd163-Cre : Stat1$^{fl/fl}$ mice injected with isotype antibodies control, at day 6 post-infection. LCMV mRNA

levels were significantly higher in Cd163-Cre : Stat1$^{fl/fl}$ than in mock-injected mice. Bar graphs show the mean ± s.e.m. and asterisks denote statistical significance (***P<0.001; Mann-Whitney two-tailed test). Data are representative of 2 independent experiments with 6 (Control) and 4 (Cd163-Cre : Stat1$^{fl/fl}$) mice per group.

G. B6 mice were reconstituted with WT or MAVS$^{-/-}$ bone marrow and infected with LCMV. An additional group of MAVS$^{-/-}$ BM reconstituted mice was injected with PBS instead as control. Six days later, neutrophils (gated on LiveDead- CD45+ CD11b+ Thy1.2- Ly6C- Ly6G+ cells), monocytes (gated on LiveDead- CD45+ CD11b+ Thy1.2- Ly6C+ Ly6G-, with MHC-II+ and MHC-II- subsets), MM (gated on LiveDead- CD45+ CD11b+ Thy1.2- Ly6C- Ly6G- CD11c- CD64+, with CD206 and MHC-II subsets), CD11b+ DC (gated on LiveDead- CD45+ CD11b+ Thy1.2- Ly6C- Ly6G- CD11c+ MHC-II+ cells), CD11b- DC (gated on LiveDead- CD45+ Thy1.2- CD11b- CD11c+ MHC-II+ cells), CD8+ T cells (gated on LiveDead- CD45+ CD11b- Thy1.2+ CD8+ cells), CD4+ T cells (gated on LiveDead- CD45+ CD11b- Thy1.2+ CD4+ cells), NKT cells (gated on LiveDead- CD45+ CD11b- Thy1.2+ NK1+ cells) in the meninges were analyzed by flow cytometry. Bar graphs show the mean ± s.e.m. for the indicated groups, and asterisks denote statistical significance (NS=Not Significant; Kruskall Wallis test followed by Mann-Whitney two-tailed test with Holm-Sidak correction for multiple analysis). For simplification, only the statistics comparing infected WT and MAVS$^{-/-}$ chimeras are indicated, sas the other comparisons showed no statistical difference. Data are representative of 2 independent experiments with 3 mice (PBS), 6 mice (BM WT) and 6 mice (BM MAVS$^{-/-}$) per group.

H. LCMV mRNA levels were quantified by quantitative PCR (Q-PCR) in the brains of WT or MAVS$^{-/-}$ bone marrow reconstituted mice, at day 6 post-infection. LCMV mRNA levels in MAVS$^{-/-}$ reconstituted mice were significantly higher than in WT-reconstituted mice. Bar graphs show the mean ± s.e.m. and asterisks denote statistical significance (*P<0.05, ****P<0.0001; Kruskal-Wallis test followed by Dunn's multiple comparison test). Data are representative of 2 independent experiments with 3 mice (PBS), 8 mice (BM WT) and 6 mice (BM MAVS$^{-/-}$) per group.

I. B6 mice were reconstituted with WT or MAVS$^{-/-}$ bone marrow, infected with LCMV and treated with CD8-depleting antibodies at day 3 and 5 post-infection. Six days post-infection, neutrophils (gated on LiveDead- CD45+ CD11b+ Thy1.2- Ly6C- Ly6G+ cells), monocytes (gated on LiveDead- CD45+ CD11b+ Thy1.2- Ly6C+ Ly6G-, with MHC-II+ and MHC-II- subsets), MM (gated on LiveDead- CD45+ CD11b+ Thy1.2- Ly6C- Ly6G- CD11c- CD64+, with CD206 and MHC-II subsets), CD11b+ DC (gated on LiveDead- CD45+ CD11b+ Thy1.2- Ly6C- Ly6G- CD11c+ MHC-II+ cells), CD11b- DC (gated on LiveDead- CD45+ Thy1.2- CD11b- CD11c+ MHC-II+ cells), CD8+ T cells (gated on LiveDead- CD45+ CD11b- Thy1.2+ CD8+ cells), CD4+ T cells (gated on LiveDead- CD45+ CD11b- Thy1.2+ CD4+ cells), NKT cells (gated on LiveDead- CD45+ CD11b- Thy1.2+ NK1+ cells) in the meninges were analyzed by

flow cytometry. No statistical difference was noted between groups. Bar graphs show the mean ± s.e.m. and asterisks denote statistical significance (NS=Not Significant; Kruskall Wallis test followed by Mann-Whitney two-tailed test with Holm-Sidak correction for multiple analysis). Data are representative of 2 independent experiments with 9 mice (BM WT) and 10 mice (BM MAVS$^{-/-}$) per group.

J. LCMV mRNA levels were quantified by quantitative PCR (Q-PCR) in the brains (left) and spleens (right) of CD8-depleted, WT or MAVS$^{-/-}$ bone marrow reconstituted mice, at day 6 post-infection. LCMV viral load was more elevated in the spleen but not the brain of MAVS$^{-/-}$ bone marrow reconstituted mice compared to controls. Bar graphs show the mean ± s.e.m. and asterisks denote statistical significance (NS=Not Significant, ****P<0.0001; Mann-Whitney two-tailed test). Data are representative of 2 independent experiments with 9 mice (BM WT) and 10 mice (BM MAVS$^{-/-}$) per group.

Supplementary Figure 10.

A,B. Mice were subjected to an injection of lipopolysaccharide (LPS) or of saline solution (PBS) before infection with LCMV. Meninges were analyzed by flow cytometry before (A) and after (B) injection with LCMV. Neutrophils (gated on LiveDead- CD45+ CD11b+ Thy1.2- Ly6C- Ly6G+ cells), monocytes (gated on LiveDead- CD45+ CD11b+ Thy1.2- Ly6C+ Ly6G-, with MHC-II+ and MHC-II- subsets), MM (gated on LiveDead- CD45+ CD11b+ Thy1.2- Ly6C- Ly6G- CD11c- CD64+, with CD206 and MHC-II subsets), CD11b+ DC (gated on LiveDead- CD45+ CD11b+ Thy1.2- Ly6C- Ly6G- CD11c+ MHC-II+ cells), CD11b- DC (gated on LiveDead- CD45+ Thy1.2- CD11b- CD11c+ MHC-II+ cells), CD8+ T cells (gated on LiveDead- CD45+ CD11b- Thy1.2+ CD8+ cells), CD4+ T cells (gated on LiveDead- CD45+ CD11b- Thy1.2+ CD4+ cells), NKT cells (gated on LiveDead- CD45+ CD11b- Thy1.2+ NK1+ cells) were enumerated. LPS induced a trend towards a reduction of CD11b+ DC as well as an increase in MHCII- monocytes before infection, while inflammatory cells (monocytes, CD8+ T cells) showed a non-significant trend towards increased cell number after infection in LPS pre-treated mice compared to controls. Bar graphs show the mean ± s.e.m. for the indicated groups, and asterisks denote statistical significance (NS=Not Significant, Kruskall Wallis test followed by Mann-Whitney two-tailed test with Holm-Sidak correction for multiple analysis). Data are representative of 3 independent experiments with 7 mice (PBS) and 6 mice (LPS) per group (A) and 6 mice (PBS+LCMV) and 7 mice (LPS+LCMV) per group (B).

C. Four months old and 1 month old mice were injected with LCMV. Meninges were analyzed by flow cytometry 6 days later. Neutrophils (gated on LiveDead- CD45+ CD11b+ Thy1.2- Ly6C- Ly6G+ cells), monocytes (gated on LiveDead- CD45+ CD11b+ Thy1.2- Ly6C+ Ly6G-, with MHC-II+ and MHC-II- subsets), MM (gated on LiveDead- CD45+ CD11b+ Thy1.2- Ly6C- Ly6G- CD11c- CD64+, with CD206 and MHC-II subsets), CD11b+ DC (gated on LiveDead-

CD45+ CD11b+ Thy1.2- Ly6C- Ly6G- CD11c+ MHC-II+ cells), CD11b- DC (gated on LiveDead- CD45+ Thy1.2- CD11b- CD11c+ MHC-II+ cells), CD8+ T cells (gated on LiveDead- CD45+ CD11b- Thy1.2+ CD8+ cells), CD4+ T cells (gated on LiveDead- CD45+ CD11b- Thy1.2+ CD4+ cells) were enumerated. LCMV induced a strong inflammation, especially in young mice (1MO). Bar graphs show the mean ± s.e.m. for the indicated groups, and asterisks denote statistical significance (NS=Not Significant, *P<0.05, **P<0.01, ***P<0.001; Kruskall Wallis test followed by Mann-Whitney two-tailed test with Holm-Sidak correction for multiple analysis). Data are representative of 3 independent experiments with 11 mice per group.

D, E. Mice were preferentially depleted of MHC-II+ MM before LCMV infection. (D) Timd4-Cre : R26-LSL-hDTR mice and littermate controls were injected transcranially with 100ng of diphteria toxin (DT) on two consecutive days. Neutrophils (gated on LiveDead- CD45+ CD11b+ Thy1.2- Ly6C- Ly6G+ cells), monocytes (gated on LiveDead- CD45+ CD11b+ Thy1.2- Ly6C+ Ly6G-, with MHC-II+ and MHC-II- subsets), MM (gated on LiveDead- CD45+ CD11b+ Thy1.2- Ly6C- Ly6G- CD11c- CD64+, and subdivided using CD206 and MHC-II), CD11b+ DC (gated on LiveDead- CD45+ CD11b+ Thy1.2- Ly6C- Ly6G- CD11c+ MHC-II+ cells), CD11b- DC (gated on LiveDead- CD45+ Thy1.2- CD11b- CD11c+ MHC-II+ cells), CD8+ T cells (gated on LiveDead- CD45+ CD11b- Thy1.2+ CD8+ cells), CD4+ T cells (gated on LiveDead- CD45+ CD11b- Thy1.2+ CD4+ cells), NK cells (gated on LiveDead- CD45+ NK1+ Thy1.2-), NKT cells (gated on LiveDead- CD45+ CD11b- Thy1.2+ NK1+ cells) were analyzed by flow cytometry, revealing no major differences. Bar graphs show mean ± s.e.m and asterisks denote statistical significance (NS=Not Significant, Kruskall Wallis test followed by Mann-Whitney two-tailed test with Holm-Sidak correction for multiple analysis). Data are representative of one experiment with 5 mice per group. (E) One day after DT treatment, LCMV was injected intravenously, and a similar flow cytometric analysis was performed at day 6 post-infection, revealing a trends towards an increase in the number of infiltrating of CD8+ T cells. Bar graphs show mean ± s.e.m and asterisks denote statistical significance (NS=Not Significant, Kruskall Wallis test followed by Mann-Whitney two-tailed test with Holm-Sidak correction for multiple analysis). Data are representative of one experiment with 5 mice per group.

F. At day 6 post-infection, LCMV mRNA was assessed by Q-PCR in spleens of Timd4-Cre : R26-LSL-hDTR mice and compared with littermate controls. Bar graphs show the mean ± s.e.m. (***P<0.001, Mann-Whitney two-tailed test). Data are representative of one experiment with 5 mice (Control) and 4 mice (Timd4-Cre : R26-LSL-hDTR) per group.

Supplementary Figure 11.

A. Mice were subjected to ‘meningeal rejuvenation’ before infection with LCMV. LysM-Cre : Csf1r-LSL-DTR mice and littermate controls were injected with 100ng of diphteria toxin (DT) transcranially at days 0 and 1 to deplete myeloid cells and then injected i.v. with blocking

antibodies (anti-LFA-1 & anti-VLA-4) at day 2 and day 4 to promote local CD206+ MHC-II- cells proliferation over CD206+ MHC-II+ cells infiltration. The kinetics of macrophage recovery was analyzed in the CD206+ MHC-II+ and the MHC-II- macrophage compartments, at day 1, 4 and 8 post initial DT injection, in 4 different meningeal regions (frontal, occipital, parietal and suture). Bar graphs show the mean ± s.e.m. and asterisks denote statistical significance (NS=Not Significant, *P<0.05, **P<0.01, ***P<0.001; Kruskall Wallis test followed by Mann-Whitney two-tailed test with Holm-Sidak correction for multiple analysis). Data are representative of 2 independent experiments with 3 mice (Control+DT) and 6 mice (LysM-Cre : Csf1r-LSL-DTR+DT) mice per group and 2 to 3 regions were quantified per mouse.

B. Maximal projections of meningeal whole mounts of LysM-Cre : Csf1r-LSL-DTR and control mice after administration of DT and anti-LFA/VLA at day 8 post-infection, showing the intense repopulation by CD206+ MHC-II- MM (green) compared to CD206+ MHC-II+ MM (yellow). The first row shows the whole meninges of control mice and rejuvenated mice at day 1, 4 and 8 post-rejuvenation. The 2nd and 3rd rows show magnification of the red insets (R1, R3). Scale bar: 1 mm (whole meninges) and 100 µm (insets). Data are representative of 2 independent experiments with 3 mice (Control+DT) and 4 mice (LysM-Cre : Csf1r-LSL-DTR+DT) mice per group.

C, D. Maximal projections (C) and quantification (D) of meningeal whole mounts of 'Rejuvenated' and control mice showing proliferating cells (Edu+, green) among MM (red) at day 4 and day 8 post-treatment. Four different meningeal regions (frontal, occipital, parietal and suture) were analyzed. Scale bar: 50 µm. Bar graphs show the mean ± s.e.m. and asterisks denote statistical significance (NS=Not Significant, *P<0.05, **P<0.01; Kruskall Wallis test followed by Mann-Whitney two-tailed test with Holm-Sidak correction for multiple analysis). Data are representative of 2 independent experiments with 3 mice (Control+DT) and 4 mice (LysM-Cre : Csf1r-LSL-DTR+DT) mice per group and 1 to 3 regions were quantified per mouse.

Supplementary Figure 12.

A, B. Mice were subjected to 'meningeal rejuvenation' before infection with LCMV. (A) LysM-Cre : Csf1r-LSL-DTR mice and littermate controls were injected with 100ng of diphteria toxin (DT) transcranially at days 0 and 1 to deplete myeloid cells and then injected i.v. with blocking antibodies (anti-LFA-1 & anti-VLA-4) at day 2 and day 4 to promote local MHC-II- cells proliferation over MHC-II+ cells infiltration. Neutrophils (gated on LiveDead- CD45+ CD11b+ Thy1.2- Ly6C- Ly6G+ cells), monocytes (gated on LiveDead- CD45+ CD11b+ Thy1.2- Ly6C+ Ly6G-, with MHC-II+ and MHC-II- subsets), MM (gated on LiveDead- CD45+ CD11b+ Thy1.2- Ly6C- Ly6G- CD11c- CD64+, and subdivided using CD206 and MHC-II), CD11b+ DC (gated on LiveDead- CD45+ CD11b+ Thy1.2- Ly6C- Ly6G- CD11c+ MHC-II+ cells), CD11b- DC

(gated on LiveDead- CD45+ Thy1.2- CD11b- CD11c+ MHC-II+ cells), CD8+ T cells (gated on LiveDead- CD45+ CD11b- Thy1.2+ CD8+ cells), CD4+ T cells (gated on LiveDead- CD45+ CD11b- Thy1.2+ CD4+ cells), NK cells (gated on LiveDead- CD45+ NK1+ Thy1.2-), NKT cells (gated on LiveDead- CD45+ CD11b- Thy1.2+ NK1+ cells) were analyzed by flow cytometry, revealing no statistical difference in those populations between 'rejuvenated' mice compared to controls. Bar graphs show mean ± s.e.m and asterisks denote statistical significance (NS=Not Significant; Kruskall Wallis test followed by Mann-Whitney two-tailed test with Holm-Sidak correction for multiple analysis). Data are representative of 2 independent experiments with 5 mice per group. (B) At day 8 post first DT injection, mice were infected with LCMV. Six days later, immune populations were assessed by flow cytometry, showing a trend towards a reduction in the number of macrophage populations. Bar graphs show mean ± s.e.m and asterisks denote statistical significance (NS=Not Significant, Kruskall Wallis test followed by Mann-Whitney two-tailed test with Holm-Sidak correction for multiple analysis). Data are representative of 2 independent experiments with 8 mice (Control) and 5 mice (LysM-Cre : Csf1r-LSL-DTR) per group.

C. LCMV mRNA levels were quantified by quantitative PCR (Q-PCR) in the spleens of 'rejuvenated' mice and compared with mock-injected controls. Bar graphs show the mean ± s.e.m. (****P<0.0001; Mann-Whitney two-tailed test). Data are representative of 2 independent experiments with 8 mice (Control) and 7 (LysM-Cre : Csf1r-LSL-DTR) mice per group.

Supplementary Figure 13.

MHC-II+ and MHC-II- MM (gated on CD45+ CD11b+ CD64+ CD206+) were sorted at 24h and 48h post-LCMV infection *in vivo*, and LCMV was quantified by RT-qPCR in each sample. LCMV was readily detected in MHC-II+ MM at 24h, whereas MHC-II+ MM were more infected at 48h. The proportion of samples positive and negative for LCMV is indicated. Data are representative of 3 independent experiments, with 6 samples (24h) and 5 samples (48h).

Supplementary Table

Primer	**5'-3' sequence**
LCMV GP Forward	CAGAAATGTTGATGCTGGACTGC
LCMV GP Reverse	CAGACCTTGGCTTGCTTTACACAG
Actb Forward	AGCTCATTGTAGAAGGTGTGG
Actb Reverse	GTGGGAATGGGTCAGAAGG

References

1. Schwartz, M. & Baruch, K. The resolution of neuroinflammation in neurodegeneration: leukocyte recruitment via the choroid plexus. *EMBO J* **33**, 7-22 (2014).

2. Rua, R. & McGavern, D.B. Advances in Meningeal Immunity. *Trends Mol Med* (2018).

3. Mowat, A.M., Scott, C.L. & Bain, C.C. Barrier-tissue macrophages: functional adaptation to environmental challenges. *Nat Med* **23**, 1258-1270 (2017).

4. Van Hove, H. *et al.* A single-cell atlas of mouse brain macrophages reveals unique transcriptional identities shaped by ontogeny and tissue environment. *Nat Neurosci* **22**, 1021-1035 (2019).

5. Mrdjen, D. *et al.* High-Dimensional Single-Cell Mapping of Central Nervous System Immune Cells Reveals Distinct Myeloid Subsets in Health, Aging, and Disease. *Immunity* **48**, 380-395 e386 (2018).

6. Goldmann, T. *et al.* Origin, fate and dynamics of macrophages at central nervous system interfaces. *Nat Immunol* **17**, 797-805 (2016).

7. Fitzpatrick, Z. *et al.* Gut-educated IgA plasma cells defend the meningeal venous sinuses. *Nature* **587**, 472-476 (2020).

8. Cugurra, A. *et al.* Skull and vertebral bone marrow are myeloid cell reservoirs for the meninges and CNS parenchyma. *Science* **373** (2021).

9. Brioschi, S. *et al.* Heterogeneity of meningeal B cells reveals a lymphopoietic niche at the CNS borders. *Science* **373** (2021).

10. Schafflick, D. *et al.* Single-cell profiling of CNS border compartment leukocytes reveals that B cells and their progenitors reside in non-diseased meninges. *Nat Neurosci* **24**, 1225-1234 (2021).

11. Weller, R.O., Sharp, M.M., Christodoulides, M., Carare, R.O. & Mollgard, K. The meninges as barriers and facilitators for the movement of fluid, cells and pathogens related to the rodent and human CNS. *Acta Neuropathol* **135**, 363-385 (2018).

12. Dragunow, M. Meningeal and choroid plexus cells--novel drug targets for CNS disorders. *Brain Res* **1501**, 32-55 (2013).

13. Salvador, A.F., de Lima, K.A. & Kipnis, J. Neuromodulation by the immune system: a focus on cytokines. *Nat Rev Immunol* **21**, 526-541 (2021).

14. Waisman, A., Liblau, R.S. & Becher, B. Innate and adaptive immune responses in the CNS. *Lancet Neurol* **14**, 945-955 (2015).

15. Ellwardt, E., Walsh, J.T., Kipnis, J. & Zipp, F. Understanding the Role of T Cells in CNS Homeostasis. *Trends Immunol* **37**, 154-165 (2016).

16. Kipnis, J., Gadani, S. & Derecki, N.C. Pro-cognitive properties of T cells. *Nat Rev Immunol* **12**, 663-669 (2012).

17. Brynskikh, A., Warren, T., Zhu, J. & Kipnis, J. Adaptive immunity affects learning behavior in mice. *Brain Behav Immun* **22**, 861-869 (2008).

18. Kipnis, J., Cohen, H., Cardon, M., Ziv, Y. & Schwartz, M. T cell deficiency leads to cognitive dysfunction: implications for therapeutic vaccination for schizophrenia and other psychiatric conditions. *Proc Natl Acad Sci U S A* **101**, 8180-8185 (2004).

19. Prinz, M., Erny, D. & Hagemeyer, N. Ontogeny and homeostasis of CNS myeloid cells. *Nat Immunol* **18**, 385-392 (2017).

20. Rua, R. *et al.* Infection drives meningeal engraftment by inflammatory monocytes that impairs CNS immunity. *Nat Immunol* **20**, 407-419 (2019).

21. Manglani, M. & McGavern, D.B. New advances in CNS immunity against viral infection. *Curr Opin Virol* **28**, 116-126 (2017).

22. Etzerodt, A. *et al.* Specific targeting of CD163(+) TAMs mobilizes inflammatory monocytes and promotes T cell-mediated tumor regression. *J Exp Med* **216**, 2394-2411 (2019).

23. Jung, S.R. *et al.* Contribution of STAT1 to innate and adaptive immunity during type I interferon-mediated lethal virus infection. *PLoS Pathog* **16**, e1008525 (2020).

24. Clingan, J.M., Ostrow, K., Hosiawa, K.A., Chen, Z.J. & Matloubian, M. Differential roles for RIG-I-like receptors and nucleic acid-sensing TLR pathways in controlling a chronic viral infection. *J Immunol* **188**, 4432-4440 (2012).

25. Sunil Thomas, A.H., Yueh-Ming Loo, Hilario Ramos and Aimee McMillan. Cell intrinsic role for MAVS in regulating CD8 T cell fitness during acute virus infection (P6113). *J Immunol May 1, 2013, 190 (1 Supplement) 173.10;* (2013).

26. Perdiguero, E.G. & Geissmann, F. The development and maintenance of resident macrophages. *Nat Immunol* **17**, 2-8 (2016).

27. Franceschi, C., Garagnani, P., Parini, P., Giuliani, C. & Santoro, A. Inflammaging: a new immune-metabolic viewpoint for age-related diseases. *Nat Rev Endocrinol* **14**, 576-590 (2018).

28. Dulken, B.W. *et al.* Single-cell analysis reveals T cell infiltration in old neurogenic niches. *Nature* **571**, 205-210 (2019).

29. Baruch, K. *et al.* Aging. Aging-induced type I interferon response at the choroid plexus negatively affects brain function. *Science* **346**, 89-93 (2014).

30. Gaya, M. *et al.* Host response. Inflammation-induced disruption of SCS macrophages impairs B cell responses to secondary infection. *Science* **347**, 667-672 (2015).

31. Barth, M.W., Hendrzak, J.A., Melnicoff, M.J. & Morahan, P.S. Review of the macrophage disappearance reaction. *J Leukoc Biol* **57**, 361-367 (1995).

32. Ginhoux, F., Bleriot, C. & Lecuit, M. Dying for a Cause: Regulated Necrosis of Tissue-Resident Macrophages upon Infection. *Trends Immunol* **38**, 693-695 (2017).

33. Kaiser, T. & Feng, G. Tmem119-EGFP and Tmem119-CreERT2 Transgenic Mice for Labeling and Manipulating Microglia. *eNeuro* **6** (2019).

34. Masuda, T. *et al.* Novel Hexb-based tools for studying microglia in the CNS. *Nat Immunol* **21**, 802-815 (2020).

35. Asano, K. *et al.* Intestinal CD169(+) macrophages initiate mucosal inflammation by secreting CCL8 that recruits inflammatory monocytes. *Nat Commun* **6**, 7802 (2015).

36. Abtin, A. *et al.* Perivascular macrophages mediate neutrophil recruitment during bacterial skin infection. *Nat Immunol* **15**, 45-53 (2014).

37. Steel, C.D. *et al.* Distinct macrophage subpopulations regulate viral encephalitis but not viral clearance in the CNS. *J Neuroimmunol* **226**, 81-92 (2010).

38. Polfliet, M.M. *et al.* Meningeal and perivascular macrophages of the central nervous system play a protective role during bacterial meningitis. *J Immunol* **167**, 4644-4650 (2001).

39. Polfliet, M.M. *et al.* A method for the selective depletion of perivascular and meningeal macrophages in the central nervous system. *J Neuroimmunol* **116**, 188-195 (2001).

40. Hoeffel, G. & Ginhoux, F. Fetal monocytes and the origins of tissue-resident macrophages. *Cell Immunol* **330**, 5-15 (2018).

41. Mass, E. Delineating the origins, developmental programs and homeostatic functions of tissue-resident macrophages. *Int Immunol* **30**, 493-501 (2018).

42. Casanova-Acebes, M. *et al.* Tissue-resident macrophages provide a pro-tumorigenic niche to early NSCLC cells. *Nature* **595**, 578-584 (2021).

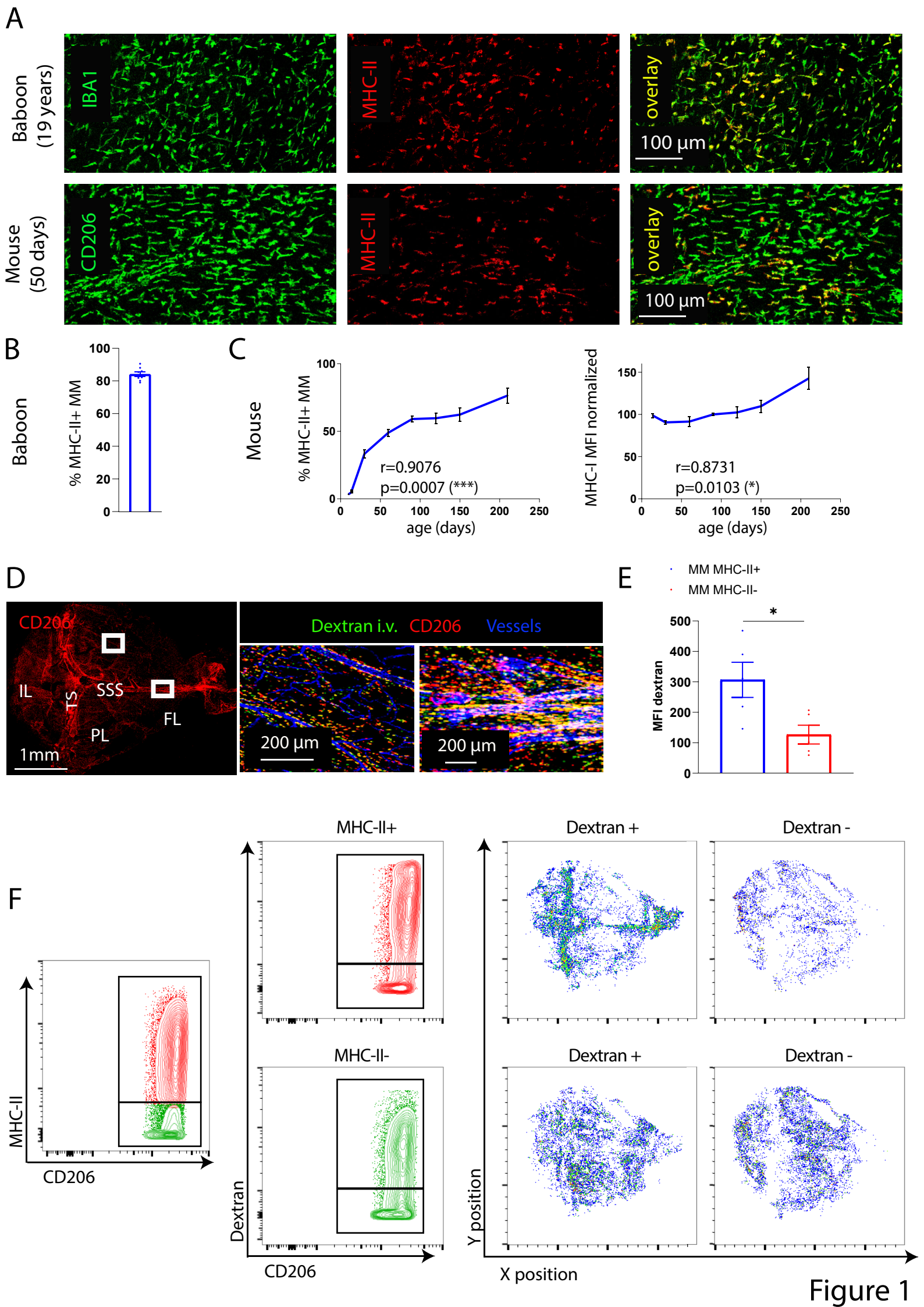
A
Baboon (19 years)
IBA1
MHC-II
overlay
100 µm
Mouse (50 days)
CD206
MHC-II
overlay
100 µm
B
Baboon
% MHC-II+ MM
C
Mouse
% MHC-II+ MM
r=0.9076
p=0.0007 (***)
age (days)
MHC-I MFI normalized
r=0.8731
p=0.0103 (*)
age (days)
D
CD206
IL
TS
SSS
FL
PL
1mm
Dextran i.v.
CD206
Vessels
200 µm
200 µm
E
MM MHC-II+
MM MHC-II-
MFI dextran
F
MHC-II+
Dextran +
Dextran -
MHC-II-
Dextran +
Dextran -
MHC-II
CD206
Dextran
CD206
Y position
X position

Figure 1

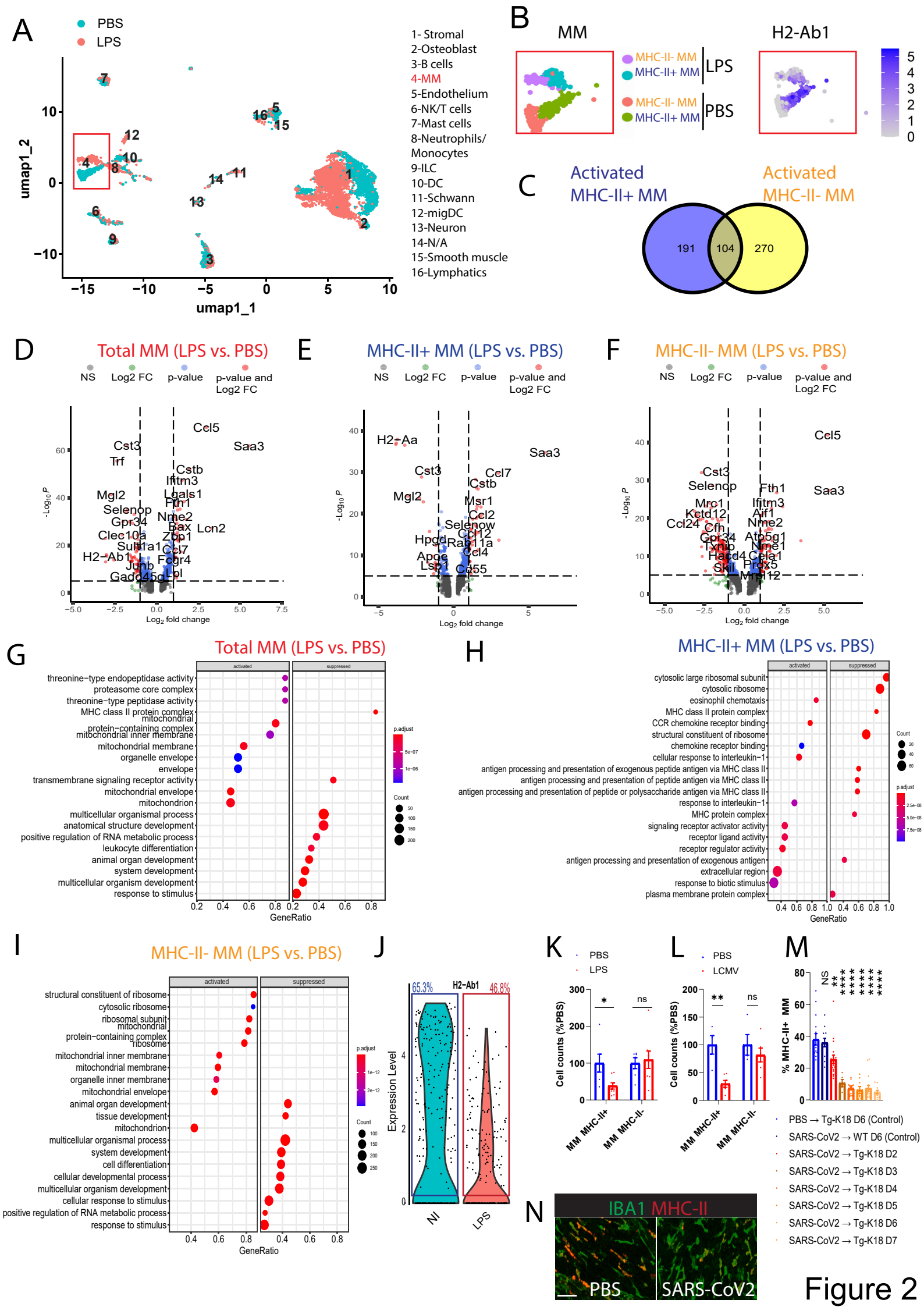
A
PBS
LPS
umap1_2
umap1_1
1- Stromal
2-Osteoblast
3-B cells
4-MM
5-Endothelium
6-NK/T cells
7-Mast cells
8-Neutrophils/
Monocytes
9-ILC
10-DC
11-Schwann
12-migDC
13-Neuron
14-N/A
15-Smooth muscle
16-Lymphatics
B
MM
MHC-II- MM
MHC-II+ MM
LPS
MHC-II- MM
MHC-II+ MM
PBS
H2-Ab1
C
Activated
MHC-II+ MM
Activated
MHC-II- MM
191
104
270
D
Total MM (LPS vs. PBS)
E
MHC-II+ MM (LPS vs. PBS)
F
MHC-II- MM (LPS vs. PBS)
NS
Log2 FC
p-value
p-value and
Log2 FC
Log2 fold change
G
Total MM (LPS vs. PBS)
H
MHC-II+ MM (LPS vs. PBS)
activated
suppressed
GeneRatio
I
MHC-II- MM (LPS vs. PBS)
J
H2-Ab1
65.3%
46.8%
Expression Level
NI
LPS
K
PBS
LPS
Cell counts (%PBS)
MM MHC-II+
MM MHC-II-
L
PBS
LCMV
M
% MHC-II+ MM
PBS → Tg-K18 D6 (Control)
SARS-CoV2 → WT D6 (Control)
SARS-CoV2 → Tg-K18 D2
SARS-CoV2 → Tg-K18 D3
SARS-CoV2 → Tg-K18 D4
SARS-CoV2 → Tg-K18 D5
SARS-CoV2 → Tg-K18 D6
SARS-CoV2 → Tg-K18 D7
N
IBA1 MHC-II
PBS
SARS-CoV2

Figure 2

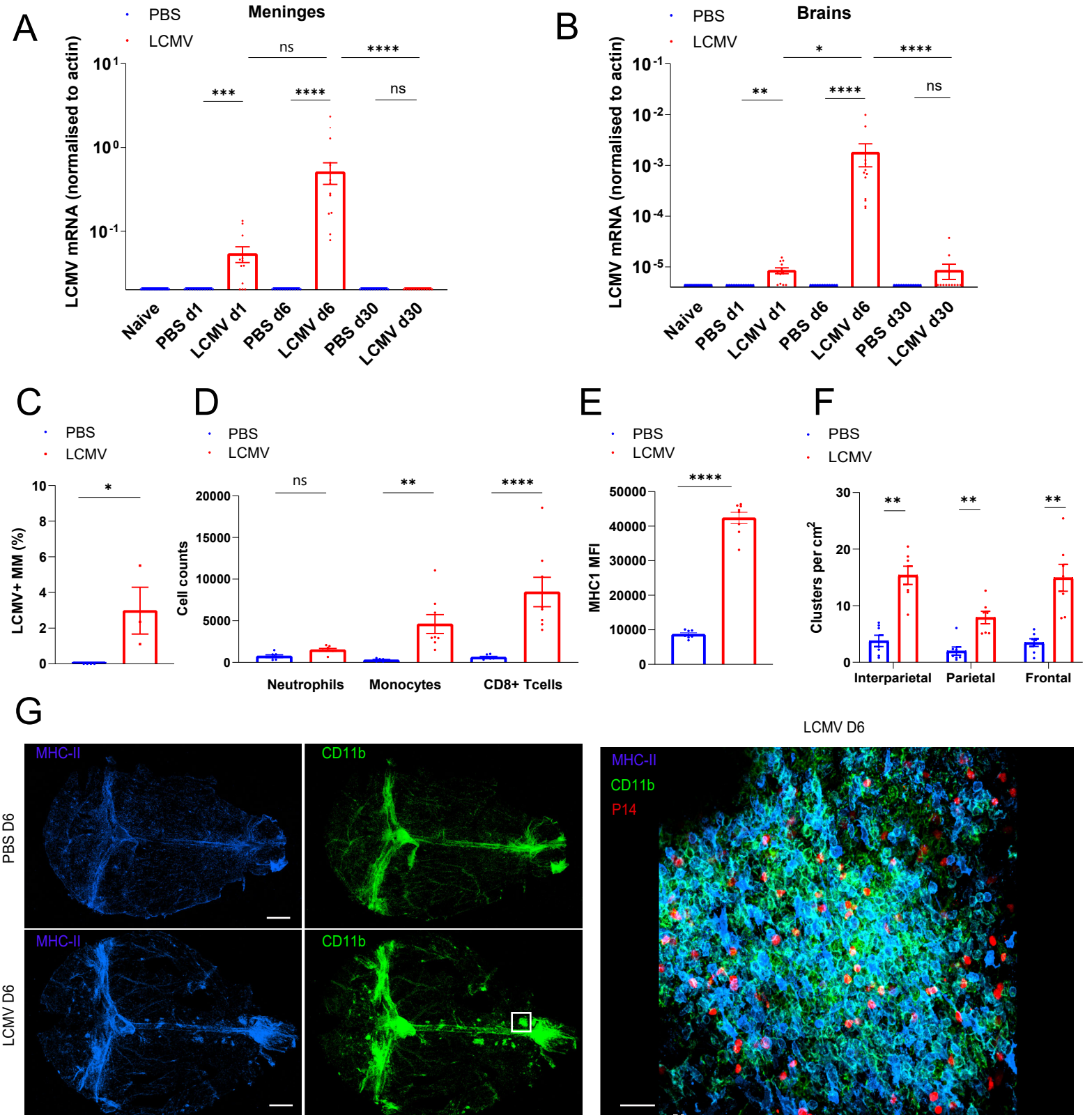
A
Meninges
PBS
LCMV
LCMV mRNA (normalised to actin)
ns
****
***
****
ns
Naive
PBS d1
LCMV d1
PBS d6
LCMV d6
PBS d30
LCMV d30
B
Brains
PBS
LCMV
LCMV mRNA (normalised to actin)
*
****
**
****
ns
Naive
PBS d1
LCMV d1
PBS d6
LCMV d6
PBS d30
LCMV d30
C
PBS
LCMV
LCMV+ MM (%)
*
D
PBS
LCMV
Cell counts
ns
**
****
Neutrophils
Monocytes
CD8+ Tcells
E
PBS
LCMV
MHC1 MFI
****
F
PBS
LCMV
Clusters per cm2
**
**
**
Interparietal
Parietal
Frontal
G
LCMV D6
PBS D6
LCMV D6
MHC-II
CD11b
MHC-II
CD11b
MHC-II
CD11b
P14

Figure 3

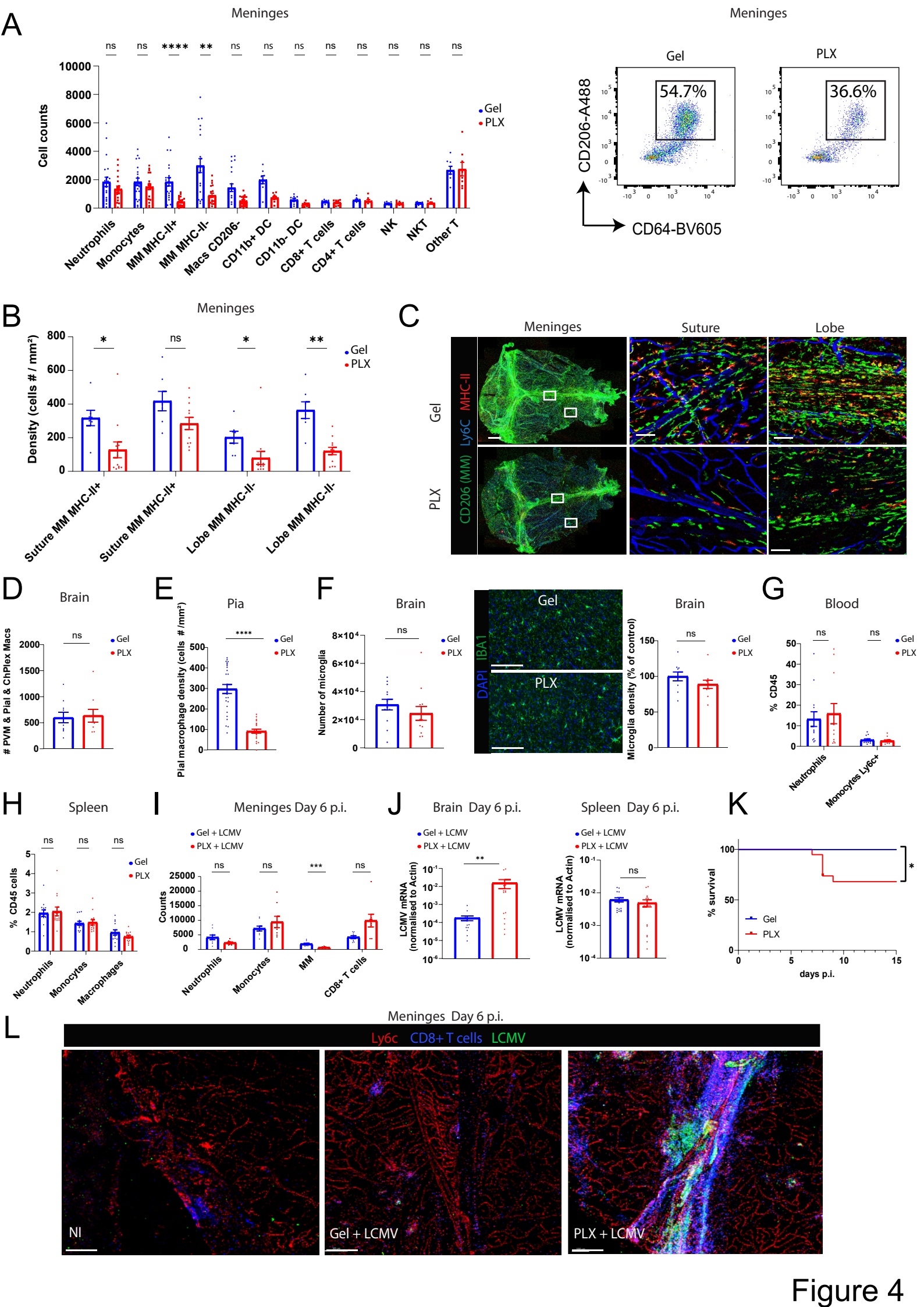
A
Meninges
ns ns **** ** ns ns ns ns ns ns ns ns
Cell counts
10000
8000
6000
4000
2000
0
Gel
PLX
Neutrophils
Monocytes
MM MHC-II+
MM MHC-II-
Macs CD206-
CD11b+ DC
CD11b- DC
CD8+ T cells
CD4+ T cells
NK
NKT
Other T
Meninges
Gel
PLX
54.7%
36.6%
CD206-A488
CD64-BV605
B
Meninges
Density (cells # / mm²)
800
600
400
200
0
* ns * **
Gel
PLX
Suture MM MHC-II+
Suture MM MHC-II+
Lobe MM MHC-II-
Lobe MM MHC-II-
C
Meninges
Suture
Lobe
Gel
PLX
MHC-II
Ly6C
CD206 (MM)
D
Brain
PVM & Pial & ChPlex Macs
2000
1500
1000
500
0
ns
Gel
PLX
E
Pia
Pial macrophage density (cells #/mm²)
500
400
300
200
100
0
****
Gel
PLX
F
Brain
Number of microglia
8×10⁴
6×10⁴
4×10⁴
2×10⁴
0
ns
Gel
PLX
Gel
PLX
IBA1
DAPI
Brain
Microglia density (% of control)
150
100
50
0
ns
Gel
PLX
G
Blood
% CD45
50
40
30
20
10
0
ns ns
Gel
PLX
Neutrophils
Monocytes Ly6c+
H
Spleen
% CD45 cells
5
4
3
2
1
0
ns ns ns
Gel
PLX
Neutrophils
Monocytes
Macrophages
I
Meninges Day 6 p.i.
Gel + LCMV
PLX + LCMV
Counts
25000
20000
15000
10000
5000
0
ns ns *** ns
Neutrophils
Monocytes
MM
CD8+ T cells
J
Brain Day 6 p.i.
Gel + LCMV
PLX + LCMV
LCMV mRNA (normalised to Actin)
10⁻¹
10⁻²
10⁻³
10⁻⁴
10⁻⁵
10⁻⁶
**
Spleen Day 6 p.i.
Gel + LCMV
PLX + LCMV
LCMV mRNA (normalised to Actin)
10⁻¹
10⁻²
10⁻³
10⁻⁴
ns
K
% survival
100
50
0
*
Gel
PLX
0
5
10
15
days p.i.
L
Meninges Day 6 p.i.
Ly6c CD8+ T cells LCMV
NI
Gel + LCMV
PLX + LCMV

Figure 4

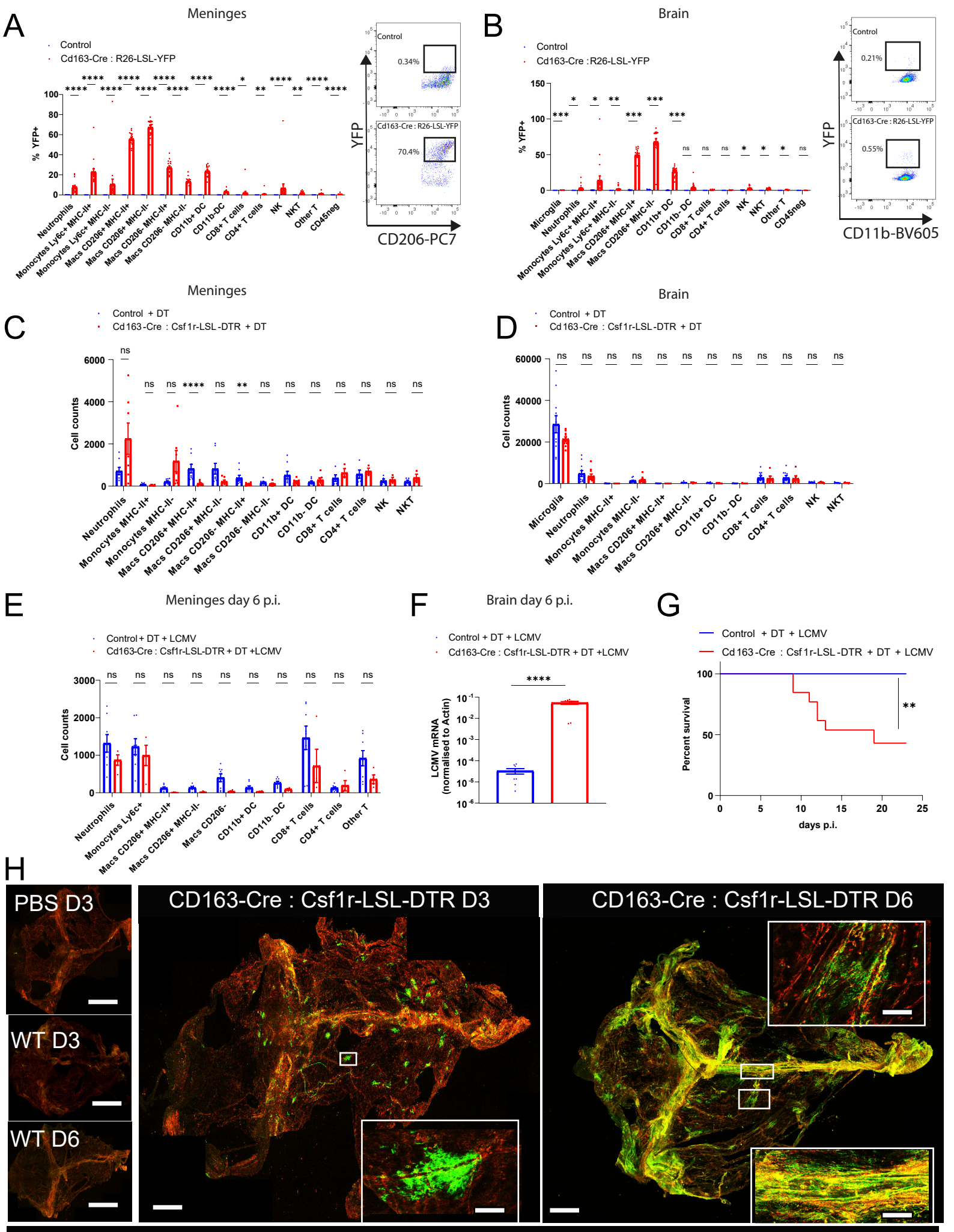
A
Meninges
Control
Cd163-Cre : R26-LSL-YFP
% YFP+
Neutrophils
Monocytes Ly6c+ MHC-II+
Monocytes Ly6c+ MHC-II-
Macs CD206+ MHC-II+
Macs CD206+ MHC-II-
Macs CD206- MHC-II+
Macs CD206- MHC-II-
CD11b+ DC
CD11b- DC
CD8+ T cells
CD4+ T cells
NK
NKT
Other T
CD45neg
Control
0.34%
Cd163-Cre : R26-LSL-YFP
70.4%
YFP
CD206-PC7
B
Brain
Control
Cd163-Cre :R26-LSL-YFP
% YFP+
Microglia
Neutrophils
Monocytes Ly6c+ MHC-II+
Monocytes Ly6c+ MHC-II-
Macs CD206+ MHC-II+
Macs CD206+ MHC-II-
CD11b+ DC
CD11b- DC
CD8+ T cells
CD4+ T cells
NK
NKT
Other T
CD45neg
Control
0.21%
Cd163-Cre : R26-LSL-YFP
0.55%
YFP
CD11b-BV605
C
Meninges
Control + DT
Cd163-Cre : Csf1r-LSL-DTR + DT
Cell counts
Neutrophils
Monocytes MHC-II+
Monocytes MHC-II-
Macs CD206+ MHC-II+
Macs CD206+ MHC-II-
Macs CD206- MHC-II+
Macs CD206- MHC-II-
CD11b+ DC
CD11b- DC
CD8+ T cells
CD4+ T cells
NK
NKT
D
Brain
Control + DT
Cd163-Cre : Csf1r-LSL-DTR + DT
Cell counts
Microglia
Neutrophils
Monocytes MHC-II+
Monocytes MHC-II-
Macs CD206+ MHC-II+
Macs CD206+ MHC-II-
CD11b+ DC
CD11b- DC
CD8+ T cells
CD4+ T cells
NK
NKT
E
Meninges day 6 p.i.
Control + DT + LCMV
Cd163-Cre : Csf1r-LSL-DTR + DT +LCMV
Cell counts
Neutrophils
Monocytes Ly6c+
Macs CD206+ MHC-II+
Macs CD206+ MHC-II-
Macs CD206-
CD11b+ DC
CD11b- DC
CD8+ T cells
CD4+ T cells
Other T
F
Brain day 6 p.i.
Control + DT + LCMV
Cd163-Cre : Csf1r-LSL-DTR + DT +LCMV
LCMV mRNA (normalised to Actin)
G
Control + DT + LCMV
Cd163-Cre : Csf1r-LSL-DTR + DT + LCMV
Percent survival
days p.i.
H
PBS D3
WT D3
WT D6
CD163-Cre : Csf1r-LSL-DTR D3
CD163-Cre : Csf1r-LSL-DTR D6
LCMV IBA1 (macrophages)

Figure 5

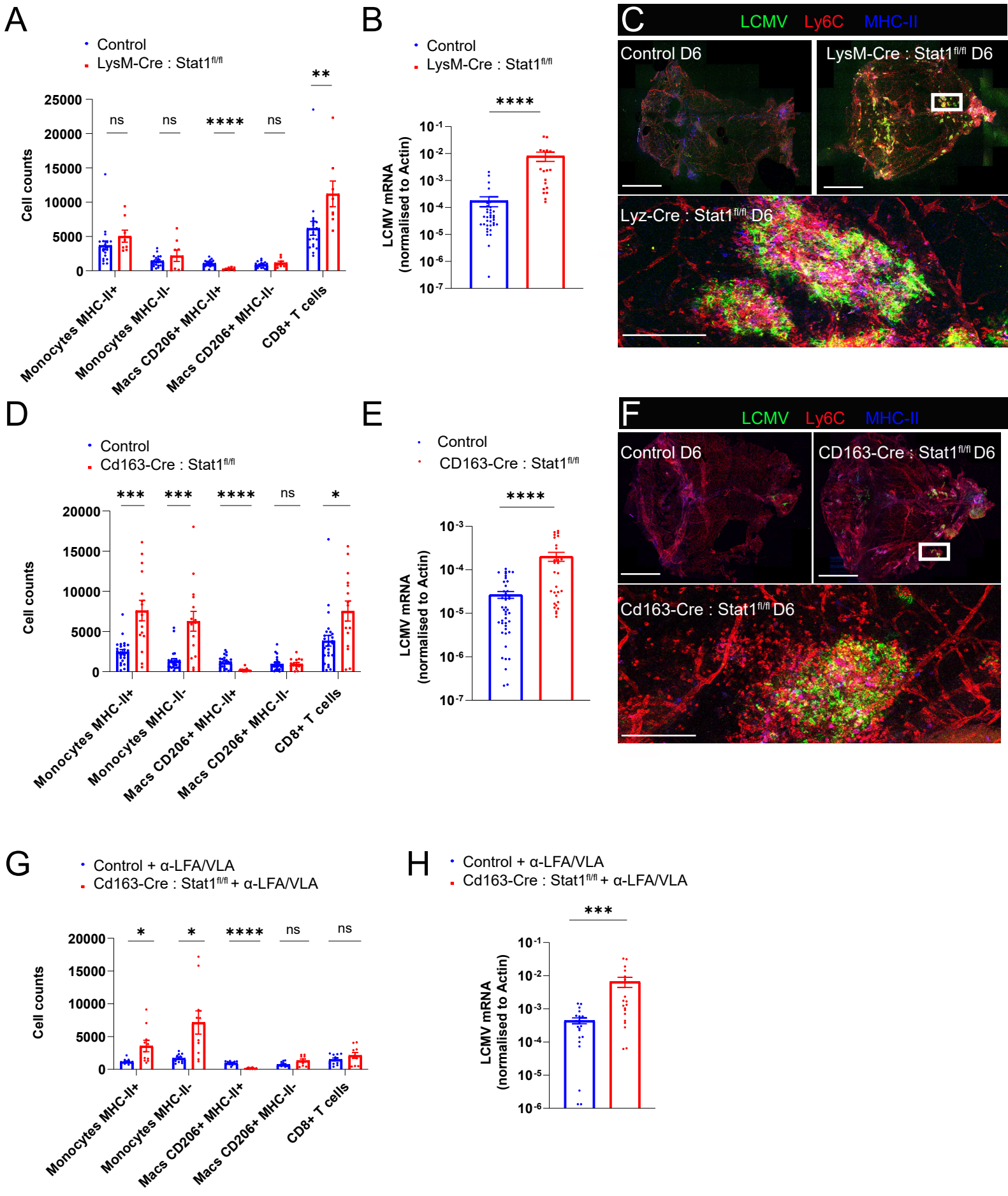
A
Control
LysM-Cre : Stat1fl/fl
Cell counts
25000
20000
15000
10000
5000
0
ns
ns
****
ns
**
Monocytes MHC-II+
Monocytes MHC-II-
Macs CD206+ MHC-II+
Macs CD206+ MHC-II-
CD8+ T cells
B
Control
LysM-Cre : Stat1fl/fl
****
LCMV mRNA (normalised to Actin)
10-1
10-2
10-3
10-4
10-5
10-6
10-7
C
LCMV Ly6C MHC-II
Control D6
LysM-Cre : Stat1fl/fl D6
Lyz-Cre : Stat1fl/fl D6
D
Control
Cd163-Cre : Stat1fl/fl
***
***
****
ns
*
Cell counts
20000
15000
10000
5000
0
Monocytes MHC-II+
Monocytes MHC-II-
Macs CD206+ MHC-II+
Macs CD206+ MHC-II-
CD8+ T cells
E
Control
CD163-Cre : Stat1fl/fl
****
LCMV mRNA (normalised to Actin)
10-3
10-4
10-5
10-6
10-7
F
LCMV Ly6C MHC-II
Control D6
CD163-Cre : Stat1fl/fl D6
Cd163-Cre : Stat1fl/fl D6
G
Control + α-LFA/VLA
Cd163-Cre : Stat1fl/fl + α-LFA/VLA
Cell counts
20000
15000
10000
5000
0
*
*
****
ns
ns
Monocytes MHC-II+
Monocytes MHC-II-
Macs CD206+ MHC-II+
Macs CD206+ MHC-II-
CD8+ T cells
H
Control + α-LFA/VLA
Cd163-Cre : Stat1fl/fl + α-LFA/VLA
***
LCMV mRNA (normalised to Actin)
10-1
10-2
10-3
10-4
10-5
10-6

Figure 6

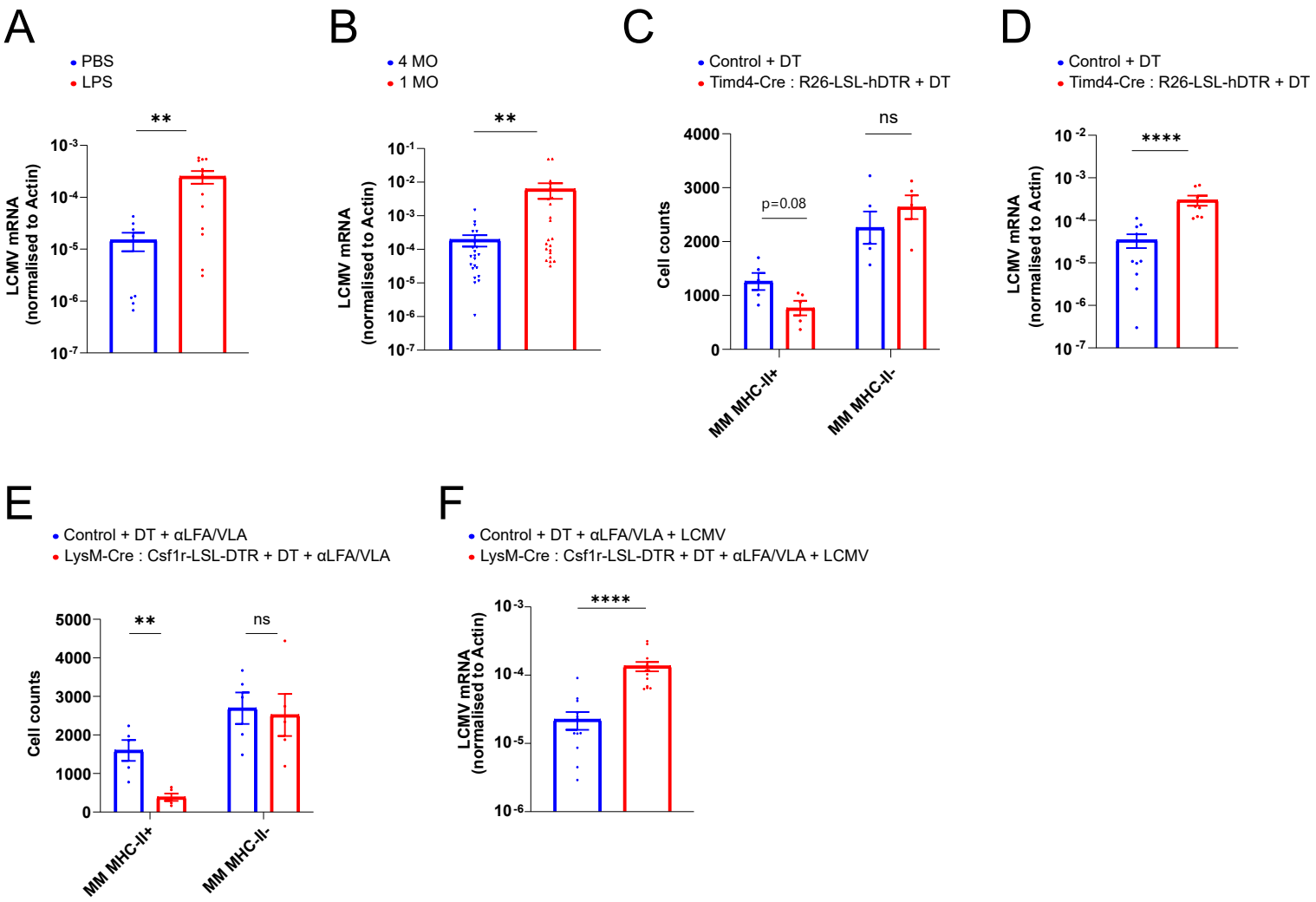
A
PBS
LPS
**
LCMV mRNA (normalised to Actin)
B
4 MO
1 MO
**
LCMV mRNA (normalised to Actin)
C
Control + DT
Timd4-Cre : R26-LSL-hDTR + DT
p=0.08
ns
Cell counts
MM MHC-II+
MM MHC-II-
D
Control + DT
Timd4-Cre : R26-LSL-hDTR + DT
****
LCMV mRNA (normalised to Actin)
E
Control + DT + αLFA/VLA
LysM-Cre : Csf1r-LSL-DTR + DT + αLFA/VLA
**
ns
Cell counts
MM MHC-II+
MM MHC-II-
F
Control + DT + αLFA/VLA + LCMV
LysM-Cre : Csf1r-LSL-DTR + DT + αLFA/VLA + LCMV
****
LCMV mRNA (normalised to Actin)

Figure 7

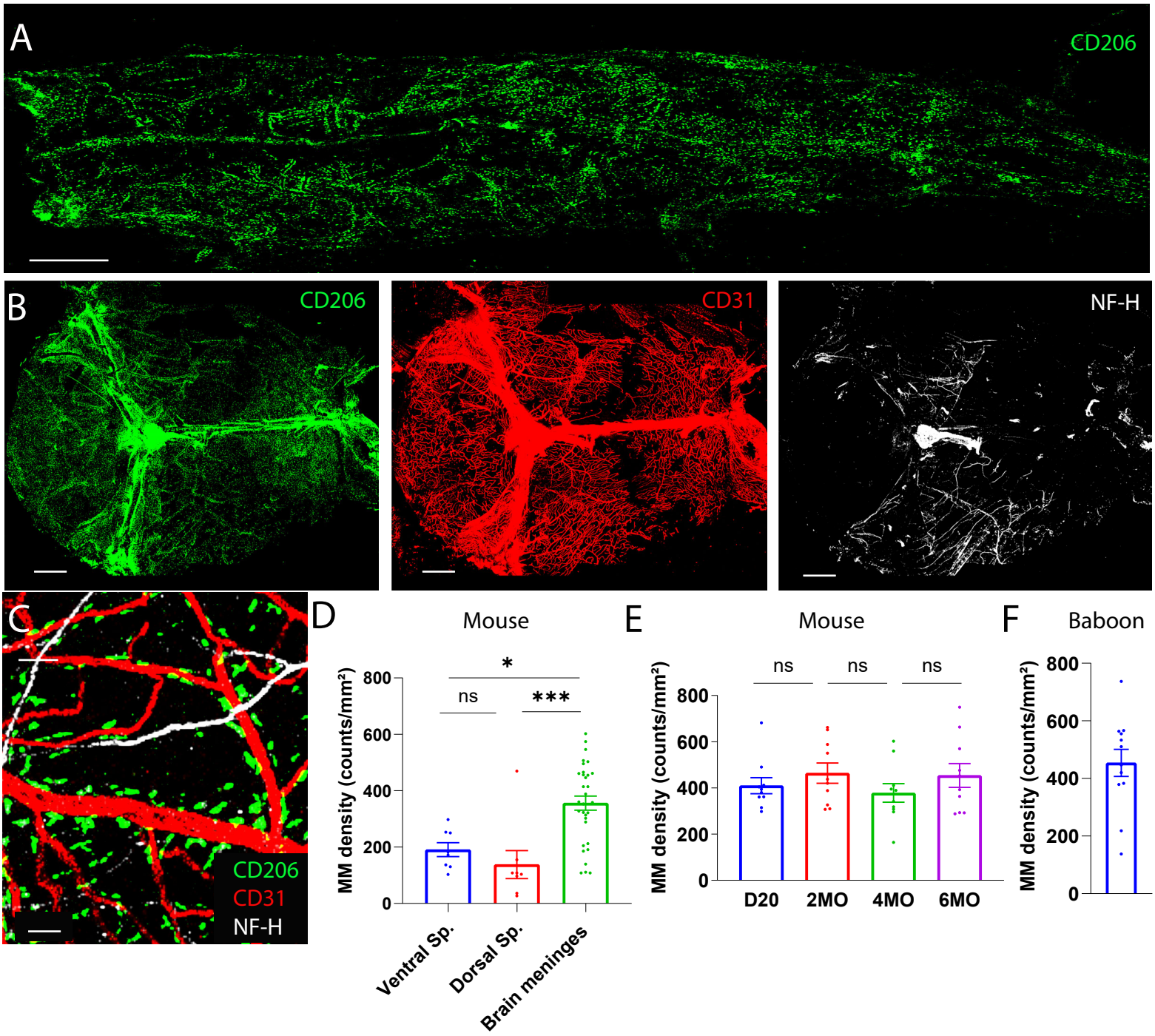

Supplementary Figure 1

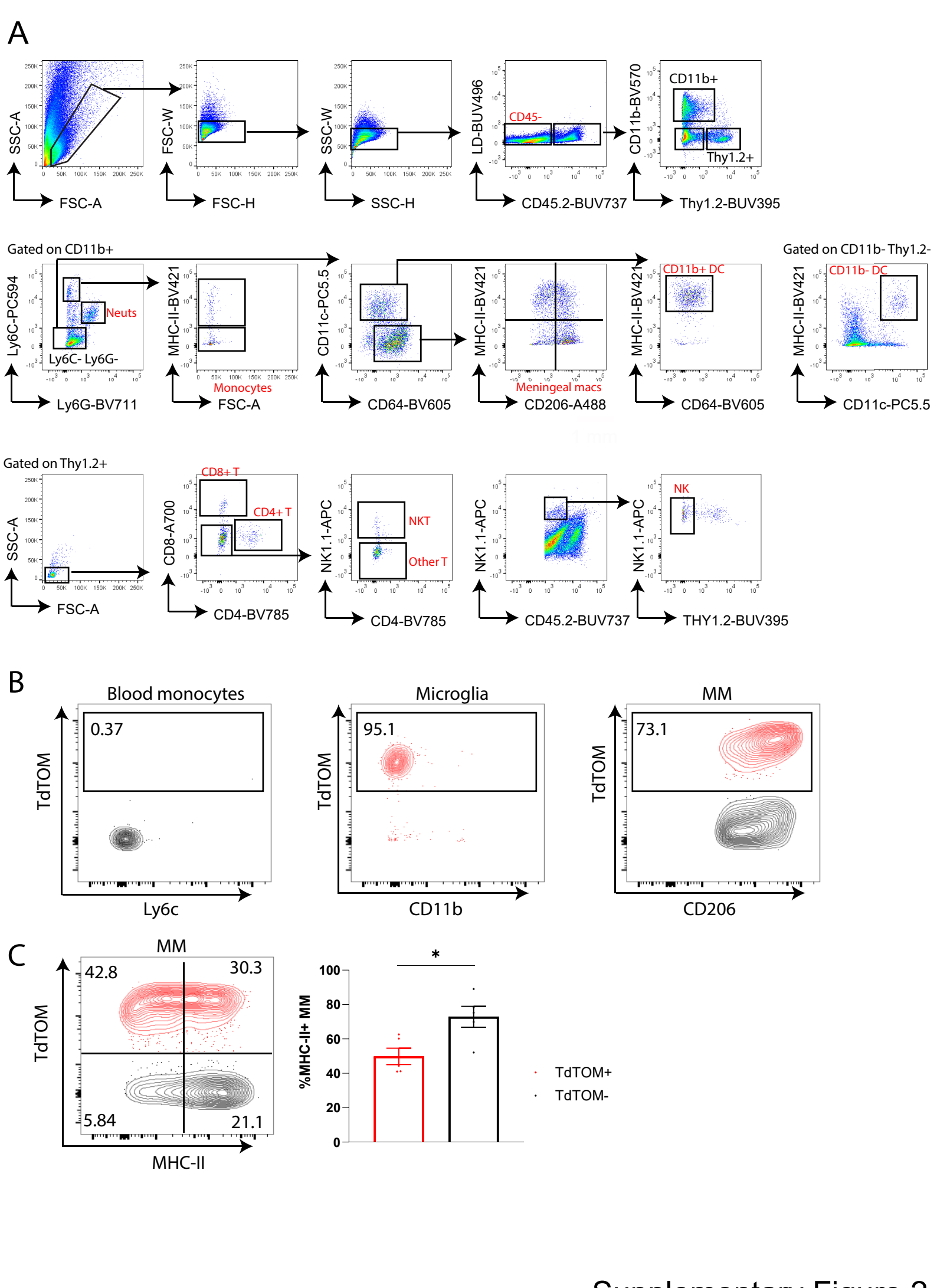

Supplementary Figure 2

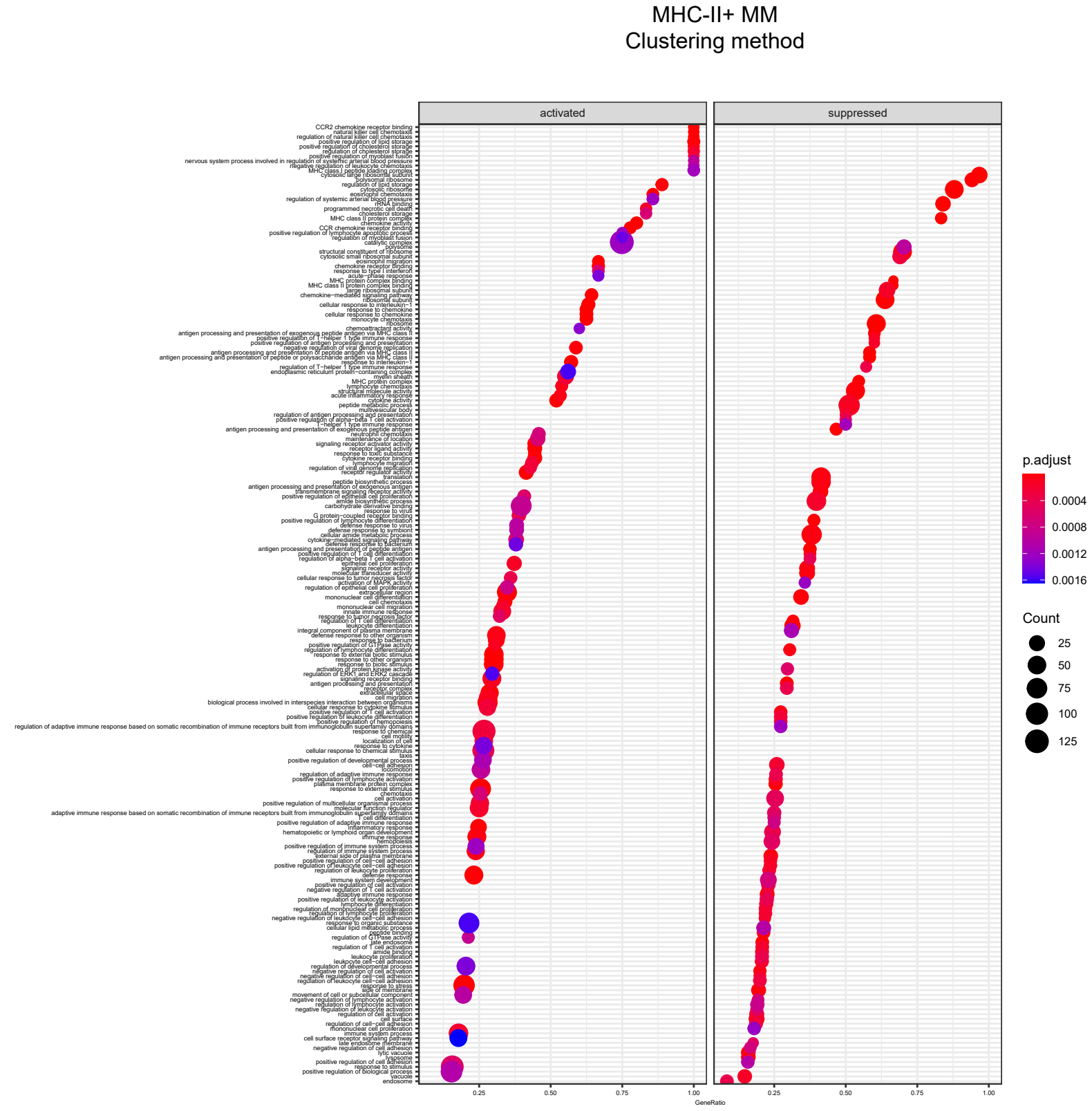

Supplementary Figure 3

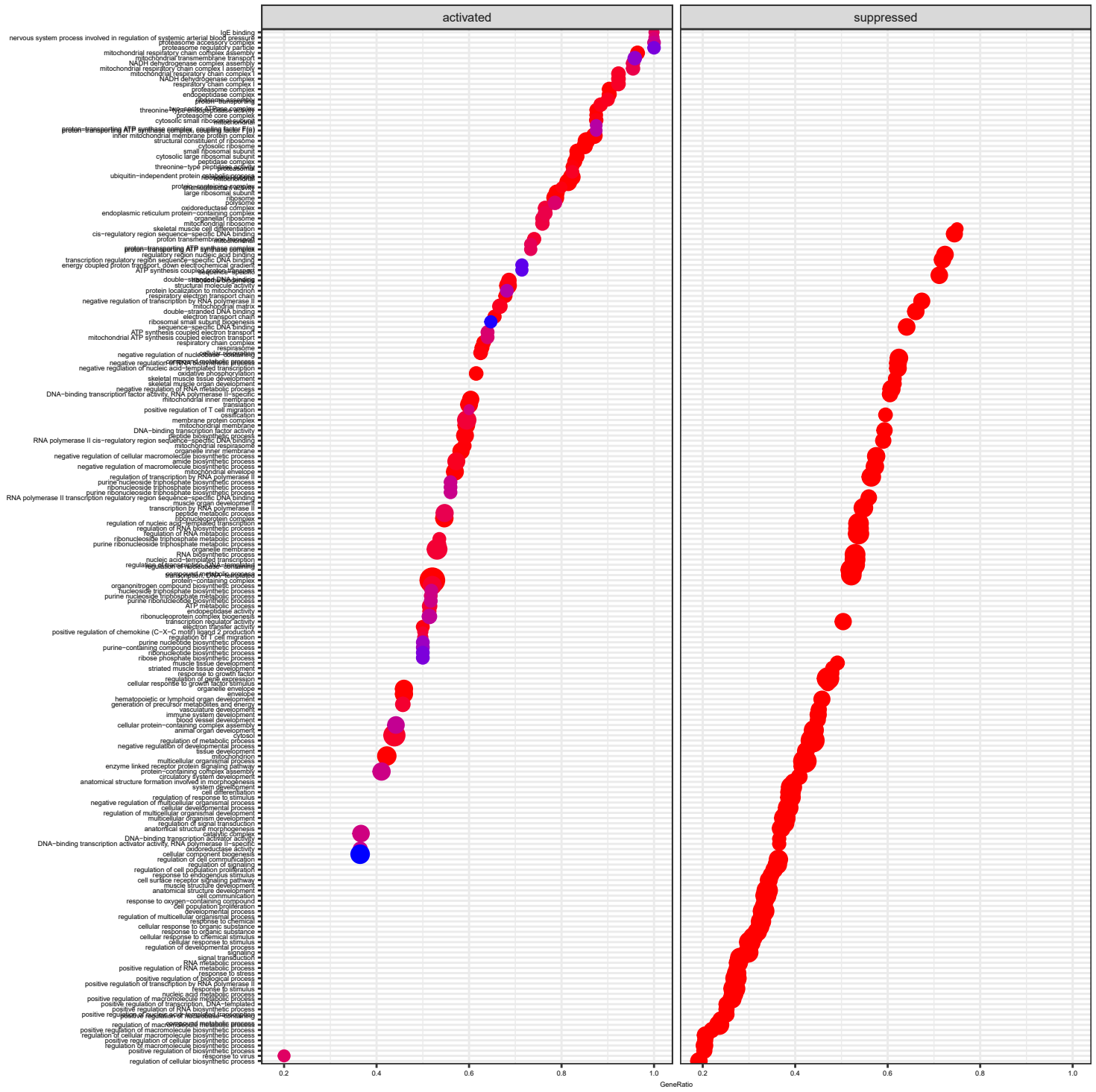

Supplementary Figure 4

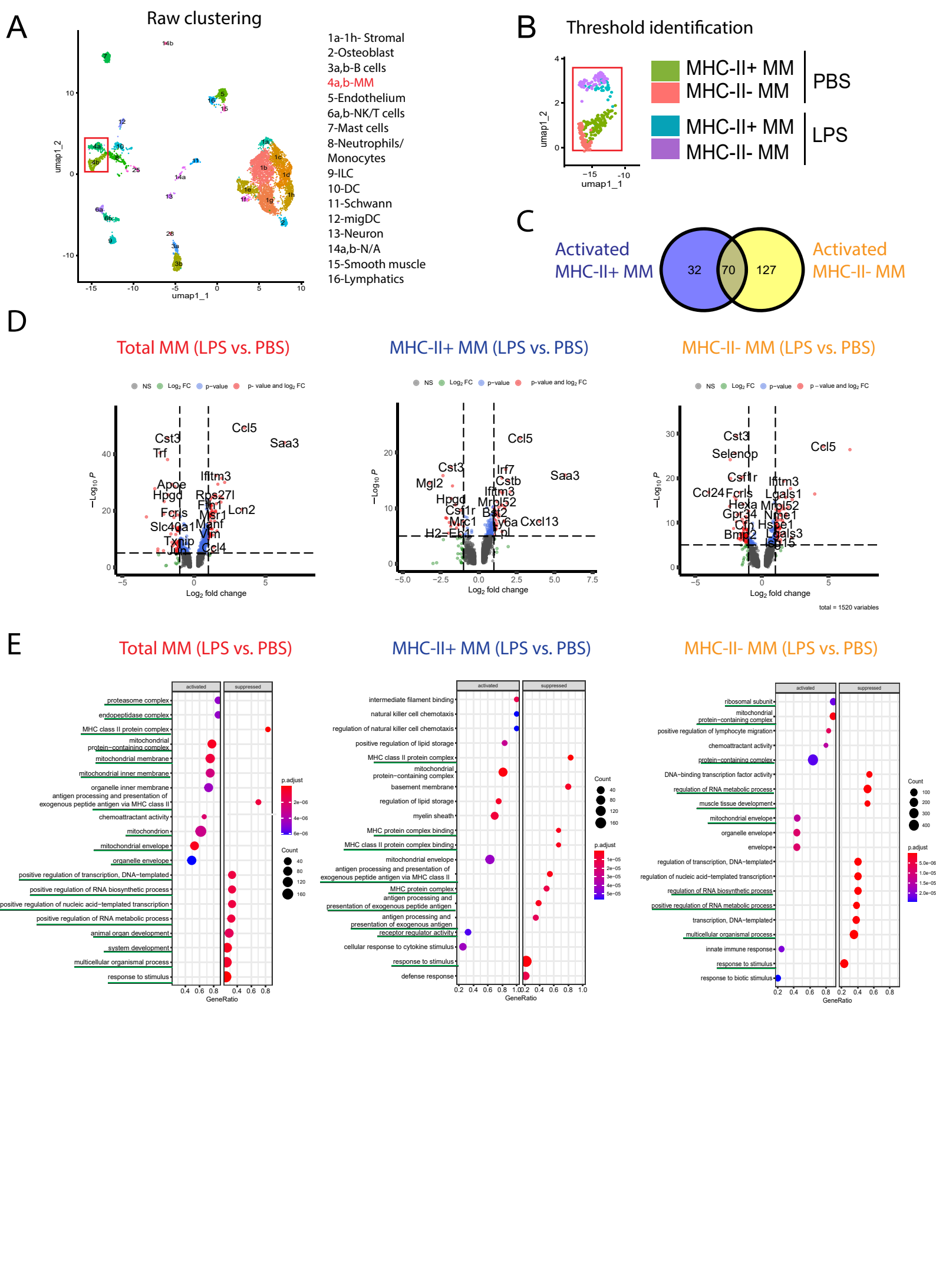

Supplementary Figure 5

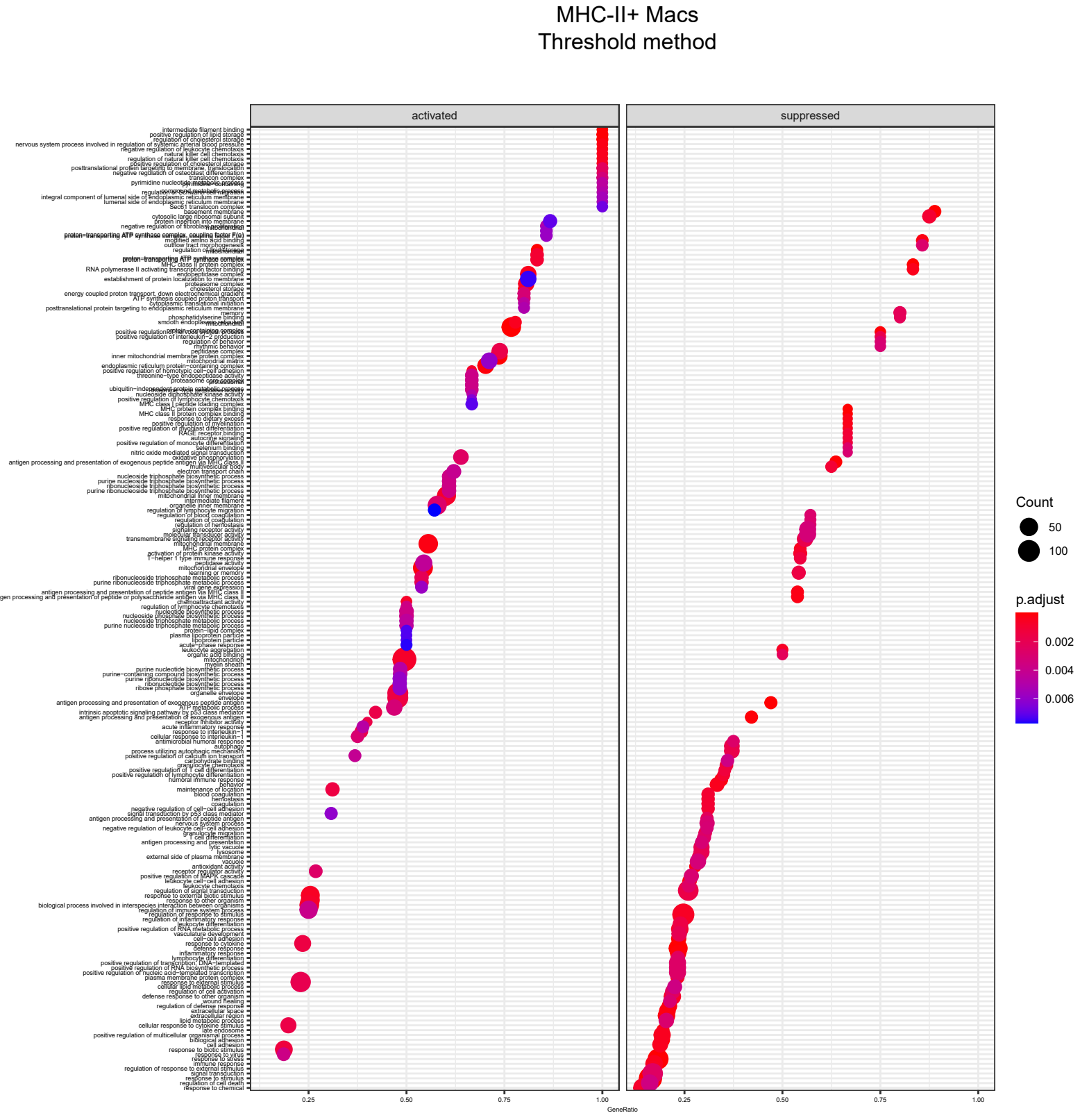

Supplementary Figure 6

MHC-II- Macs
Threshold method

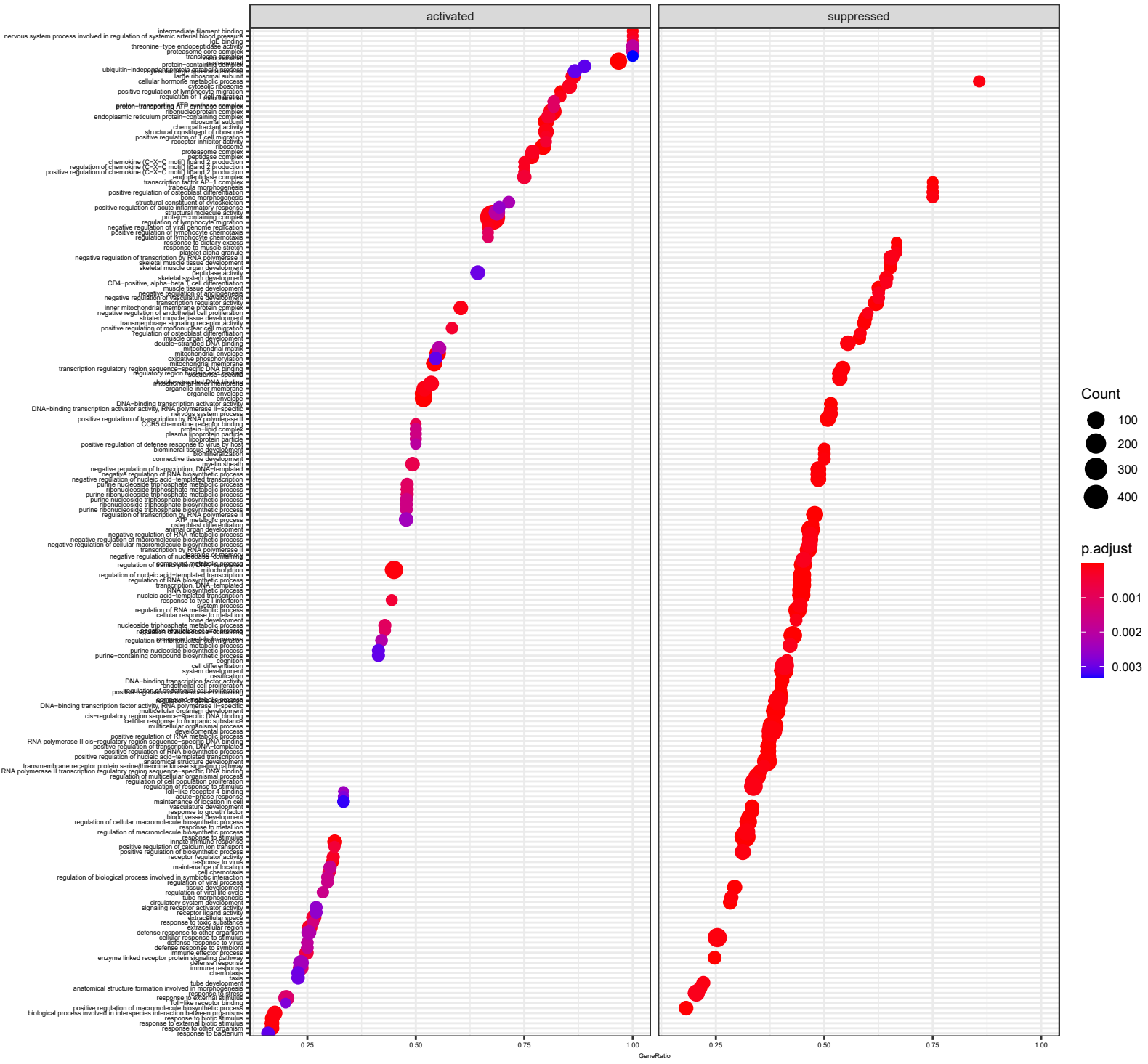

Supplemental Figure 7

A

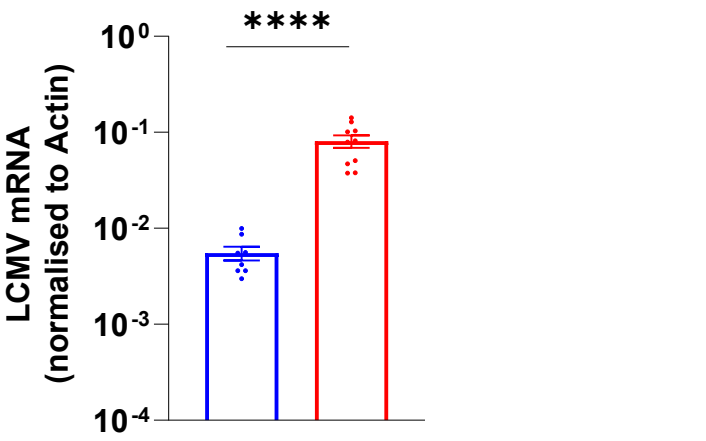

Supplementary Figure 8

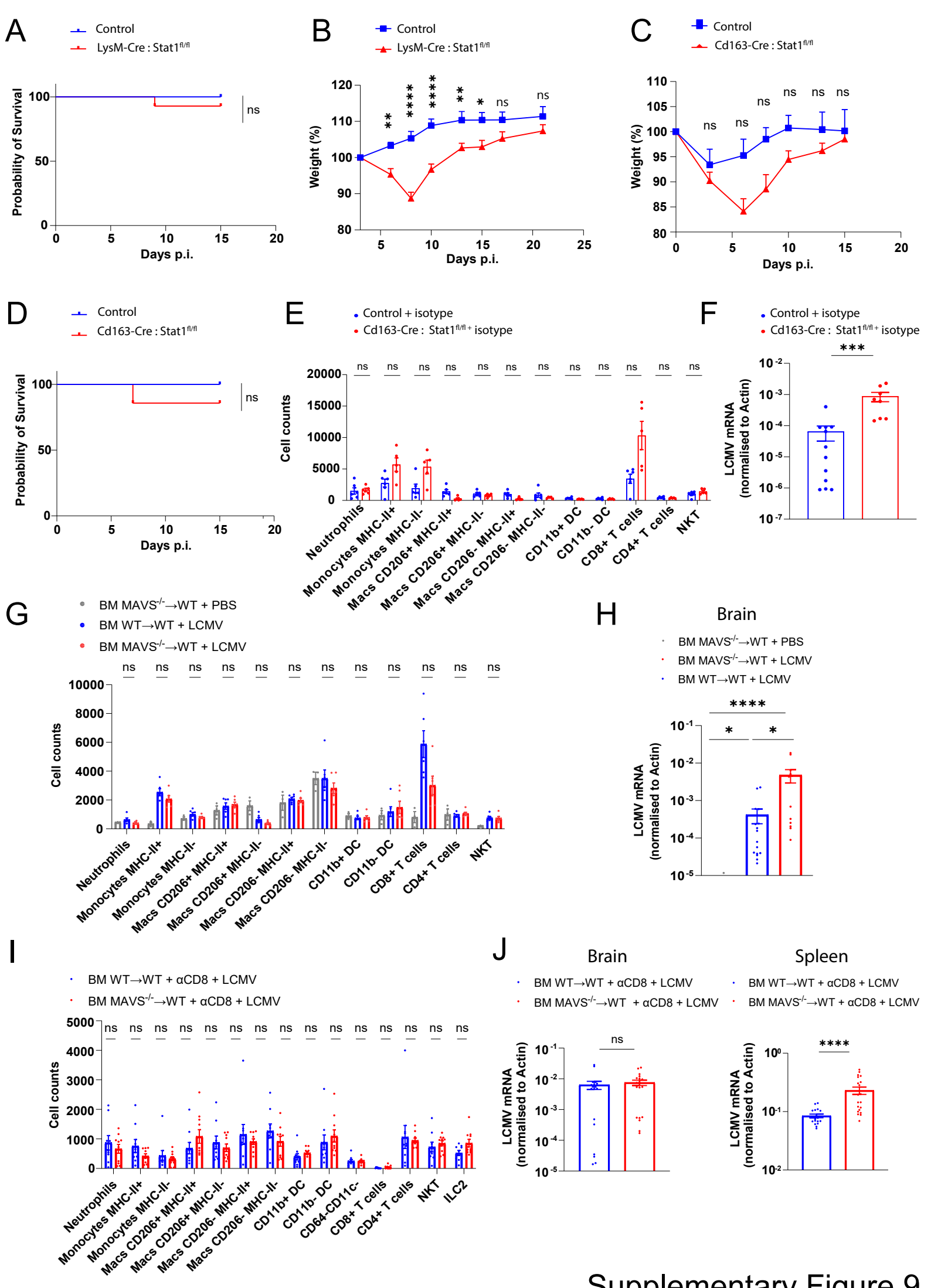

Supplementary Figure 9

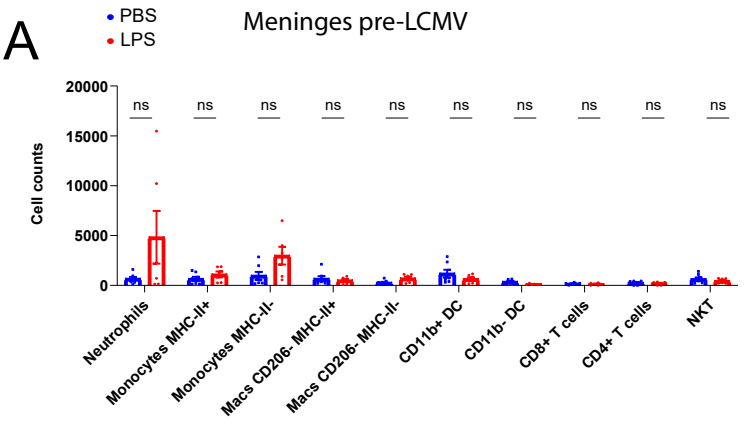

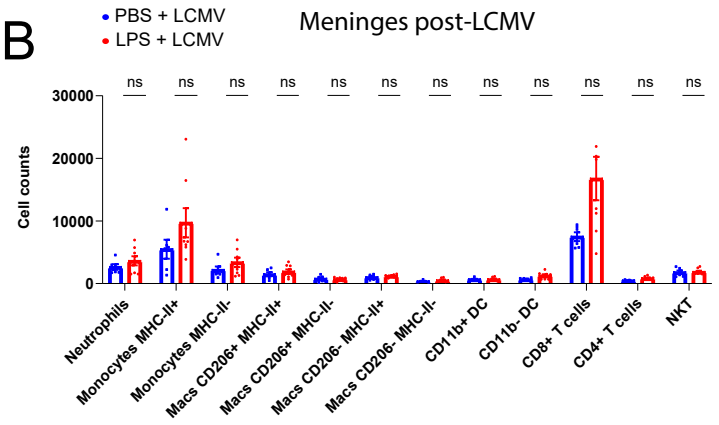

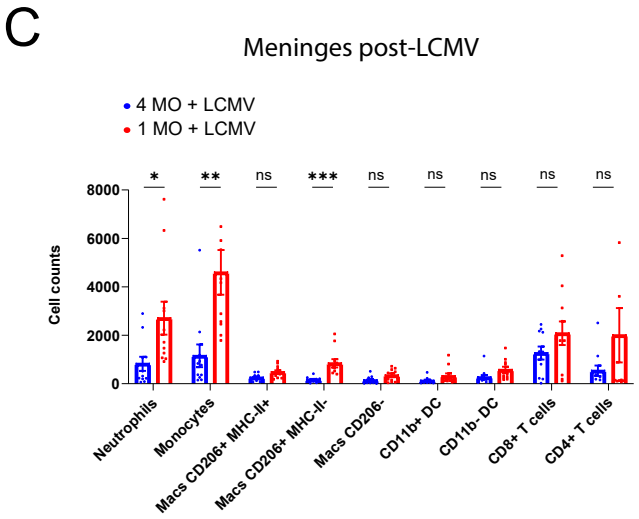

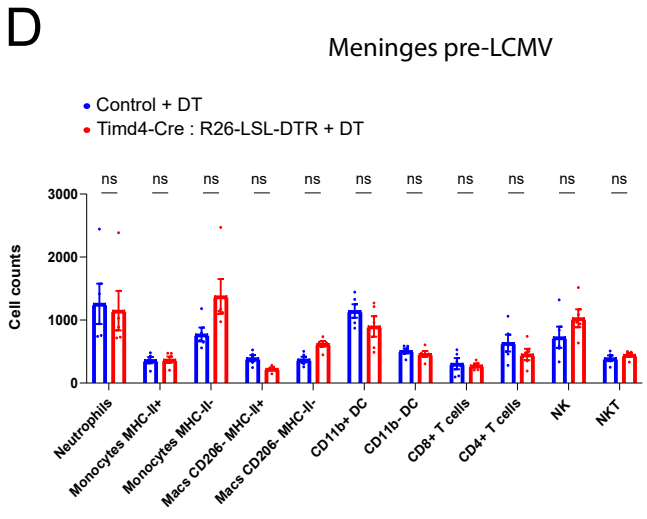

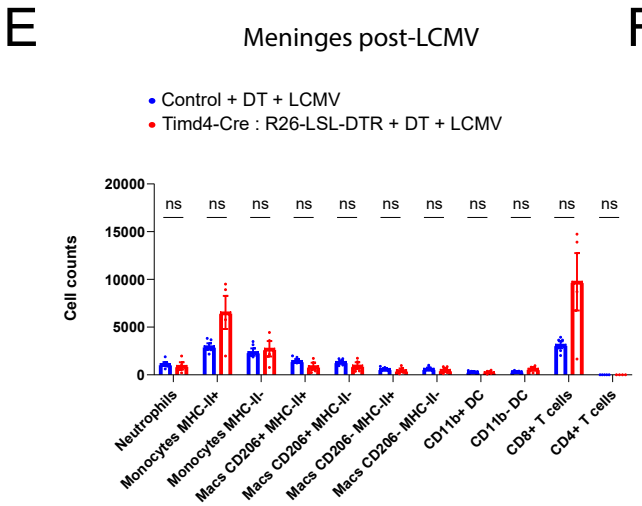

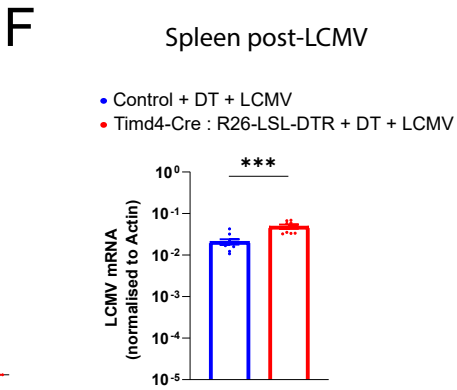

Supplementary Figure 10

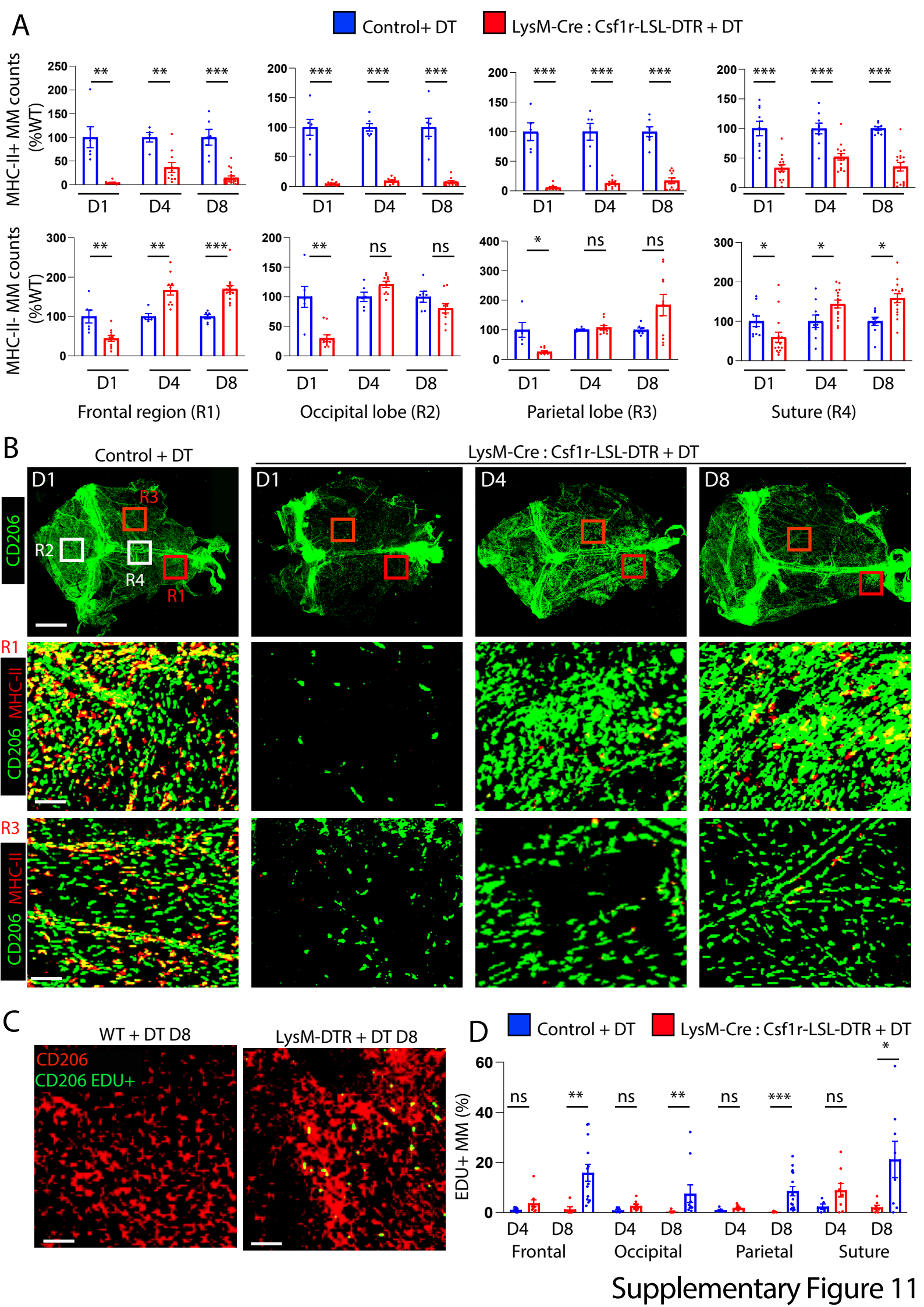

Supplementary Figure 11

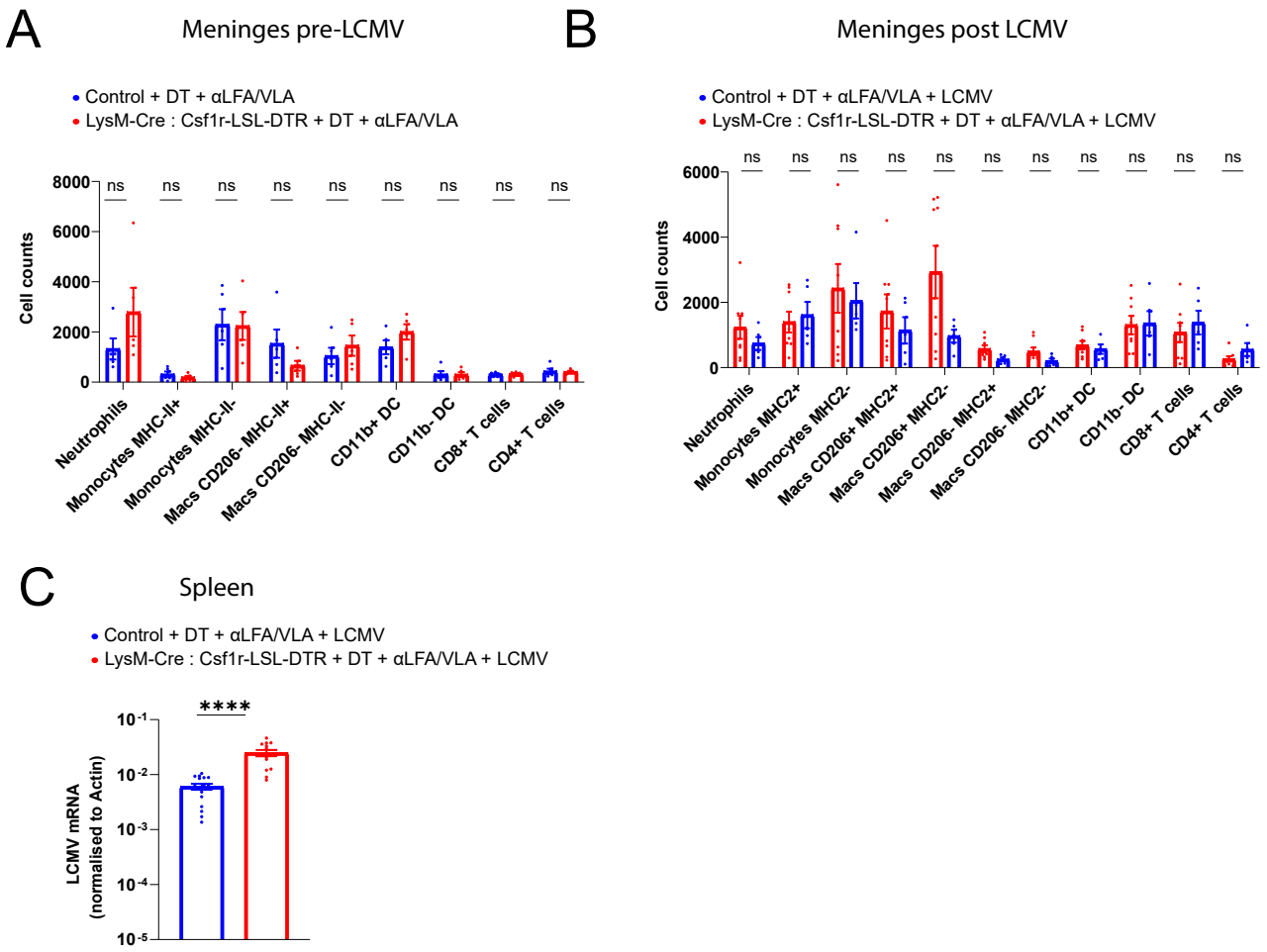

Supplementary Figure 12

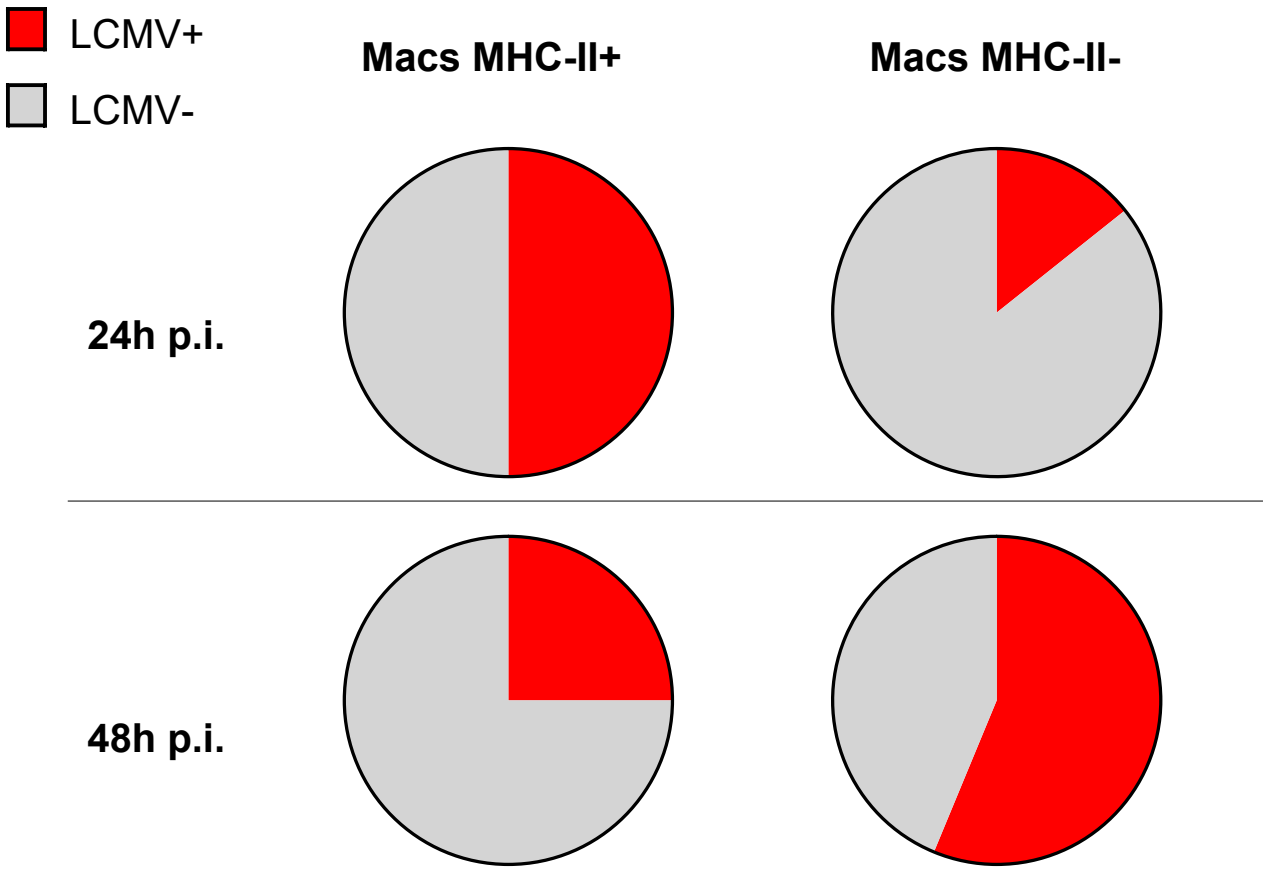

Supplementary Figure 13